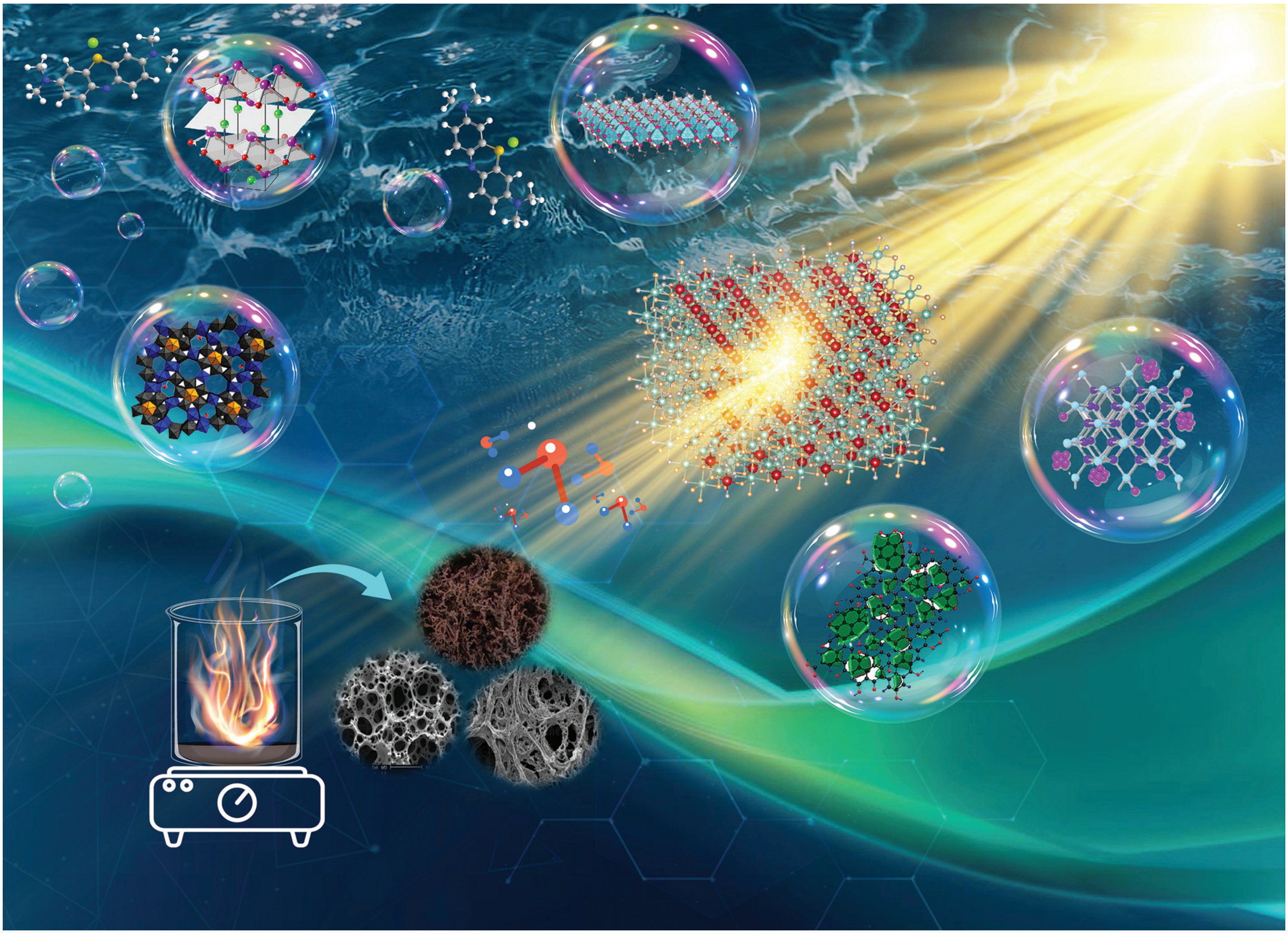

Showcasing the review work from School of Science, Minzu University of China; Inorganic Chemistry Laboratory, University of Oxford, UK; Institut National de la Recherche Scientifique, Centre Énergie, Matériaux et Télécommunications, Canada and Department of Physics and Applied Mathematics, PIEAS Pakistan.

Solution combustion synthesis: the relevant metrics for producing advanced and nanostructured photocatalysts

Nanoscale metal oxides have shown great potential towards photocatalytic applications to provide renewable and sustainable energy through solar energy conversion. This review focuses on the versatility of solution combustion synthesis (SCS) methods in producing complex and multicomponent photocatalysts. The illustration depicts SCS, a powerful technique for the synthesis of various morphologies and crystallite structures of nanomaterials for photocatalytic applications in wastewater treatment.

As featured in:

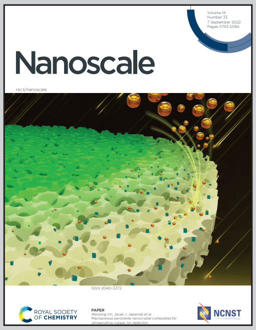

Nanoscale

See Fizza Siddique,
Sergio Gonzalez-Cortes,
Xiaoming Zhang *et al.*,
Nanoscale, 2022, **14**, 11806.

ROYAL SOCIETY
OF **CHEMISTRY**

rsc.li/nanoscale

Nanoscale

ROYAL SOCIETY OF CHEMISTRY

REVIEW

View Article Online
View Journal | View Issue

Check for updates

Cite this: *Nanoscale*, 2022, **14**, 11806

Solution combustion synthesis: the relevant metrics for producing advanced and nanostructured photocatalysts

Fizza Siddique, *[a,d] Sergio Gonzalez-Cortes, *[b] Amir Mirzaei,[c] Tiancun Xiao,[b] M. A. Rafiq[d] and Xiaoming Zhang*[a,e]

Received 16th May 2022,
Accepted 8th July 2022

DOI: 10.1039/d2nr02714c

rsc.li/nanoscale

The current developments and progress in energy and environment-related areas pay special attention to the fabrication of advanced nanomaterials *via* green and sustainable paths to accomplish chemical circularity. The design and preparation methods of photocatalysts play a prime role in determining the structural, surface characteristics and optoelectronic properties of the final products. The solution combustion synthesis (SCS) technique is a relatively novel, cost-effective, and efficient method for the bulk production of nanostructured materials. SCS-fabricated metal oxides are of great technological importance in photocatalytic, environmental and energy applications. To date, the SCS route has been employed to produce a large variety of solid materials such as metals, sulfides, carbides, nitrides and single or complex metal oxides. This review intends to provide a holistic perspective of the different steps involved in the chemistry of SCS of advanced photocatalysts, and pursues several SCS metrics that influence their photocatalytic performances to establish a feasible approach to design advanced photocatalysts. The study highlights the fundamentals of SCS and the importance of various combustion parameters in the characteristics of the fabricated photocatalysts. Consequently, this work deals with the design of a concise framework to link the fine adjustment of SCS parameters for the development of efficient metal oxide photocatalysts for energy and environmental applications.

1. Introduction

Over the last few decades, metal oxide nanostructures have been extensively investigated for their potential applications in optical, magnetic and electronic applications such as photocatalysis, environmental remediation, gas sensing, solar cells, photodetectors and photoanodes for water splitting and CO_2 conversion, *etc*. Particularly, the tunable bandgap and thus light absorption and band edge positions of metal oxides make them a potential candidate for photocatalytic applications. However, the synthesis and fabrication method can significantly alter the physical and chemical features of metal oxide semiconductors and consequently their photocatalytic performance.

To date, various techniques for the synthesis of nanostructured metal oxides have been explored, which are broadly categorized as top-down and bottom-up approaches. The top-down strategy starts with macro or micro-sized particles that are scaled down to the nano regime. However, some major disadvantages associated with such techniques are the lack of control over size, morphology and other structural properties of the fabricated particles. On the other hand, the bottom-up techniques start with the molecular level and provide significant control over the shape, size and morphology of the derived particles. Therefore, the bottom-up approaches are more popular and widely applied owing to the subtle control of the structural parameters of the derived products. The growth process of nanostructures in the bottom-up approach can also be controlled with the assistance of reagents such as growth inhibitors, ligands and surfactants. The most popular bottom-up techniques are the wet chemical procedures such as the solution combustion synthesis (SCS) technique,[1–7] solution-based-hydrothermal and solvothermal methods, and

---

[a]School of Science, Minzu University of China, Beijing, 100081, People's Republic of China. E-mail: fizza.siddique@hotmail.com, xmzhang@muc.edu.cn
[b]Inorganic Chemistry Laboratory, Department of Chemistry, University of Oxford, South Parks Road, Oxford OX1 3QR, UK.
E-mail: sergio.gonzalez-cortes@chem.ox.ac.uk, slgoncor@gmail.com
[c]Institut National de la Recherche Scientifique, Centre Énergie, Matériaux et Télécommunications, 1650 Boulevard Lionel-Boulet, Varennes, Québec J3X 1P7, Canada
[d]Department of Physics and Applied Mathematics, Pakistan Institute of Engineering and Applied Sciences, Nilore, Islamabad 45650, Pakistan. Fax: +92 (51) 924 8600; Tel: +92 (51) 1111, +92 (51) 1111 74327 Ext. 3247
[e]Optoelectronics Research Center, Minzu University of China, Beijing, 100081, People's Republic of China

polyol synthesis methods. However, the production of metal oxide nanostructures on a large scale through these techniques is currently limited due to the difficulties in controlling the properties of the bulky material and the utilization – in some cases – of non-environmentally friendly chemicals. Additionally, the high-temperature synthesis of metal oxides makes the procedure expensive at industrial scale. Therefore, employing an effective technique for the bulk-scale synthesis of metal oxides is of utmost importance.

The SCS technique is a relatively new materials manufacturing method, accompanied by a robust high-temperature and self-sustained exothermic reaction that makes this technique a highly energy-efficient process. We herein summarize the surging popularity of the SCS technique. The SCS method employs a homogeneous aqueous mixture of precursors followed by condensation to form a hydrogel containing a homogeneous metal cation network. The combustion reaction takes place between an inorganic reagent (generally nitrates) and fuel upon calcination. Commonly used fuels are ammonium nitrate, sucrose, citric acid (CA), tetra formyl triazine (TFTA), glycine, urea, triethylamine hydrochloride and sorbitol.[8,9] The technique is particularly suitable for the development of multicomponent and hybrid nanostructures with desired structural parameters. Also, the properties of the derived products can be modified and controlled according to the application by adjusting the process parameters of the SCS reaction.[10,11] Moreover, this technique provides a fast route to the synthesis of nanostructures with high surface area.[6,12] Additionally, the method can be deployed for the bulk production of nanostructured metal oxides as the products obtained *via* the SCS technique can be synthesized rapidly and in large quantities.

The combination of reactive fuel and oxidizer solution and combustion lends its name to *solution combustion synthesis*.[13] SCS is a violent exothermic reaction which generates the intense evolution of gases. Importantly, the energy supplied for the synthesis of metal oxide comes from the redox reactions after achieving the ignition temperature. The evolution of NO_x and CO_x gaseous products leads to a self-sustained and self-propagating combustion reaction between intermediate phases during combustion synthesis.[14] This intense evolution yields voluminous, loosely packed and finely divided nano powders. Combustion takes place when the reaction temperature exceeds the autoignition temperature of the redox (*i.e.*, oxidizer and fuel) solution. The process is identified by its unique parameters, including distinctly high heating rates (up to 10^6 K s^{-1})[15] and typical temperatures of ~2000 K in a very short period of time.[13,16] The temperature of the combustion "T_c" reaction is a critical parameter in SCS of materials. If "T_o" is the ambient "normal" temperature, generally taken as 298 K, "C_p" denotes the heat capacity at constant pressure, and "ΔH_r°" and "ΔH_p°" represent the enthalpy of reactants and products, respectively, then T_c can be estimated by the following relation:[17,18]

$$T_c = T_o + \left(\Delta H_r^\circ - \Delta H_p^\circ\right)/C_p \tag{1}$$

However, if the furnace is set at low temperature, T_c can also be lowered. This could result in amorphous derived product. To ensure the crystallinity of the product, the furnace temperature is normally set in the range of 673 K–873 K for SCS to ensure the crystallinity of the metal oxides.[19,20] It should be noted that SCS is not totally an adiabatic synthesis. The theoretically calculated temperature T_c is always higher than the measured temperature "T_m". This is because of the heat losses following gas evolution, or heat loss through radiation or incomplete combustion of fuels. The high tempera-

Fizza Siddique

Fizza Siddique received her PhD degree in 2022 at the Department of Physics and Applied Mathematics, PIEAS (Pakistan), under the supervision of Prof. M. A. Rafiq. She carried out part of her PhD research work in Prof. Peter Edwards's group at the Inorganic Chemistry Department, University of Oxford (UK). Currently, she is working as a postdoc fellow with Prof. Chuanbo Li's group at the School of Science, Minzu University of China. Her current research interests mainly focus on photocatalysis, water treatment, hydrogen production and related applications.

Sergio Gonzalez-Cortes

Sergio González-Cortés was born in Venezuela. He received his Licentiate in chemistry at the University of Los Andes (ULA) Venezuela, and his D.Phil. from Oxford University in 2005. After working for several years at the University of Los Andes as Assistant and then Associate Professor, he worked for several years at Velocys and Future Blends Ltd (UK). Sergio joined the University of Oxford in 2014 to develop advanced applications of dielectric heating in a variety of catalytic processes of interest in the petrochemical industry. Sergio has published nearly 90 papers and several reviews; he has also edited two books, Advanced Solid Catalysts for Renewable Energy Production *(2018) and* Solution Combustion Synthesis of Nanostructured Solid Catalysts for Sustainable Chemistry *(2020).*

tures "T_c" during the combustion synthesis may result in pore shrinkage, reducing pore volume and hence lowering the specific surface area of the derived product.

Li *et al.*[21] presented an excellent review on the SCS synthesis of metal oxide nanomaterials. The authors discussed the SCS-produced metal oxides for various energy applications including lithium-ion batteries, supercapacitors, hydrogen and methane production, fuel cells and solar cells. Another prominent review on SCS synthesis is given by Carlos *et al.*[22] The authors discussed the crucial parameters of SCS synthesis, and particular focus was given to the SCS synthesis of multicomponent-oxide thin films for their applications in thin film transistors. However, the present article aims to review the fundamentals of SCS, and SCS of metal oxides along with the strategies for preparing an improved photocatalyst. The focus is mainly on the enhanced photocatalytic activity and the versatility of the SCS method in producing complex and multicomponent photocatalysts. In addition, we focus on the relationship between SCS parameters and photocatalytic activity.

Photocatalysis has attracted significant attention in the context of developing green technologies for environmental remediation, including air and water treatment, and for cleaner energy production. The early research on photocatalysis was carried out on the wide bandgap semiconductors such as TiO_2 and ZnO. However, it was observed that the performance of a photocatalytic material significantly depends upon its structural and optical properties. The structural and optical characteristics of the photocatalytic material are responsible for the photoabsorption, charge carrier production and charge transfer.

We herein summarize the fundamentals, novelty and applications of SCS in the development of advanced photocatalysts. We will give a holistic perspective by including the current understanding of the different steps involved in SCS chemistry and the possible challenges for the SCS method in overcoming some environmental limitations. We also examine the photocatalytic applications of SCS-synthesized nanomaterials to gain insight into the relationship between the SCS parameters and photocatalytic performance, to establish a feasible approach to design advanced photocatalysts. This can be achieved by tuning (engineering) the physical properties such as structural parameters and shifting the response towards the visible range of the electromagnetic spectrum. Moreover, we detail the *in situ* modifications in the host semiconductor during the formative stage of the SCS process.

We initially give a brief overview of the fundamentals of photocatalysis followed by the principles of SCS including the different modes and approaches to ignite the energetic redox mixture, followed by the metrics that affect the combustion reaction. Then, we describe the SCS of nanostructured metal oxide semiconductors and their photocatalytic applications alongside the safety issues of the combustion process. Finally, we integrally analyze the relationship between SCS parameters and photocatalytic performance, with an overall conclusion and possible outlook for this very important catalysts and materials preparation method.

2. Photocatalysis: an overview

One of the most crucial problems generated in industrialization is the discharge of wastewater that contains several different types of contaminants such as organics and heavy metal ions into water systems. Several wastewater treatment technologies have been developed including filtration, the membrane separation technique, adsorption, and advance oxidation processes (AOPs). In recent years, photocatalysis using metal oxide-based catalysts has gained significant attention

Amir Mirzaei

Dr Amir Mirzaei received Bachelor's and Master's degrees in Chemical Engineering. In 2019, he obtained his PhD degree in Civil and Environmental Engineering from Concordia University, Canada. The focus of his Master's and PhD thesis was on the development of nanomaterials to remove emerging contaminants from water. In 2020, he was awarded a fonds de recherche du Québec – nature et technologies (FRQNT) with a rank of first. He is currently a FRQNT post-doctoral fellow at the Institut National de la Recherche Scientifique (INRS), Canada. His current research interests are focused on the development of thin-film photocatalysts for environmental applications.

Tiancun Xiao

*Tiancun's research is focused on overcoming the impacts of excessive emissions. His research group has developed novel processes and catalysts to capture and utilise CO_2, including turning it into jet fuel, fine chemicals or biodegradable plastics, e.g., poly glycolic acid, strip usable hydrogen from fossil fuels, and create clean hydrogen from plastic waste. He is the CEO of OxCCU Tech Ltd, (**https://www.oxccu.com**), a spinout company from Oxford University.*

over the period due to its capability of total decomposition of contaminants into green by-products.

Photocatalysis has the potential to utilize the energy of photogenerated electrons for environmental remediation including water purification and clean energy production. A large number of applications have spawned a renewed scientific interest in the field of photocatalysis and the advances in photocatalysis are rapidly growing, so far particularly in photoinduced reactions in metal oxide semiconductors.[23] However, the conversion efficiency of solar energy into chemical energy in photocatalysis needs maximization. Efforts have been made to understand the fundamentals of photocatalysis as well as to improve the efficiency of the photocatalytic reaction by synthesizing novel photocatalysts that can harvest visible/solar light. The basic principle of semiconductor metal oxide photocatalysis is to generate an electron–hole pair by light absorption and to utilize it in redox reactions. It is usually the surface phenomenon which requires the pollutants to be adsorbed over the surface of the photocatalyst (Fig. 1).[24] A greater number of surface sites may result in higher photocatalytic performance. The surface features of the photocatalyst include the porosity, surface area, and surface sites. When light with equal or higher photon energy than the band gap is irradiated on a photocatalyst, its valence band electron excites to the conduction band leaving a hole behind in the valence band. In the second step, this electron–hole pair travels to the active sites. The schematic representation of photocatalytic degradation of pollutant when the pollutant is physiosorbed over the photocatalyst is shown in Fig. 1.

In general, it is assumed that the photogenerated electron can be transferred to the active site if its redox potential lies below the conduction band of the photocatalyst, whereas the hole can be transferred to the donor site if its redox potential lies above the valence band of the photocatalyst. However, the ability of a semiconductor to transfer the photogenerated electron and hole to the active site also depends on the band energy position of the photocatalyst.[25] The approximate band edge positions of different metal oxides along with the redox potentials of water-splitting half reactions at pH 7 with respect to normal hydrogen electrode (NHE) are shown in Fig. 2.

These photogenerated electrons and holes, when transferred to the active sites, lead to redox reactions to generate reactive oxygen species (ROS). It is well established that the initial step in the photocatalytic reaction is the generation of short-lived and highly reactive $^{\bullet}OH$ radicals through hole trapping.[27] The $^{\bullet}OH$ radicals are generated on the hydroxylated metal oxide surface through the direct oxidation of adsorbed water molecules or surface hydroxyls, or direct oxidation of pollutant molecules present in the aqueous solution. This process is immediately followed by the reduction of adsorbed oxygen species to initiate the formation of ROS such as the superoxide anion radical $^{\bullet}O_2^-$, and singlet oxygen $^1O_2$, and the production of hydrogen peroxide H_2O_2 during the photocatalytic process (Fig. 3).

ROS are the primary intermediates and one of the most dominant participants in the photocatalytic process. These ROS attack the pollutant molecules such as organic dyes and lead to degradation products.[28] The presence of these radicals has been confirmed by spin trapping experiments with EPR spectroscopy.[29] However, the use of metal oxides for high-end photocatalytic applications is prompted by higher photoabsorption in the range of the visible spectrum. The schematic mechanism of photocatalytic water depollution by semiconductor metal oxide is shown in Fig. 4. The other important factor that has gained considerable attention in photocatalysis is the inhibition of electron–hole recombination. Once the photoexcitation takes place, there must be enough time for an electron and hole to transfer to the active site (adsorbate site), otherwise the electron will recombine with the hole. The recombination rate is therefore known to retard the photocatalytic efficiency. There is a large body of literature dealing with the modifications made on the semiconductor metal oxide surface to suppress the recombination rate.

M. A. Rafiq

Muhammad Aftab Rafiq is a Professor at the Department of Physics and Applied Mathematics PIEAS (Pakistan). He obtained his PhD degree in Physics from the Cavendish Laboratory, University of Cambridge (UK) in 2006. He has worked at Imperial College London (UK) as a visiting researcher, and as a postdoc research fellow at the Tokyo Institute of Technology, Tokyo (Japan). He is also a fellow of the Institute of Physics, Chinese Academy of Sciences (China).

Xiaoming Zhang

Prof. Xiaoming Zhang is an associate professor at Minzu University of China, and her research field lies in functional interface assembly, nanomaterials and nanodevices. She received her PhD degree in 2007 from the Chemistry Institute of the Chinese Academy of Sciences. From 2007 to 2015, she worked as a postdoctoral researcher at Keio University (Japan), Dublin City University (Ireland) and the National Center of Nanoscience and Technology (China), respectively. She has published over 30 peer-reviewed journal papers. Details can be found at: ***https://www.researcherid.com/rid/A-1301-2009***.

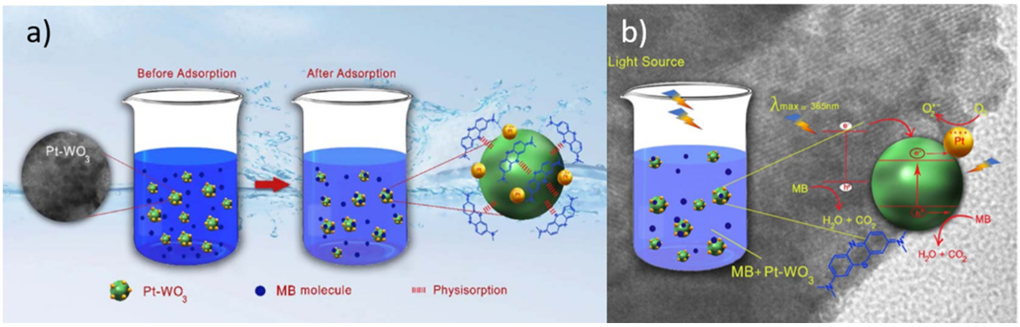

Fig. 1 Schematic representation of (a) adsorption of pollutant in water over the photocatalyst surface, (b) photocatalytic degradation of adsorbed pollutants. This figure has been adapted from ref. 24 with permission from IOP, copyright 2021.

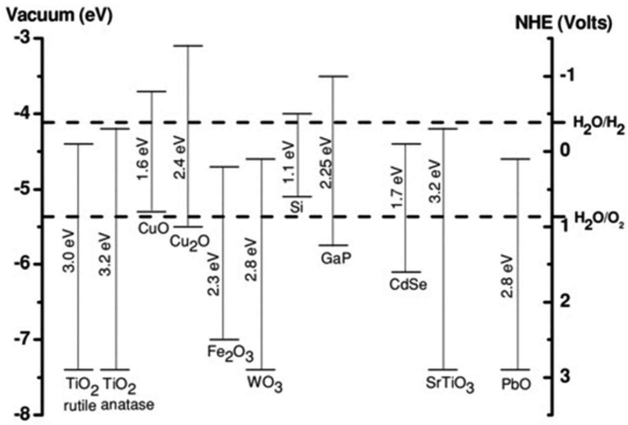

Fig. 2 Energy band diagram of different metal oxides and their redox potentials of water splitting. This figure has been adapted from ref. 26 with permission from Wiley, copyright 2012.

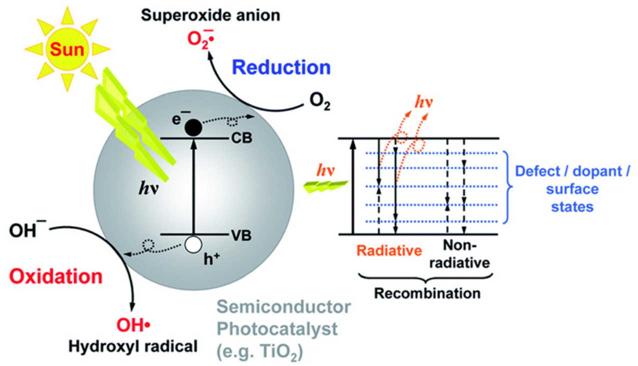

Fig. 4 Schemetic representation of the principle of photocatalysis. This figure has been adapted from ref. 30 with permission from RSC, copyright 2014.

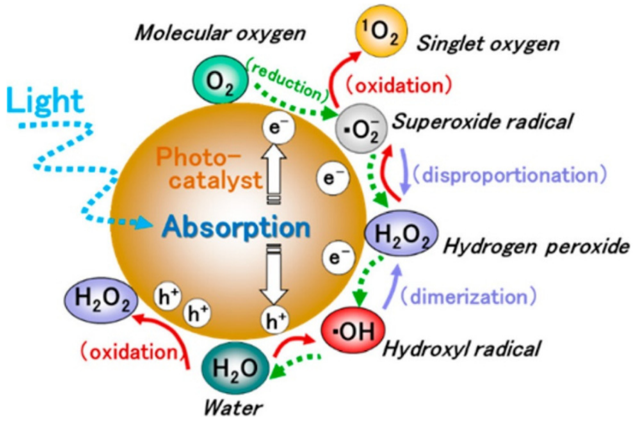

Fig. 3 Generation of ROS in photocatalytic reduction and oxidation of oxygen and water. This figure has been adapted from ref. 28 with permission from ACS, copyright 2017.

During the past decades, several classes of materials such as metal oxides, metal sulphides, carbon and polymer-based materials have been utilized in photocatalysis. Ever since the pioneering work of Frank *et al.*[31] in photocatalytic oxidation of cyanide *via* TiO_2, metal oxide semiconductors have frequently been explored for photocatalysis. The unique chemical, optoelectronic, and thermal properties as well as the stability of metal oxides make them eminently potential and promising candidates for photocatalysis.[32] Additionally, the tunability of metal oxides provides an extra degree of freedom in the development and design of novel photocatalysts. Studies show that single-component and unmodified metal oxides such as ZnO and TiO_2 usually exhibit photoabsorption in the UV region due to their large band gaps. Since solar light offers only ~4% UV light out of its spectrum, researchers are keen to develop solar/visible light-driven photocatalysts. In view of utilizing solar light, many new compounds of semiconductor metal oxides have been developed. These modifications include surface modifications such as creating defects and oxygen vacancies in pristine metal oxides, doping of transition metal atoms (cations such as Bi, Ni, *etc.*) at the metal site, doping of non-metal anions (such as N and C) at the oxygen site, and fabrication of composite and hybrid metal oxide materials. Besides the band gap, photocatalytic efficiency is also greatly influenced by size, morphology, surface area and porosity of the synthesized metal oxide.

A variety of synthesis methods have been employed to synthesize nanostructured metal oxide semiconductors. The selection of an appropriate synthesis method may lead to the successful synthesis of nanostructured metal oxide. Moreover, the physical properties of the fabricated products significantly depend upon the synthesis method. Therefore, the synthesis method has a great influence on the performance of the metal oxide in photocatalytic applications. According to the literature,[33,34] researchers actively focus on the following factors in the development of the rational design of photocatalysts:

- Availability of adsorption sites.
- Tuning of bandgap and/or extension of excitation wavelength.
- Prevention of charge carrier recombination.
- Promotion of photoinduced charge carriers to the active sites, and providing adequate quality of active sites on the surface of the photocatalyst to facilitate forward reaction.

3. Fundamentals of SCS

Two main methods can be distinguished from the self-sustained reaction synthesis (SRS) technique: (1) self-propagating high-temperature synthesis (SHS) and (2) solution combustion synthesis (SCS). These routes differ mainly based on the reactivity of the gas phase and the physical state of the reactants and products. The SHS technique was first named and developed by Russian scientists in 1967.[35] Among the several methods that have been employed for the synthesis of nanostructures, the SCS method is a unique and well-established approach for the development of nanomaterials. This method was developed in the mid-1980s by Kingsley and Patil for the synthesis of α-alumina and related binary oxide materials;[36,37] since then, SCS has been effectively applied for the development of metals and metal oxides for various applications including in potassium ion batteries,[38] electrocatalysis,[39] materials for lithium storage,[40] and in various biomedical applications such as in photodynamic therapy,[41] glucose detection,[42] supported catalysts[43,44] *etc.*

3.1 Advantages of SCS

Several advantages of SCS can be identified: (1) cost-effectiveness, (2) environmentally friendly, (3) easy to scale up to make products in large quantity, (4) facile synthesis method without requiring expensive equipment, (5) self-propagating fast reaction that decreases synthesis time and allows ultra-rapid development of novel materials, (6) high-purity products (due to high reaction temperature during combustion, which can volatize impurities), and (7) the possibility of obtaining new non-equilibrium or metastable phases and consolidating inorganic materials into a final product in one-pot synthesis.[45–47] Moreover, varying the synthesis parameters allows fine tuning of properties of the solid product.

The solution combustion synthesis is a process intensification (PI) approach to synthesize metal oxides.[46,48–51] SCS-synthesized metal oxides often show more advanced performance than their calcined counterparts.[52] In general, the SCS of metal oxides is a possible combination of solid- and gas-state reactions between the precursor powders. The reaction requires effectively high temperatures to overcome the diffusional barrier to enhance the mobility of the reacting species and to bring them significantly closer to facilitate the chemical reaction. Yet the harsh reaction conditions in this case may preclude subtle control over the morphology, size and porosity of the desired product. Moreover, they also preclude the possibility of synthesizing thermally labile products.[53] Rajeshwar *et al.*[54] concluded that the SCS of oxide semiconductors is more energy efficient in contrast with the ceramic route and some of the soft chemistry synthesis techniques.

3.2 Thermodynamic considerations

As the name depicts, SCS is accomplished in a liquid media that is usually water. The solution contains an oxidizer (usually metal nitrates) and an organic compound (or fuel) as reducing agent. The oxidizer–fuel redox mixture facilitates the combustion by providing enough exothermicity to the reaction. Another important feature of the fuel is to make stable complexes with metal ions, thereby preventing selective precipitation of metal ions during water evaporation. Once the redox mixture is ignited, the energy required for the reaction is provided by the reaction itself. Hence, the SCS process promulgates by self-sustained redox reactions between metal nitrates and fuel and obeys all the characteristics of combustible systems. The basis of the combustion synthesis process comes from the thermochemical theory formulated in the field of propellants and explosives, and its extrapolation to the combustion synthesis of metal oxides.[55] However, simple methods for the calculation of thermochemical parameters for combustion synthesis are required.

The initial state of the SCS system is essentially a non-equilibrium state due to non-minimal Gibbs free energy. Moreover, the system can be described as a quasi-stationary state, since it does not undergo significant changes over a fairly long time. Therefore, the minimization of the Gibbs free energy of the system provides the driving force for the redox reactions during combustion by converting chemical potential into heat energy. During ignition, extremely high temperatures can be obtained in very short periods, for instance 2–3 seconds, providing a very short time for heat to escape to the environment. Therefore, the system can be safely assumed to be a thermally isolated system for a short period of time. For a longer period (10–100 s) the system is, however, not thermally isolated and exchanges heat with the environment. Under the thermally isolated assumption, the maximum attained temperature is typically known as the adiabatic temperature. The enthalpy of a system is a state function. If $\Delta C_{\mathrm{p}}(\text{product})$ is the change in heat capacity for the formation of the combustion product and $\Delta H^{\circ}_{\mathrm{f},298}$ is the standard enthalpy of formation of the combustion product at 298 K, the heat released during the reaction is given as:

$$\Delta H^{\circ} = \Delta H^{\circ}_{\mathrm{f},298} + \int_{298}^{T_{\mathrm{ad}}} \Delta C_{\mathrm{p}}(\text{product})\mathrm{d}T \tag{2}$$

For an adiabatic system $\Delta H^{\circ} = 0$. This implies, $-\Delta H^{\circ}_{\mathrm{f},298} = \int_{298}^{T_{\mathrm{ad}}} \Delta C_{\mathrm{p}}(\text{product})\mathrm{d}T$.

This is for the case when the adiabatic temperature T_{ad} is less than the melting point "T_{mp}". In the case when T_{ad} is equal to T_{mp} then a factor is added called heat of fusion of the product "ΔH_m" times the fraction (*i.e.*, stoichiometric coefficient) of the product in aqueous state "ν".

$$-\Delta H^{\circ}_{f,298} = \int_{298}^{T_{ad}} \Delta C_p(\text{product})\mathrm{d}T + \nu\Delta H_m \tag{3}$$

In the case when T_{ad} is greater than T_{mp}, the expression becomes:

$$-\Delta H^{\circ}_{f,298} = \int_{298}^{T_{mp}} \Delta C_p(\text{product, solid})\mathrm{d}T + \Delta H_m + \int_{T_{mp}}^{T_{ad}} \Delta C_p(\text{product, liquid})\mathrm{d}T \tag{4}$$

Thermodynamic data for most compounds are available in the literature.[56] Hence, the adiabatic temperature of the combustion reaction can be calculated using these relations. So far, due to simplifying stipulations added in the theoretical model, the consensus between observed combustion temperature T_c and calculated adiabatic temperature T_{ad} is lacking.

The fundamental theoretical models for combustion were formulated in the 1950s. The other important combustion parameters such as propagation velocity can also be determined through both empirical relations and theoretical methods. Provided that T is the reaction temperature and T_o is the ambient room temperature in Kelvin, ϱ is the density of the precursor material, k is the thermal conductivity, C_p is heat capacity, q is the coefficient of heat loss, t is the reaction time in seconds, r is the sample radius in cm, ε coefficient of emissivity, Q is the heat of the reaction, η is the reacted fraction, and W is the rate of the reaction, the heat balance equation at any point in the sample can be given as:[57,58]

$$C_p\varrho\frac{\mathrm{d}T}{\mathrm{d}t} = k\nabla^2 T + \varrho Q W(\eta, T) - q(T - T_o) - \frac{2\varepsilon\sigma_0}{r}\left(T^4 - T_o^4\right) \tag{5}$$

$$\text{Propagation velocity} = [\text{conduction}] + [\text{chemical reaction term}] \tag{6}$$

These four terms on the right-hand side of eqn (6) describe the heat produced by conduction and chemical reactions minus the heat losses by convection and radiation. Thereby, the adiabatic combustion wave velocity $\bar{V}_a$ can be calculated. The function $W(\eta,T)$ is given by the following relations:

$$W(\eta, T) = \frac{\mathrm{d}\eta}{\mathrm{d}t} = \bar{V}_a\nabla\eta \tag{7}$$

$$= (1-\eta)^n K_0 \exp\left(-\frac{E}{RT}\right) \tag{8}$$

where E represents activation energy and R is the universal gas constant. In the same way, the thermodynamics of the system also demonstrates essential parameters for kinetics of the reaction such as processing time and the rate at which the system moves to equilibrium state for the minimization of Gibbs free energy, which in turn controls the production of compounds with desired physical and chemical characteristics.

3.3 Modes of combustion synthesis

Based on mode of ignition, the combustion synthesis technique can be classified in two modes. The first is the self-propagating high-temperature synthesis (SHS) mode, and the other is known as volumetric combustion, also called thermal explosion or bulk combustion mode. In SHS mode, the reactant compact is typically ignited at one end. Typically, the reactant is exposed to a heat source for ignition. The heat flow during this stage of synthesis (*i.e.*, SHS) is directed from the environment to the reacting mixture, thereby the sample temperature reaches ignition temperature. Once ignited, the materials react exothermically, and a rapid (~0.1–10 cm s^{-1}), high-temperature (~1000–3000 °C) combustion wave front propagates from one end of the mixture to the entire volume. The combustion wave propagates in a self-sustaining manner to convert reactants into products. In contrast, in volume combustion mode the whole volume is rapidly heated to the ignition temperature. The uniform heating allows the reaction to initiate throughout the volume, making it difficult to monitor the evolution of the reaction media. Moreover, the vigorous gas phase evolution and solid product eruption during combustion also inhibit observation of the reaction mechanism.[59] Therefore, this mode of combustion reaction is usually less controllable and is applied for the weakly exothermic combustion reactions where well-nanostructured materials can be obtained. In both the combustion modes, initially the heat flow is directed from the environment to the reaction mixture and during combustion it reverses (*i.e.* from the reaction mixture towards the environment) due to the exothermic nature of the reaction. Volatile impurities greatly expand producing highly porous metal oxides and composites with low mechanical strengths.[59,60]

3.3.1 Conventional combustion synthesis. Regardless of the operation mode, all combustion synthesis requires an external heat source to ignite the combustion (or redox) precursor mixture. Each route involves a specific method of combustion synthesis. The typically adopted method is to place the ceramic container containing the precursor solution on a hot plate or inside the preheated furnace at 300–500 °C. Heating will cause the solvent to evaporate from a precursor mixture and lead to the formation of a hydrogel. The hydrogel then decomposes and self-ignites, followed by combustion, and then produces solid product in subsequent steps as shown in Fig. 5.

The second route is the sol–gel combustion synthesis in which the precursor solution is first heated on a hot plate below the boiling point of the solvent. This allows the water to evaporate from the precursor mixture to form a hydrogel. Depending on the concentration, this can also be deposited over substrates by methods such as spin coating, spray coating or dip coating, to obtain thin films. The hydrogel formation is usually done through condensation of sol or by the incorpor-

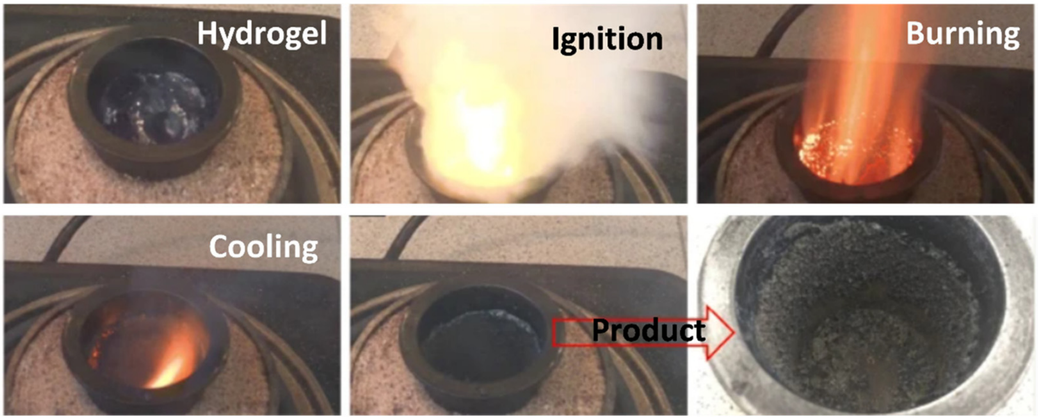

Fig. 5 Different stages of SCS of CuO/CeO_2 composites fueled by urea at fuel-to-oxidizer ratio of 0.8. This figure has been adapted from Cam *et al.*[61]

ation of polymers,[62,63] and produces the nanostructured materials after a combustion step.

3.3.2 Microwave (MW)-assisted solution combustion synthesis. Since the 1980s the use of MW equipment has been progressively escalating in research laboratories and MW equipment is widely used for heat treatment. Researchers have proposed a facile way to ignite the combustion precursor mixture through MW heating, thereby assisting SCS. However, according to the literature, conventional SCS is more widely studied and applied than MW-assisted SCS. The first MW-induced synthesis of an organic compound was reported in 1986, and opened a whole new approach for combustion synthesis.[64] Later, MW-assisted combustion synthesis of ceramics was employed by Dalton and co-workers in 1990.[65,66] Since then, MW-assisted SCS has attracted a great deal of attention in the combustion synthesis of advanced nanostructured materials.[67] The major advantage of MW heating is the considerably short reaction time that cannot be obtained by conventional heating. MWs are known to penetrate deeply into the structure and elevate the reaction temperature well above the boiling point of the solvent, and increase the rate by a factor of 10–1000.[68] Thereby, reactions are completed in minutes or even seconds. Moreover, MW irradiation heats the sample nearly uniformly and ignition starts from the center so that the combustion wave front travels radially outwards.[60] Hiranmayee *et al.*[69] observed that MWs speed up the volume combustion even with a smaller amount of fuel. Since the MWs are directly absorbed by the lossy material, a MW heat source ensures the sustainability of ignition temperature during the synthesis. Because of the aforementioned MW heating peculiarities, along with the extremely fast reaction rate due to direct interaction between the electromagnetic radiation and the reactants, the MW technique has led to undoubted advantages in terms of processing time, product yield, product purity, and material properties.[46,65,70,71] Fig. 6 shows schematically the difference between conventional heating and MW heating.[72,73]

Various studies reported in the literature show the significant influence of the MW heating source on the physical and chemical characteristics and catalytic efficiency of combustion-synthesized metal oxides.[73–76] MW-assisted SCS is seen to develop more fine and active metal oxide catalysts than the metal oxides obtained from conventional combustion synthesis.[77] Ajamein *et al.*[77] showed that the MW combustion technique can synthesize smaller CuO particles with higher surface area and improved crystallinity. The effectiveness of

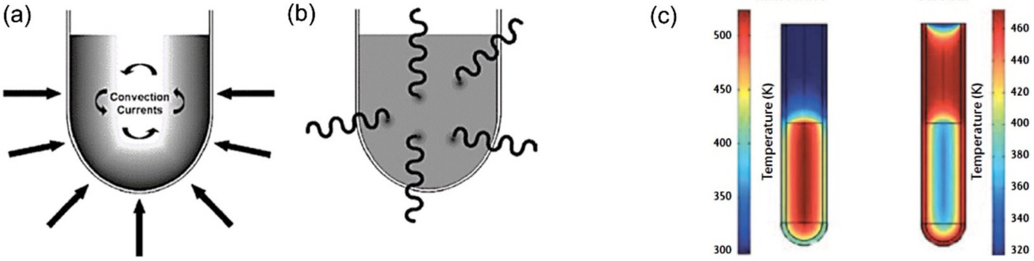

Fig. 6 (a) Conventional heating, (b) MW heating, (c) comparison of temperature gradients in conventional heating and MW heating. This figure has been adapted from ref. 72 with permission from Elsevier, copyright 2016.

MW SCS investigated by Khodaeipour *et al.*[78] also showed high porosity and greater surface area of the MW combustion-derived metal oxide ($Bi_mO_nBr_z$) photocatalyst than the one ($Bi_mO_nBr_z$) synthesized by the conventional SCS process. The high porosity of the photocatalyst allows ease of adsorption–desorption and diffusion of large pollutant molecules, thereby enhanced catalytic activity could be achieved by MW-assisted SCS-synthesized catalysts.[77–80]

3.3.3 Ultrasound-assisted combustion synthesis. Process intensification can also be done by means of ultrasonication, as it provides a smart, cost-effective and green synthesis approach. Ultrasound is composed of the 20 kHz to 5 MHz frequency range, and travels in the form of compressions and rarefactions through liquid media. The propagation of these waves produces cavitation/micro bubbles in the media that grow to a maximum size and then collapse. This process leads to local hotspots (~4000–10 000 K), significantly high local pressure ($\sim 1.013 \times 10^8$ Pa), microjets and rapid heating and cooling rates of 10^{10} K s^{-1}.[81,82] Moreover, the periodic occurrence of ultrasonic compressions and rarefactions leads to turbulence in the solution. Studies show that the generation of local hot spots and pressure *via* ultrasonication assist and enhance chemical reactions. The unique ultrasonic characteristics coupled with extreme combustion reaction conditions increase the overall reaction rates. Fig. 7 shows schematically how ultrasonication is employed in combination with the SCS process. Note that the cavitation and its eventual implosion drive the combustion of the redox precursor.

There are few studies on ultrasound-assisted SCS of metal oxides.[84,85] The experimental setup requires an ultrasonic transducer dipped in the precursor solution during furnace heating, generating ultrasonic waves until ignition. The coupling of ultrasound technology with combustion synthesis is also useful in the production of (1) well-dispersed metal oxide particles favored by the turbulence produced by ultrasonication in the precursor solution, and (2) a nano-porous structure generated due to the ultrasonic cavitation process. The unique reaction conditions provided by acoustic cavitation are also known to break agglomerates.[86,87] Zhou *et al.*[83] reported that the particle size of Li_2TiO_3 obtained by ultrasound-assisted combustion synthesis was smaller than that of particles obtained by conventional combustion synthesis and the solid-state reaction technique. Furthermore, in this study the ultrasound-assisted combustion-synthesized powders were observed to have nano-sized pores that were not seen in the conventionally combustion-synthesized powders. However, comparatively less work has been done on ultrasound-assisted combustion synthesis for photocatalytic applications. Wang *et al.*[88] showed that ultrasound-assisted combustion-synthesized Sr^{2+}-doped $BiFeO_3$ nanoparticles are a potential photocatalyst owing to their surface defects.

In overview, since the combustion reaction is self-sustained after ignition and the products are obtained through the *in situ*-generated heat, the energy requirement for the SCS process is limited to only up to the ignition stage. In addition to the conventional method for the initiation of the combustion process (or ignition of the energetic redox mixture), two other ignition modes *i.e.*, MW- and ultrasound-assisted SCS are potentially capable of enhancing the greenness of the combustion method. Although MW is a powerful energy transfer tool, several peculiarities may arise from the coupling of MW energy with SCS reactants. However, most of the theoretical reports on MW–matter interaction deal with the losses due to the electric field component only. Thus, approximations need to be made for the experiments performed in a domestic multimode MW cavity. Nevertheless, several reports show that MW-assisted SCS has potential for the development of novel nanomaterials with improved yield of the product and shorter synthesis time. The ultrasonication technology, on the other hand, may be employed with the SCS process to produce well-dispersed and mesoporous structures. Hence, it is an advanced technique that can potentially address the agglomeration of SCS-derived crystallite products, a major limitation of SCS. Ultrasonication technology coupled with the SCS technique is promising for the synthesis of binary, ternary and doped metal oxide nanoparticles.[89,90]

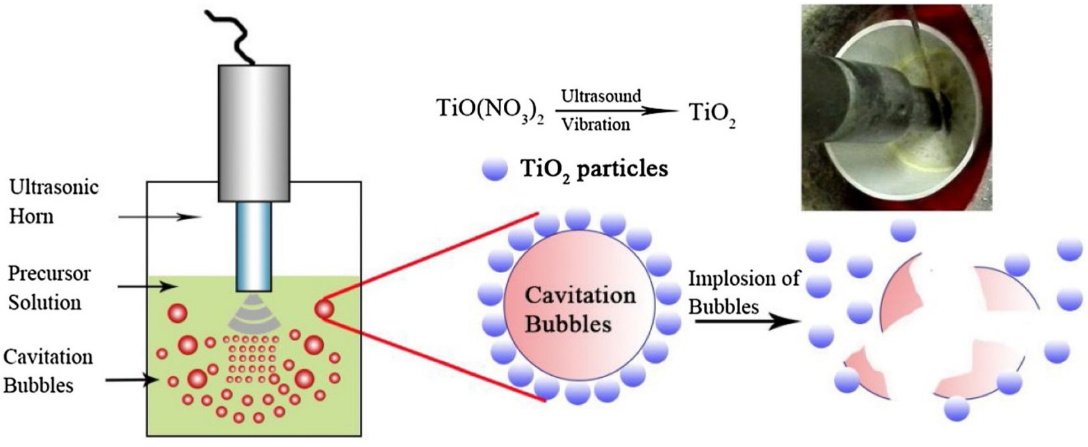

Fig. 7 Schemetic diagram of ultrasonication-assisted SCS. This figure has been adapted from ref. 83 with permission from Elsevier, copyright 2017.

4. Factors affecting SCS

The combustion reaction has a complex mechanism. The heterogeneity of the reactant solution is of the scale of 10–100 μm; coupled with an extremely high reaction temperature and rapid reaction rates during combustion, this makes it difficult to have precise control over the size and morphology of the derived product. It is therefore necessary to look into the applied parameters of the combustion reaction that have a consequential role in production. These parameters include the applied temperature, reaction time, type of fuel, amount of fuel, fuel-to-oxidizer (F/O) ratio and pH of the redox solution. The literature shows that optimization of the initial parameters is crucial in getting subtle control not only of the characteristics of the derived product but also for the application standpoint.

In general, the synthesis of nanomaterials by solution combustion can be divided into the following steps:

- Preparation of the redox solution through the dissolution of the oxidizer and reducer reactants.
- Formation of energetic gel-like network (or viscous solution) upon the aging and drying step.
- Combustion process.
- Calcination process to burn off residual carbon material.

All these steps evolve through a sequence of events (*e.g.*, complexation reaction, condensation, dehydration, precipitation, melting of free fuel, gas and solid-state chemical reactions) induced by the increase of the temperature, as illustrated in Fig. 8. When the redox solution is uniformly heated, these steps take place nearly simultaneously when the sample is under uncontrolled thermal condition at temperatures above the ignition temperature of the metal–organic redox network. These steps can also occur through a gradual progression to the ignition temperature and subsequent combustion when the redox solution is under controlled thermal condition (*i.e.*, slow heating process).

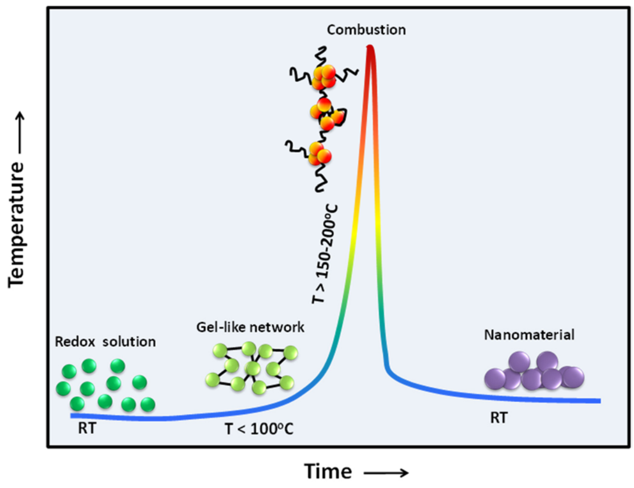

Fig. 8 Pictorial representation of the temperature and structure evolution of SCS-synthesized nanomaterials from the redox solution to the formation of a redox network and subsequent combustion reaction. The combustion material would require an additional calcination step if residual carbon material needed to be removed.

In the next sections, we will analyze in detail the most important steps involved in the SCS method and their influences over the micro- and nanostructure, morphology and the general physical and chemical properties of the nanomaterials. This includes several metrics such as metal precursor, organic fuel (or complexing agent), pH, solvent, concentration, temperature of gelation, oxidizing/reducing character of the combustion atmosphere and temperature of the final calcination step.

4.1 Aqueous chemistry of the redox solution

The dissolution of an ionic salt in a solvent depends on the balance of the ion separation process from the crystal lattice to a weak interaction state and the process of ion solvation. The overall energy of these two processes controls the dissolution of ionic salts.[91] An aqueous solution of a transition metal ionic salt, as catalyst metal precursor, takes place through the coordination of the water molecules with the metal cation (M^{z+}), where z^+ corresponds to the metal ion charge. This process occurs *via* electron transfer from the lone pair electrons in the water molecule (ligand) to empty d-orbitals of M^{z+} to produce $[M(OH_2)_h]^{z+}$, where h is the coordination number of the cation, being six for hexaquo-ion complexes. The aquo-ligand complexes of transition metals with charges of usually +2 and +3 can undergo the hydrolysis reaction as illustrated in eqn (9) and (10). The water deprotonation is due to the weakening of the O–H bond of coordinated water.

$$[M(OH_2)_h]^{z+} + H_2O \rightleftharpoons [M(OH_2)_{h-1}(OH)]^{(z-1)+} + H_3O^+ \quad (9)$$

$$[M(OH_2)_{h-1}(OH)]^{(z-1)+} + H_2O \rightleftharpoons [M(OH_2)_{h-2}(OH)_2]^{(z-2)+} + H_3O^+ \quad (10)$$

The relationship between these equilibriums with the cation charge and the solution pH is illustrated in Fig. 9,

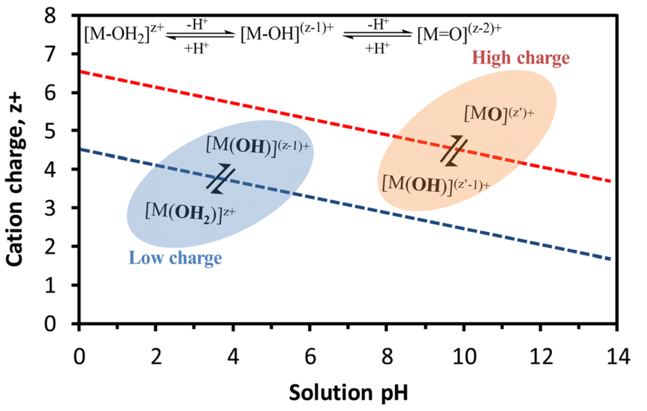

Fig. 9 Dependence of the hydrolysis equilibriums of cations on the charge and pH. Inset chemical equilibriums correspond to different degrees of hydrolysis. Figure adapted from Livage *et al.*[93] and Cushing *et al.*[94]

where the presence of aquo (OH_2), hydroxo (–OH) and oxo (═O) ligands coordinated to the metal cation is strongly dependent on these two metrics. Over a wide range of pH, cations with low charge give rise to aquo, aquo-hydroxo and/or hydroxo complexes whilst high-valence cations mainly produce oxo-hydroxo and/or oxo-complexes. For instance, the hexaquo-ion complexes of Fe^{3+} rapidly hydrolyze to give a yellow solution of aquo-hydroxo Fe^{3+} complex in acid medium, owing to the strong acidic character of Fe^{3+}. The increase of the pH causes the formation of colloidal hydroxyl-oxo-polymer that eventually precipitates as iron(III) oxide-hydroxide.[92]

The condensation reaction of hydrolyzed cations can occur through two main pathways:[95]

(1) The olation mechanism results from the release of an aqueous ligand through a nucleophilic attack of the hydroxide group onto the metal cation, leading to the formation of M–OH–M bridges as given in eqn (11).

$$\mathrm{M{-}OH} + \mathrm{M{-}H_2O} \rightarrow \mathrm{M{-}OH{-}M} + \mathrm{H_2O} \tag{11}$$

(2) The oxolation mechanism takes place through the nucleophilic addition of hydroxo groups onto metal cations to produce an oxo bridge (M–O–M) and a water molecule *via* an intramolecular hydrogen-transfer reaction (eqn (12)). Since these mechanisms operate *via* nucleophilic substitution and nucleophilic addition, ligands with high nucleophilicity and good living group are advantageous for the condensation reactions.

$$\mathrm{M{-}OH} + \mathrm{M{-}OH} \rightarrow \mathrm{M{-}O{-}M} + \mathrm{H_2O} \tag{12}$$

The synthesis of metal oxides as catalysts or catalyst precursors from an aqueous–ion complex requires either drying the aqueous solution or adjusting the pH. The drying process can produce either the precipitation of the original metal salt or amorphous metal oxides/hydroxides, which usually exhibit large crystals or aggregates. On the other hand, the adjustment of the pH may satisfactorily control the textural and morphological properties of the precipitation product. A better strategy to regulate the dimension and morphology of the nanostructured catalyst is combining an appropriate ligand (*i.e.*, chelating agent) and the adjustment of the pH to tune the stability of the aqueous metal complexes and structures to resemble the sol–gel chemistry approach.[94] This strategy is particularly suitable for the SCS method because the ligand can have different roles: (1) it can function as a chelating agent in stabilizing the metal complex and minimizing the hydrolysis equilibria, (2) as a micro- and nano-structure-controlling agent in the gelation and combustion processes, and (3) as a reducing agent for facilitating the combustion reaction.

The formation of a transition metal complex in aqueous solution involves the replacement or substitution of water molecules coordinated to the metal ion by ligands (L) as illustrated in eqn (13).

$$[\mathrm{M(OH_2)}_n]^{z+} + x\mathrm{L} \leftrightarrow [\mathrm{M(OH_2)}_{n-x}\mathrm{L}_x]^{z+} + x\mathrm{H_2O} \tag{13}$$

The ligand incorporation takes place through a sequence or stepwise equilibria that decrease the hydrolysis equilibria as the number of coordinated ligands increases. For example, the addition of ethylenediaminetetraacetic acid (EDTA) to aqueous iron solution can reduce the equilibrium constant of hydrolysis by around four orders of magnitude[96] as a consequence of the enhanced stability of the resultant metal ion complex. Indeed, the equilibrium constants of formation (or stability) of metal complexes strikingly increase when chelating agents (or polydentate ligands) substitute monodentate ligands. For instance, the addition of ammonia to an aqueous Ni solution can produce an aqueous–ammonia Ni complex (eqn (14)) whose equilibrium constant of formation is $K = 10^{2.8}$ whilst the complexation of Ni^{2+} with a bidentate ligand, *i.e.*, ethylenediamine (EN), to form an aqueous-ethylenediamine Ni complex (eqn (15)) has a stability constant of $K = 10^{7.5}$. The increased stability, known as the chelate effect, is mainly associated with the strong rise of the reaction entropy[92]

$$[\mathrm{Ni(OH_2)_6}]^{2+} + \mathrm{NH_3} \leftrightarrow [\mathrm{Ni(NH_3)(OH_2)_5}]^{2+} + \mathrm{H_2O} \tag{14}$$

$$[\mathrm{Ni(OH_2)_6}]^{2+} + \mathrm{EN} \leftrightarrow [\mathrm{Ni(EN)(OH_2)_4}]^{2+} + 2\mathrm{H_2O} \tag{15}$$

The strong interaction between the metal ion and the chelating agent can decrease the hydrolysis equilibria of metal aqueous complexes, hence facilitating the synthesis and control of the nanosize, morphology and composition of nanomaterials. CA, a weak triprotic acid, in water dissociates to produce mainly three anionic species (*i.e.*, H_2Cit^-, $HCit^{2-}$ and Cit^{3-}) through a sequence of deprotonation reactions led by the increase of the pH as given in Fig. 10a. The molecular structures of citric acid (CA) alongside other chelating agents such as ethylenediaminetetraacetic acid (EDTA), nitrilotriacetic acid (NTA), glycine and glutamic acid (GA) are depicted in Fig. 10b. These molecules clearly show their polydentate feature and usefulness as organic fuel (*i.e.*, reducing agent) for the SCS method.[97] The interaction of citrate-type species with Co aqueous solution decreases the hydrolysis of the hexaaquacobalt(II) complex because of the strong chelating effect of polydentate citrate anions, particularly at high Co : citrate ratio and pH around 5 where a water-free complex (*i.e.*, $[Co(CitH)_2]^{4-}$) is produced. The coordination reaction of Co^{2+} with citrate apparently occurs through two carboxylate groups and the hydroxyl group, whose deprotonation can take place at high pH to result in the $[Co(Cit)(OH_2)_3]^{2-}$ complex.[98]

Previous reports in the literature about the synthesis of CA-prepared CoMoP formulation for the hydrotreating process show that the chelating effect of citrate on the Co^{2+} ion prevents its sulfidation at low temperatures.[100] This facilitates the interaction of Co sulfide with MoS_2-like structure and hence the synergy between Mo and Co and the catalyst performance. Furthermore, the use of CA as chelating agent in the synthesis of CoMo formulation can also enhance the C–S bond scission through the direct desulfurization pathway and the hydrogenation route.[101] CA as a chelating agent and reducing agent (*i.e.*, fuel) can also affect the phase composition and the morphology of perovskite-type nanopowders synthesized by the SCS method. On one hand, low pH values are generally detrimental for the phase composition and the morphology whilst

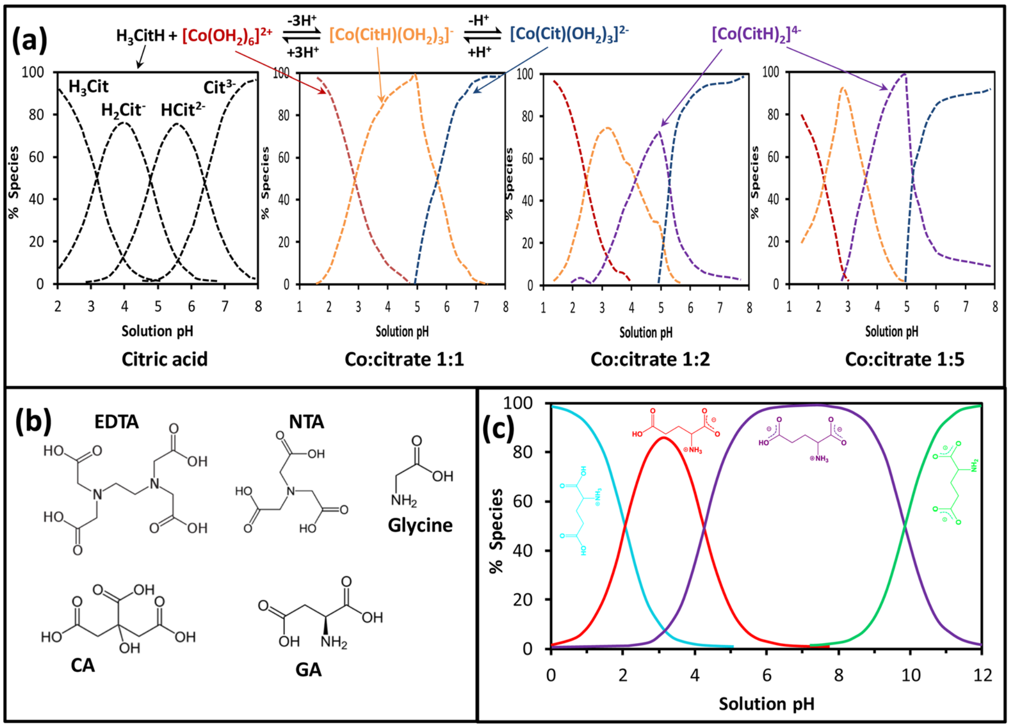

Fig. 10 (a) CA and cobalt speciation with pH and Co : citrate ratio, adapted from ref. 96, (b) molecular structures for EDTA, NTA, glycine, CA and glutamic acid (GA) as complexing agents and fuels for the SCS method, (c) speciation for glutamic acid in water, adapted from ref. 99.

high pH values cause phase segregation.[102] On the other hand, high concentrations of CA and pH above 7 are the key factors for complexing the different metal cations in aqueous solution and hence producing barium hexaferrite by the SCS approach.[103] These findings would indicate that the chelating effect of CA over diverse cations plays an important role in the SCS of mixed-metal oxides.

Glutamic acid (GA) and glycine are amino acid-type fuels that contain carboxylic and amine functional groups (see Fig. 10b) able to generate different species in equilibrium in aqueous solution. For instance, the dissolution of glutamic acid in water produces protonated glutamic acid at low pH (below 2) as shown in Fig. 10c. At pH around 3.2 above 80% of the speciation corresponds to zwitterions, whilst the maximum speciation of anion and dianion species is achieved at pH 6–8 and around 12, respectively.[99] A similar stepwise equilibrium shows glycine in water to produce three monomeric species (*i.e.*, protonated glycine cation, zwitterion and an anionic form) as displayed in Fig. 11. The stability constant for zwitterion formation is seven orders of magnitude (*i.e.*, 10^7) larger than that for the protonated glycine.[104]

$$H_2NCH_2COO^- \underset{-H^+}{\overset{+H^+}{\rightleftharpoons}} \overset{\oplus}{H_3N}CH_2COO^- \underset{-H^+}{\overset{+H^+}{\rightleftharpoons}} \overset{\oplus}{H_3N}CH_2COOH$$

Fig. 11 Stepwise equilibria showing glycine in water produces three monomeric species (protonated glycine cation, zwitterion and an anionic form).

The formation of various polymeric associates is also possible in concentrated glycine solution.[105] The bidentate character of glycine over most metal ions at high pH would facilitate the formation of mixed-metal oxides by the SCS method.[106] The glycine–metal ion interaction may enhance the formation of ferrite-type mixed metal oxide when a low content of nitric acid and high nitrate-to-glycine ratio are used in the SCS process.[104]

4.2 Formation of energetic gel-like network

Hydrolysis and condensation are crucial reactions that take place throughout the preparation of the redox solution and the subsequent mild heating step in the SCS of nanostructured catalysts and materials. Indeed, the redox solution needs to be a homogeneous system where the chemical interaction between the oxidizing precursors and the organic fuels minimizes the hydrolysis equilibria. Furthermore, the fuel, also acting as chelating agent, plays a fundamental role in the formation of viscous solutions (or glassy solids) through the condensation reaction during the ageing (gelation) period and the thermal treatment at mild conditions. The metal–organic redox network formed by interconnected metal complexes is displayed in Fig. 12a, where nitrate could act either as counter ion or ligand directly coordinated to the metal ion. The combustion fuel, usually with several and different functional groups (see Fig. 10b), produces metal–fuel complexes that can be linked to each other through a weak intermolecular interaction and even with free molecules of fuel to give rise to an

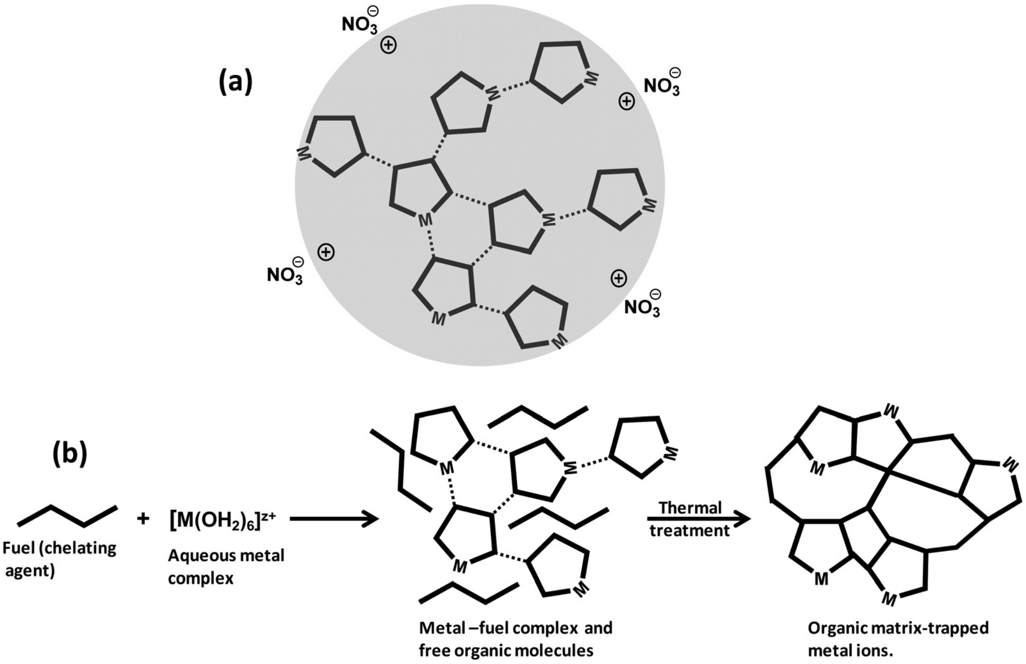

Fig. 12 Aqueous chemistry in the SCS method. (a) Representation of the metal–organic redox network and (b) the formation of a gel-like framework upon ageing and drying steps of the redox solution. Hydrogen bonding and van der Waals interactions alongside the chelate effect can facilitate the metal nitrate–organic redox framework.

amorphous glassy network with trapped metal ions upon the thermal treatment, Fig. 12b, resembling the chemistry of the Pechini method.[107,108]

The removal of water in the drying process of an aqueous solution containing inorganic metal nitrates without complexing agent produces a heterogeneous mixture of precipitates as the metal nitrate and oxyhydroxide solids. The synthesis of a redox solution with good homogeneity at atomic scale using an appropriate chelating agent, acting as organic fuel as well, can counteract the precipitation issue. The basis for the formation of the metal–fuel complex is to facilitate the gel-like formation during the water evaporation process by minimizing the hydrolysis reactions of the metal aqueous complex and hence the heterogeneous precipitation. For instance, the precipitation of iron oxyhydroxide from Fe(III) hexaaqueous complex solution can take place in a very wide range of pH and Fe^{3+} concentrations, Fig. 13a. Herein, $[Fe^{3+}]'$ is related to the concentration of free metal ion $[Fe^{3+}]$ through Ringbom's side-reaction coefficient (*i.e.*, $[Fe^{3+}]' = \alpha_{Fe(X)}\cdot[Fe^{3+}]$).[109] Highly concentrated solutions can apparently occur at very low pH regions whilst Fe ion concentrations below 10^{-7} mol dm^{-3} can exist at any pH.[110]

The presence of EDTA as chelating agent and fuel in aqueous solution containing Fe^{3+} markedly enhances the solution stability, thereby decreasing the precipitation region as illustrated in the chemical stability diagram given in Fig. 13b. Note that when two Fe ion solutions at 0.01 mol dm^{-3} and pH 6 (P_0) and at pH 8 (Q_0) are concentrated by partial evaporation of water, P_0 and Q_0 are shifted toward P_1 and Q_1, respectively. Furthermore, the pH for P_1 decreased relative to P_0 whilst Q_1 showed higher pH than Q_0, inducing the precipitation of iron (oxy)hydroxide when the excess of EDTA concentration is low. Concentrations of EDTA above 10^{-2} mol dm^{-3} hinder the precipitation reaction and facilitate the gelation process during the solvent evaporation step.[110] This sol–gel method based on the utilization of organic complexing agents was also applied to prepare ceramic superconductors.[113] In fact, ethylenediaminetetraacetic acid is a weak acid with four carboxylic acid moieties (Fig. 10b) able to dissociate to produce the metal complex, as given in Fig. 13c for fully dissociated EDTA (L^{4-}). Various anionic species such as monocarboxylate (H_3L^{-1}), dicarboxylate (H_2L^{2-}), tricarboxylate (HL^{3-}) and tetracarboxylate (L^{4-}) can be generated from the dissociation of EDTA in aqueous solution by tuning of pH (Fig. 13d).[112] This is particularly advantageous in systems with different metals where the formation of stable metal–EDTA species is required to prevent precipitation.

4.3 Effect of applied temperature and reaction time

In a typical reaction procedure, the reactant solution is preheated to remove water and then ignited to form a foam-like powder. Conventional SCS is generally carried out between 673 and 873 K furnace temperature. However, the applied temperature significantly influences the physical and chemical properties of the derived product.[114,115] Liu *et al.*[20] found that the phase, morphology and structural disordering of $LiNi_{0.5}Mn_{1.5}O_4$ spinals synthesized by SCS is greatly influenced by the preparation temperature. The crystallinity increased

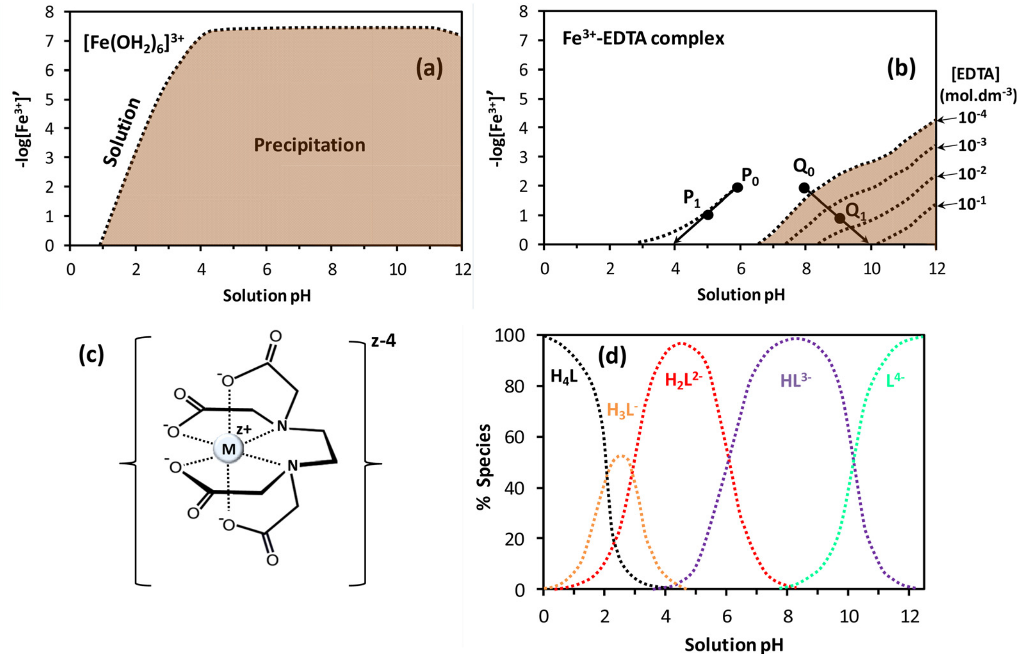

Fig. 13 (a) The pFe^{3+}–pH diagrams for Fe^{3+} aqueous solution and (b) Fe^{3+}–EDTA (ethylenediaminetetraacetic acid) complex solution; the reddish brown represents the precipitation zone whilst the dashed lines correspond to the boundary between iron hydroxide precipitation and either Fe^{3+} solution or Fe^{3+}–EDTA complex solution. The excess of EDTA concentration is between 0.1 and 10^{-4} mol dm^{-3}; figures adapted from Kakihana[110] and Kragten[111]. (c) Metal–EDTA complex with EDTA fully dissociated and (d) dependence of the EDTA (H_4L) speciation with pH, adapted from ref. 112.

with rising temperature from 400 to 600, and 800 °C. In a recent study Murthy *et al.*[116] synthesized calcium aluminate ($CaAl_2O_3$) using coffee husk as a green fuel at 600, 700, 800, 900 and 1000 °C. According to XRD (X-ray diffraction) analysis, the samples derived at 600 °C and 700 °C were completely amorphous whilst higher synthesis temperature enhanced the solid crystallinity.

In MW-assisted SCS, the temperature of the reaction is directly related to the intensity of the incident MWs, controlled by the MW power and the dielectric loss of the energetic gel-like redox mixture. Thus, MW power influences the size, morphology, surface area, porosity and performance of the synthesized products. Hashemzehi *et al.*[79] evaluated the effect of MW power on the properties and performance of Zn/Cu aluminate spinel using urea and ammonium acetate fuel. The samples synthesized under higher MW powers showed improved morphology and a more uniform distribution of crystals. Increasing the MW intensity also resulted in growth of the pore diameter of the derived product. The growth of pore diameter facilitates the esterification reaction by providing easy access for fatty acid molecules into the pores of the catalyst and hence better binding with the surface. Therefore, increasing MW power during combustion synthesis may enhance the catalytic performance.

Although SCS of solid materials takes place in a relatively short period, the reaction time (or the post-thermal treatment) is another important parameter in determining the particle size and morphology of the derived product in the SCS process. Wang *et al.*[117] reported that a graphene/ZnO composite of variable porosity can be obtained *via* fine tuning of SCS processing parameters including synthesis time and temperature of combustion. The composite porosity only appeared at 400 °C and above. The resulting pore sizes after 1 min treatment of the precursor mixture in a muffle furnace at 450, 500 and 550 °C were 3, 30, and 52 nm, respectively. Interestingly, the increase in calcination time widened the average pore size as revealed in TEM (transmission electron microscopy) images (Fig. 14A). The evaluated average pore sizes were 3, 44, and 48 nm at combustion time of 1 min, 10 min and 20 min, respectively, as shown in Fig. 14B. Under certain reaction conditions (*e.g.*, 450 °C for 1 min) the combustion of the redox mixture produced ZnO nanoparticles, whilst the oxidation of carbon generated porosity in the solid composite. Thereby, the degree of oxidation was also observed to increase with the increase in combustion time and temperature.

4.4 Effect of metal nitrate precursor

In general, metal salts can be used as metal precursors in SCS including acetates, nitrates and some other precursors.[118–123] However, metal nitrates are the most common metal precursors[114,124] because of their wide positive features including (1) relatively high oxidizing character, (2) high solubility in water (and polar organic solvents), (3) relatively low decomposition temperatures, (4) highly volatile decomposition products, and (5) low cost. Other metal precursors such as hydroxides,[125] alkoxides,[126,127] acetates,[128,129] oxalates[130,131] and

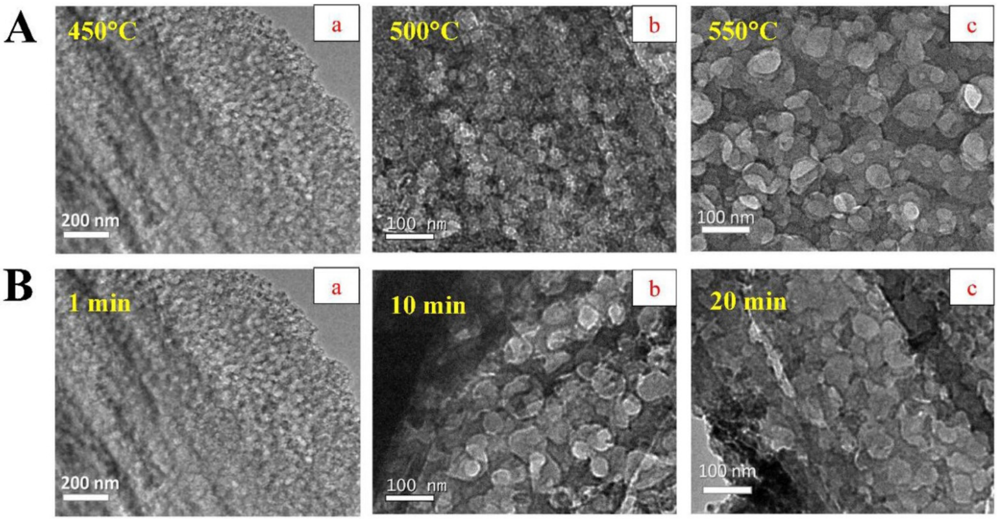

Fig. 14 TEM images showing porous graphene with different pore size (A) prepared at different temperatures, (B) variation in pore size when prepared under different synthesis time at a constant reaction temperature. This figure has been adapted from ref. 117 with permission from Elsevier, copyright 2019.

acetylacetonates[132,133] have also been used. However, they do have a reducing character instead of oxidizing property, and an additional oxidant such as nitric acid or ammonium nitrate is required to obtain a suitable redox mixture. Metal–chloride precursors have also been investigated in the synthesis of bulk and supported catalysts by combustion synthesis.[134,135] Unfortunately, this type of metal source does not present an oxidizing character and a small content of residual chloride could remain in the combusted nanomaterial.

In some cases when nitrates are not available, other metal precursors are also utilized.[56,63] Morales *et al.*[121] used peroxotungstic acid as tungsten precursor for the SCS of very fine WO_3 particles of size 22, 16 and 12 nm by varying glycine, urea and thiourea fuel, respectively. In another report by Chen *et al.*,[136] ammonium paratungstate ($(NH_4)_6H_2W_{12}O_{40}$) was employed as metal precursor with three different fuels – glycine, urea and CA – to synthesize various nanoscale tungsten oxides. The type of metal precursor employed in the SCS also has an influence on the derived product. In a study by Thomas *et al.*,[137] two different tungsten precursors, namely $(NH_4)_2WO_4$ and $Na_2WO_4{\cdot}2H_2O$, were used in the SCS of Ag_2WO_4, $CuWO_4$ and $ZnWO_4$. Structural analysis revealed that $Na_2WO_4{\cdot}2H_2O$ resulted in the formation of almost pure monophasic product, whilst $(NH_4)_2WO_4$ led to the formation of a biphasic structure.

The kinetics and some mechanistic aspects of the thermal decomposition of metal-nitrate salts have been formerly described by various researchers;[138–140] however, an in-depth understanding of this topic has been elusive because of the different – and sometimes complex – thermal chemical properties of the metal nitrates. According to Małecki and coworkers,[141,142] the thermal decomposition pathway of transition metal nitrates occurs through a consecutive (or sequential) mechanism that involves three stages, as illustrated in Fig. 15. The first route (from 25 °C to around 70 °C) involves the melting of the metal nitrate and the release of weakly bound water to produce a partially dehydrated metal nitrate.

The second stage proceeds at temperatures between 70 and *ca.* 200 °C through further dehydration and release of nitrate as nitric acid alongside the formation of metal hydroxynitrate (*i.e.*, $M(OH)_b(NO_3)_{z-b}$) and even metal oxynitrate $\left(MO_{\left(\frac{b}{2}\right)}(NO_3)_{z-b}\right)$. The presence of these intermediate nitrates depends on the cation's ability (acidity) to assist the hydrolysis reaction, particularly when M^{z+} ($z > 2$) can be further oxidized.[143] The formation of evaporated water (steam) together with HNO_3 could produce an azeotropic mixture (68% HNO_3

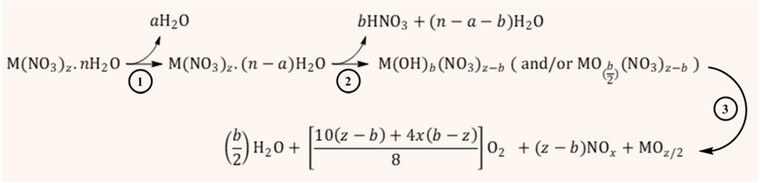

Fig. 15 The mechanistic pathway of the thermal decomposition of metal nitrates through three stages: (1) partial dehydration, (2) further dehydration–partial denitration and (3) degradation of nitrate to produce metal oxide.

and 32% H_2O) with a boiling point (120 °C) higher than that of any of its constituents.[144] The last step occurs at temperatures above 200 °C and involves the degradation of the nitrate group, from the metal hydroxynitrate/oxynitrate and even nitric acid, to produce the metal oxide followed by NO_x (NO, NO_2, N_2O, N_2O_2, *etc.*), oxygen and water emissions. Certainly, the intrinsic properties of the metal (cation) markedly affect the mechanistic pathway and hence the formation of the intermediate nitrates and the distribution of the gaseous products.[141,142]

The identity of the metal ion primarily defines the thermochemical stability (or reactivity) of the metal-nitrate precursor because of the electronic interactions between the metal and nitrate group, although other factors such as annealing atmospheres,[145,146] catalyst support,[147] vacuum heating[148] and controlled thermal treatment[149] can also affect the thermolysis of metal nitrates. Metal cations with high positive charges relative to the ionic radius (or charge density, CD) will decrease the N–O bond energy through the polarization of the electronic cloud of the nitrate ion and back donation of the π-electronic cloud in nitrate for transition metals with accessible d-orbital vacancies, as illustrated in Fig. 16a. Both effects promote the nitrate dissociation and hence the thermal decomposition of the metal-nitrate salts, as determined by Yuvaraj *et al.*[150] and Cochran *et al.*[144] for various alkali, alkaline-earth, rare-earth, transition and post-transition metal nitrates.

They found an inverse proportional dependency between the decomposition temperature of the metal nitrates and the polarizing power of the metal cation or charge density ($CD = 3z/4\pi r^3$), where z and r correspond to atomic charge and atomic radius (nm), respectively. A better rationalization of the relative stability of metal nitrates can arise from considerations of electronegativities, cation radii and polarization effects. Interestingly, the charge density–decomposition temperature correlation can be extended to the ignition temperatures of SCS-type redox mixtures as given in Fig. 16b, where the decomposition temperatures of various metal-nitrate salts follow approximately the trend of the ignition temperatures of glycine–metal nitrate mixtures.[151] This trend indicates that the polarizing power of the counter cation plays a major role in the thermal stability (or instability) not only of single metal nitrates but also – and most importantly – of SCS redox mixtures. Thus, the decomposition temperature of the metal nitrates appears to be a good prior metric to describe the combustibility of redox mixtures.

We have selected a broad range of metal nitrates that are relevant for the SCS of nanomaterials and, using HSC Chemistry 5.11 software, calculated the standard enthalpy of combustion $\left(\Delta H^\circ_{\mathrm{Comb}}\right)$ of the redox mixtures containing urea (reducing agent) and metal nitrate (oxidizing agent) at equivalence composition ($\Phi_e = 1$). It is worth remarking that whatever the involved fuel, a similar trend can be obtained. The decomposition temperatures (T_{dec}) of the metal nitrates were collected from a previous report[150] whilst the ionic radius of the metal cations, for the CD calculation, were gathered and compared from several sources[144,150] to ensure that every figure corresponds to the proper coordination number of the cation in the crystal structure of the considered metal nitrates. The variation of Gibbs free energy for all the considered redox mixtures specifies that the combustion reactions occur spontaneously ($\Delta G^\circ < 0$). A roughly linear correlation between $\Delta H^\circ_{\mathrm{Comb}}$ and T_{dec} clearly indicates that the combustion reaction becomes more exothermic with decreasing decomposition temperature of the metal nitrate (Fig. 17a). Furthermore, the exothermicity of the combustion reaction rises markedly with increasing cation charge (M^{z+}), from (−100 to −350 kJ M-mol^{-1}) for $z = 1$, to (−450 to −800 kJ M-mol^{-1}) for $z = 2$ and between −1000 and −1150 kJ M-mol^{-1} for $z = 3$, because of the

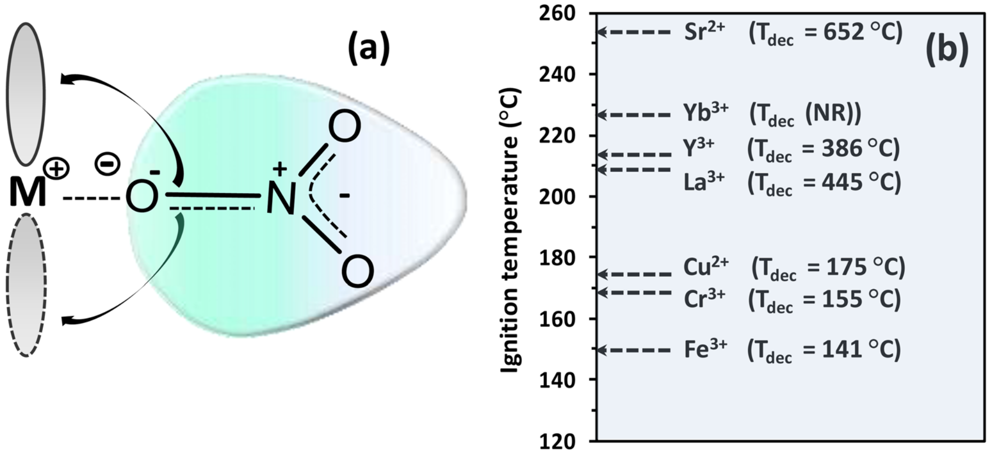

Fig. 16 Metal–nitrate interactions. (a) Illustration of high-CD metal cation attracting the electron cloud of the nitrate ion and back donation of the π-electronic cloud in nitrate to accessible d-orbital vacancies in transition metals. (b) Correlation of the ignition temperature of glycine–metal nitrate redox mixture at equivalence composition with decomposition temperature (T_{dec}) of various metal nitrates, whose values were mainly obtained from Cochran *et al.*[144] and Yuvaraj *et al.*,[150] for strontium nitrate, whilst no report of decomposition temperature of ytterbium (Yb) nitrate hydrate was found.

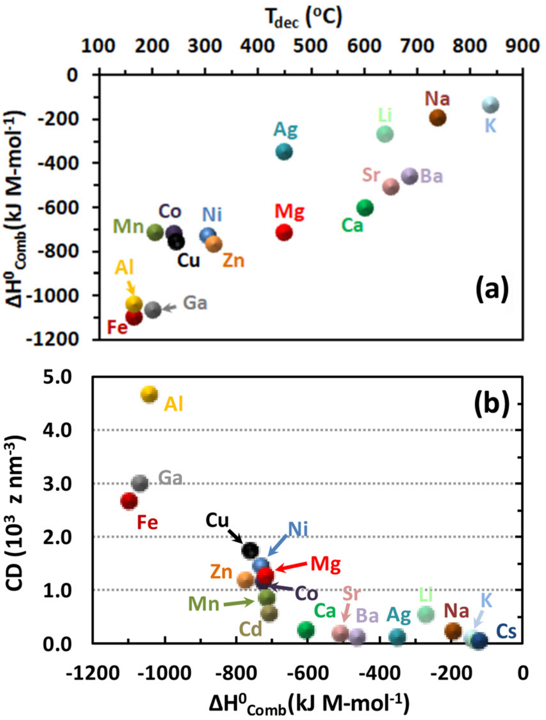

Fig. 17 SCS of metal oxides from urea–metal nitrate redox mixtures at equivalence composition (Φ_e = 1). (a) Variation of the combustion heat with the decomposition temperature (T_{dec}) of the metal nitrates, (b) correlation between the metal cation-CD and the combustion enthalpy of various redox mixtures.

rise of the oxidizing character (*i.e.*, −5, −10 and −15, respectively) of the metal nitrates.

We obtained a direct correlation between the cation-CD and the standard enthalpy of combustion (Fig. 17b); obviously this trend is opposite to the correlation between the cation-CD and the thermal decomposition temperature of various metal nitrates[144,150] because of the inverse relationship between ΔH°_{Comb} and T_{dec}. Noticeably, low-CD cations (Ag, alkali and alkaline-earth metals except Mg) exhibit little polarizing power on the counter-nitrate electron cloud, and this is reflected in relatively low combustion heats. The low polarizing ability of these cations facilitates the formation of ionic metal nitrates as a consequence of their poor trend to share their valence electron cloud with the nitrate ion. On the other hand, high-CD cations such as Al^{3+}, Ga^{3+} and Fe^{3+} effectively share their valence electron cloud with the nitrate ion to form covalent metal nitrates with weak N–O bonds, which favour the exothermicity of the combustion reaction. Intermediate-CD cations (transition metals and Mg^{2+}) also present intermediate values of combustion heats. It is worth remarking that the adiabatic temperature of the solution combustion synthesis of alkali, alkaline-earth and transition metals oxides follows a lineal dependence with the inverse radius of metal ions[152] due to the different polarizing power of the metal cations.

The cation CD metric (or T_{dec}) can be a useful descriptor of the exothermicity (or maximum temperature) that redox mixtures can reach during the SCS of mesostructured catalysts and materials. In this context, the synthesis of α-Al_2O_3 from aluminum nitrate-urea redox gel occurs at about 1500 °C (flame temperature)[36] in agreement with the high-CD Al^{3+} or low decomposition temperature of aluminum nitrate (∼160 °C). This high exothermicity is particularly advantageous for synthesizing Al-based mixed metal oxides[55] and also a large variety of alumina-based materials[153] when the other metal-nitrate precursors such as alkali and alkaline-earth metals have low CD and hence high T_{dec}. The direct SCS of maghemite (γ-Fe_2O_3) using glycine as fuel led to a violent combustion reaction, whose maximum temperature was ∼1500 °C,[13] reflecting the large exothermic character of this redox mixture. This iron oxide phase was also synthesized by direct thermal decomposition of an Fe(III) nitrate–urea complex.[154] The higher-CD Fe^{3+} compared with those for Co^{2+} and Mn^{2+} from their metal-nitrate precursors facilitated the SCS of the $LaFeO_3$-type perovskite at various Φ whilst the synthesis of $LaCoO_3$ and $LaMnO_3$ required a subsequent calcination step on the combusted samples.[155] Another example corresponds to Cu^{2+} compared with Ni^{2+}, whose glycine-based Cu/Ni redox mixture produced a combustion temperature (∼525 °C) slightly higher than that for Ni nitrate–glycine redox gel (∼475 °C)[156,157] because of higher-CD Cu^{2+} compared with Ni^{2+}. It is worth highlighting that metal ion-containing redox mixtures with intermediate values of charge density show, in general, combustion temperatures lower than those produced by redox mixtures containing Al^{3+} and Fe^{3+} metal nitrates.

4.5 Role and type of fuel

A large variety of polar organic molecules (compounds) such as hydrazides, carboxylic acids, amines/amides (carbamide/urea) compounds, amino acids, saccharides and combinations of different functional groups in a single molecule have been used as fuel (or reducing agent) for the SCS of nanostructured materials.[22,158,159] Structures of some commonly used fuels are shown in Fig. 18. The organic fuel for the SCS is usually soluble in polar solvents and particularly in water; the fuel can also act as complexing agent and metal ion dispersing agent depending on the strength of the *cation–fuel–water–nitrate* interactions in aqueous solution.[160] Certainly, the fuel also plays the role of reducing agent in the redox gel and induces a self-propagating combustion reaction that produces a nanostructured solid material and large amount of gases.[97] It is worth remarking that the substitution of water molecules coordinated to metal cations by molecules of fuel *via* stepwise fashion will lead to the formation of a metal–fuel complex, whose weakly connected units usually form resins or glassy solids.[96] On the other hand, if the *fuel–fuel* and *fuel–water* interactions through hydrogen bonds, covalent and coordinate bonds also take place, the metal precursor (and/or metal–fuel complex) will be homogeneously dispersed into a viscous organic network.[110] Regardless of the chemical interaction that predominates in the redox system, the microstructure of the combusted material will be strongly affected by the chemical properties of the fuel and obviously the chemistry that

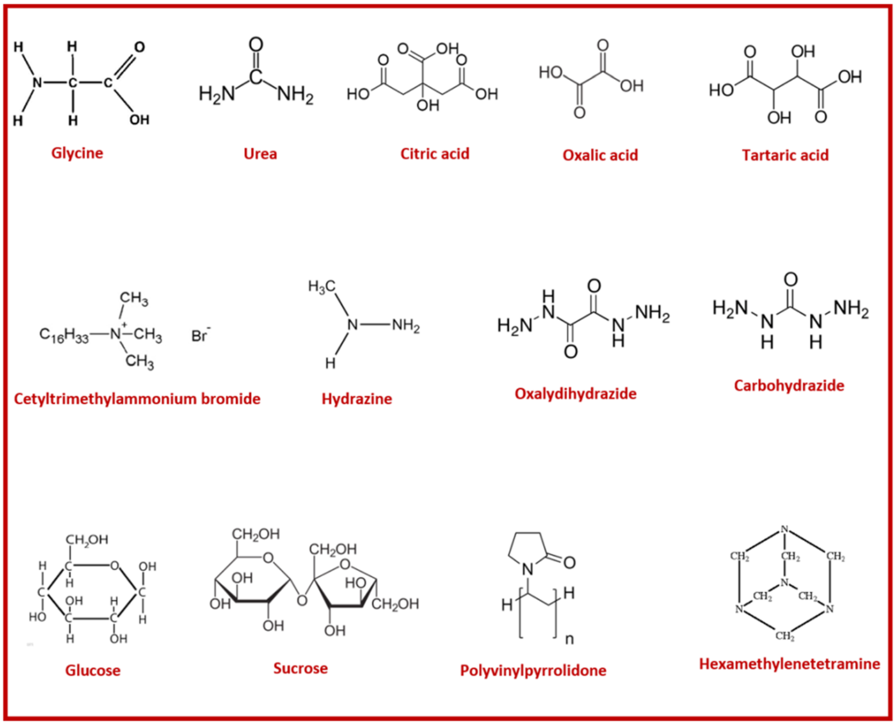

Fig. 18 Chemical structures of some commonly used organic fuels.

occurs in the solid and gas phases during the combustion process.

The precursor mixture or redox mixture in the solution combustion synthesis process is composed of one oxidizing component (*i.e.*, metal nitrate) and a reducing component "fuel". The precursor is therefore termed as the "redox" mixture. Various investigations focused on gaining understanding in combustion synthesis have been carried out. In general, a good fuel in SCS must have the following characteristics:[161]

- Fuel should behave as a complexing agent for metal ions to increase the homogeneity of the mixture.
- Fuel (and metal nitrate) is considered as a source of essential components of combustion that lead to the release of a large amount of hypergolic gases. Hypergolic gases when acquiring a critical density easily, can ignite at their ignition temperature even under ambient pressure.
- A good fuel should not produce toxic gases; however, large emissions of CO_2 and NO_x are produced.

The type of fuel has significant effects on the combustion synthesis as well as the structure, phase and morphology of the derived product. Basically, the organic fuels vary in reducing powers and quantity of gases they produce during thermal reaction. Hammami *et al.* showed that, applying similar operating conditions, in SCS La–Mn perovskite exhibits only one sharp maximum with glycine, whereas with CA fuel, two temperature maxima were observed in temperature–time profiles. This happened due to the difference in the thermal behaviours of the two systems. Additionally, the two maxima in the temperature profile with CA fuel also indicate the occurrence of secondary reactions.[162]

Toniolo *et al.*[17] reported a remarkable potential of glycine-nitrate and urea-nitrate towards the production of Co and cobalt oxide powders. They found the production of metallic Co powder by only glycine fuel in fuel-rich reactions, whereas the cobaltous oxide phase can be formed by both glycine and urea fuels in fuel-rich reactions. They attributed the difference to the chemical nature of the fuels.

Intensity of combustion, an important feature in combustion synthesis, also depends upon the reducing power of the fuel and the amount of evolved gases.[163] Therefore, varying fuel type and its amount makes it possible to modulate the major parameters of combustion synthesis. These parameters in turn determine the characteristics of the synthesized products. The combustion can vary from moderate burning to violent and intense burning depending upon the type of fuel. In recent research, Gotoh *et al.*[19] presented a study in which they synthesized persistent phosphors $Gd_3Al_2Ga_3O_{12}$:Ce^{3+}–Cr^{3+} (GAGG:Ce^{3+}–Cr^{3+}) *via* SCS incorporating mixed fuels urea and glycine. According to the study, using a single fuel can lead to an incomplete combustion reaction and amorphous products. The study also reported the rates of the combustion reaction during SCS. The incorporation of mixed fuel resulted in the highest reaction rate, *i.e.* 47.1 K s^{-1}. However, the samples with only urea and only glycine resulted in reaction rates of 3.53 K s^{-1} and 27.7 K s^{-1}, respectively. The authors also deduced that products could be amorphous if the reaction rates are lower than 30–40 K s^{-1}. Another study[164] compared

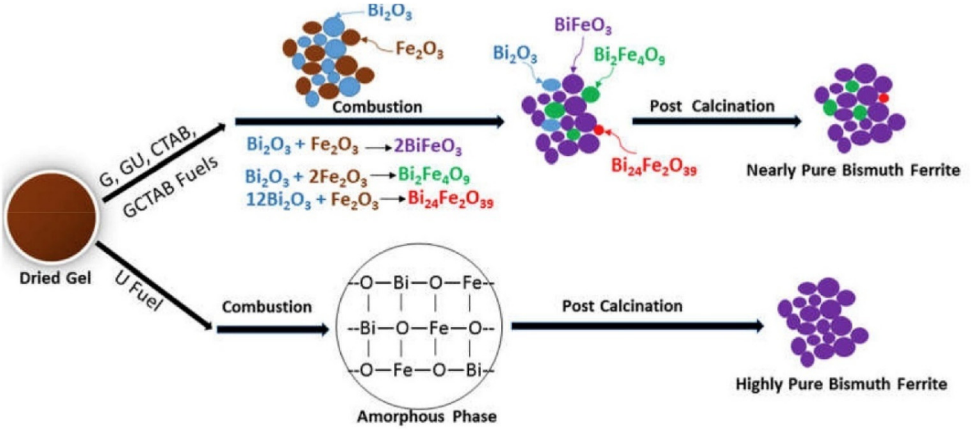

Fig. 19 Schematic diagram of phase evolution of bismuth ferrite during SCS. This figure has been adapted from ref. 164 with permission from Elsevier, copyright 2019.

the thermal analysis of dried gels prepared by urea (U), glycine (G), CTAB, and mixed fuels glycine–urea (G + U) and glycine–CTAB (G + CTAB). The schematic representation of phase evolution during the SCS process is shown in Fig. 19.

The synthesis was carried out using $Bi(NO_3)_3{\cdot}5H_2O$ and $Fe(NO_3)_3{\cdot}9H_2O$ metal precursors for the synthesis of $BiFeO_3$ keeping the fuel to oxidant ratio constant $\Phi = 1$. Except for the CTAB fuel sample, all samples showed a sharp exothermic peak at 180 °C. The combustion reaction starts and leads to the decomposition of $Bi(NO_3)_3{\cdot}5H_2O$ and $Fe(NO_3)_3{\cdot}9H_2O$ into metal oxides and gaseous products such as NO_x, HNO_3, CO_x and H_2O. The sample with glycine showed a sharp weight reduction due to the lower decomposition temperature of glycine. Therefore, a simultaneous decomposition of both metal nitrates and glycine resulted in sharp weight loss at lower temperature. In contrast, CTAB has a relatively higher decomposition temperature, which shifted the exothermic reaction to a higher temperature and relatively smaller weight loss, *i.e.* 40%. The slower decomposition rate in the case of the sample with urea as a fuel is attributed to the gradual decomposition of urea leading to the release of hyperbolic gases and delaying the reaction. Lazarova *et al.*[165] demonstrated that employing nitrogen-containing fuel (*e.g.* glycine and urea) may lead to the formation of products with larger crystallite size and a greater tendency to form aggregates, whilst utilizing carbohydrate fuel (such as sucrose and glycerol *etc.*) in SCS may lead to products with smaller crystallite size and low aggregation.

4.6 Amount of fuel and the Φ coefficient for the SCS method

Besides the type of fuel, quantity of fuel is also one fundamental factor in SCS, influencing the physical and chemical parameters of the derived product.[159,166] Fuel amount is usually given as the fuel-to-oxidizer ratio Φ. A specific method based on the oxidizing and reducing valences of the precursor mixture is employed for thermodynamic calculations.

The reducer-to-oxidizer molar ratio for a redox mixture is an important factor not only to control the exothermicity of the combustion reaction but also to prevent the precipitation of the metal oxide, hence controlling the properties of the nanostructured material. The SCS method usually employs an aqueous solution of a single or mixture of metal nitrates as oxidizing agents (or oxidizers) and a suitable organic fuel (or mixture of fuels) used as reducing agent (or reducer). The ignition of the redox mixture initiates a self-propagating exothermic reaction that sustains high temperatures for a sufficient period to decompose usually all the organic material and metal nitrate. The ignition temperature is significantly lower than the consequential combustion temperature that results in the formation of a mixture of gases and the final solid nanomaterial with specific chemical and physical properties.

Jain *et al.*[167] developed a simple method of calculating the elemental stoichiometric coefficient (Φ_e) of single or multi-component fuel–oxidizer mixtures. This concept was then adapted to the calculation of the proportion of oxidizer and fuel (reducer) for the SCS method[55,168,169] by considering metals, carbon and hydrogen as reducing elements with the corresponding metal valence, +4 for carbon and +1 for hydrogen. Oxygen as oxidizer has the valence −2 and nitrogen is considered with valence 0.

A summarized calculation to exemplify the determination of the valence–mole ratio (Φ) for the SCS of metal oxide (*i.e.*, M_2O_3) is illustrated in Fig. 20a. It is assumed for simplicity that H_2O, CO_2 and N_2 are the gaseous products formed in the combustion reaction. The metal(III) nitrate $[M(NO_3)_3{\cdot}xH_2O]$ has an oxidizing valence (OV) of −15 ($OV = 3 + 2 \times 0 - 3 \times 6 + x \times 1(2) - x \times 2$) whilst the reducing valence (RV) for glycine ($C_2H_5NO_2$) is 9 ($RV = 4 \times 2 + 1 \times 5 + 0 \times 1 - 2 \times 2$). Note that water of hydration in the metal nitrates does not contribute to the oxidizing valence. A similar calculation can be carried out for synthesizing single oxides (*i.e.*, M_2O, MO) and mixed-metal oxides such as perovskites (ABO_3), spinels (AB_2O_4), garnets ($A_3B_5O_{12}$), *etc.* Also note that a general formula for Φ calculation involves the RV, the absolute value of OV and the amounts (in moles) of the reagents (Fig. 20a). This mathemat-

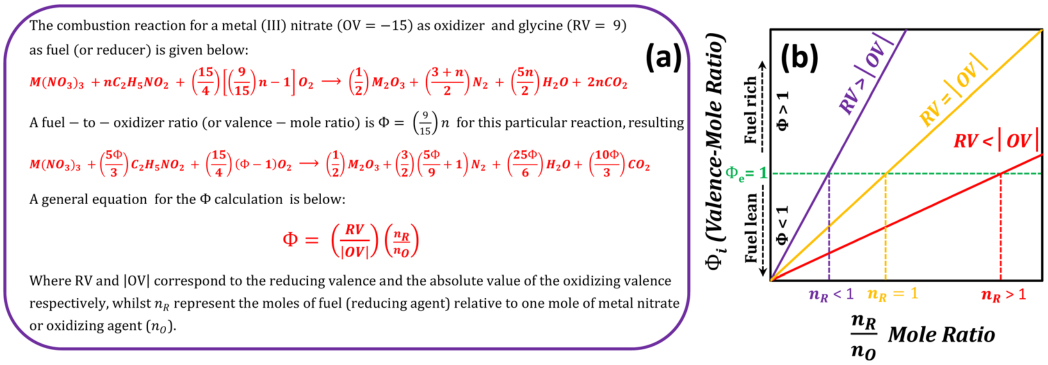

The combustion reaction for a metal (III) nitrate (OV = −15) as oxidizer and glycine (RV = 9) as fuel (or reducer) is given below:

$$M(NO_3)_3 + nC_2H_5NO_2 + \left(\frac{15}{4}\right)\left[\left(\frac{9}{15}\right)n - 1\right]O_2 \longrightarrow \left(\frac{1}{2}\right)M_2O_3 + \left(\frac{3+n}{2}\right)N_2 + \left(\frac{5n}{2}\right)H_2O + 2nCO_2$$

A fuel − to − oxidizer ratio (or valence − mole ratio) is $\Phi = \left(\frac{9}{15}\right)n$ for this particular reaction, resulting

$$M(NO_3)_3 + \left(\frac{5\Phi}{3}\right)C_2H_5NO_2 + \left(\frac{15}{4}\right)(\Phi - 1)O_2 \longrightarrow \left(\frac{1}{2}\right)M_2O_3 + \left(\frac{3}{2}\right)\left(\frac{5\Phi}{9} + 1\right)N_2 + \left(\frac{25\Phi}{6}\right)H_2O + \left(\frac{10\Phi}{3}\right)CO_2$$

A general equation for the Φ calculation is below:

$$\Phi = \left(\frac{RV}{|OV|}\right)\left(\frac{n_R}{n_O}\right)$$

Where RV and |OV| correspond to the reducing valence and the absolute value of the oxidizing valence respectively, whilst n_R represent the moles of fuel (reducing agent) relative to one mole of metal nitrate or oxidizing agent (n_O).

Fig. 20 The fuel-to-oxidizer (or valence-mole) ratio (Φ) for the SCS method. (a) Representative calculation for an oxidizing valence of −10 and reducing valence of 9 and general formula for Φ coefficient. (b) Dependence of Φ on the valence and the molar composition of the redox mixture.

ical expression is also applicable for synthesizing mixed-metal oxides, in which different metal nitrates (or oxidizing agents) are employed, with a single fuel or even a mixture of fuels as reducing agents. In these cases, the overall OV (or RV) and n_R involve the sum of stoichiometric contribution for each reactant whilst n_O still represents unity.

The lineal dependence of Φ on the n_R-to-n_O ratio is strongly affected by the reducing and oxidizing valences of the reactants involved in the combustion reaction through the $\frac{RV}{|OV|}$ ratio, as depicted in Fig. 20b. For instance, redox mixtures at optimal stoichiometric composition or equivalence ratio (*i.e.*, $\Phi_e = 1.0$), or at any other determined Φ value, will have different $\frac{n_R}{n_O}$ mole ratios because of the different reducer and/or oxidizer character of the reagents. Specifically, the number of moles of fuel (reducer) will be larger than the number of moles of oxidizer when the reducing valence is below the absolute value of the oxidizing valence in order to balance the reducing and oxidizing species, hence obtaining the equivalence ratio. An opposite trend of the valence distribution (*i.e.*, RV above |OV|) will lead to n_R-to-n_O ratio below one, whilst this molar ratio corresponds to unity when RV and |OV| have the same value. In the context of the combustion reaction, the equivalence composition of the redox mixture is obtained when no molecular oxygen is required (*i.e.*, $\Phi_e = 1$) as a consequence of well-balanced valence and moles of oxidizing and reducing species. When $\Phi < 1$ the redox mixture is under a fuel (reducer)-lean regime and molecular oxygen is available because of the excess of oxidizer relative to reducer. On the other hand, if $\Phi > 1$ the redox mixture is under a fuel-rich condition and molecular oxygen is required to fully convert the fuel to gaseous products due to the limited oxidizer compared with reducer molar amount.

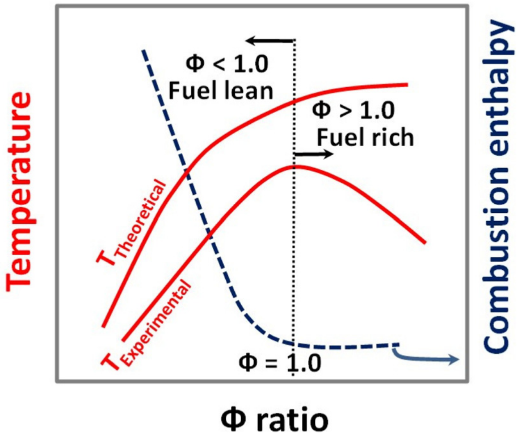

Fig. 21 Combustion enthalpy and experimental and theoretical trends of temperature as a function of Φ. This figure has been adapted from ref. 170.

As previously stated, the value of Φ determines the "richness" and "leanness" of fuel in the combustible mixture; Φ equal to 1 implies that the initial reaction mixture does not require atmospheric oxygen, $\Phi > 1$ corresponds to a fuel-rich system, and the value of $\Phi < 1$ means a fuel-lean system.[59] The exothermicity and temperature (experimental and theoretical) of the combustion reaction depend on Φ, as illustrated in Fig. 21. An increased volume of evolved gases is observed with the increase in fuel-to-oxidizer ratio Φ.[171,172] Moreover, for a given value of Φ, the system behaves differently due to the substantial difference in oxygen balance. The theory of chemical propellants depicts the evolution of maximum energy at equivalence composition ($\Phi = 1$).[173,174] Tripathi *et al.*[175] demonstrated the significant impact of amount of fuel on temperature and mode of synthesis. They used glycine as a fuel and varied the fuel-to-oxidant ratio in SCS of Li_2ZrO_3. The study showed that the fuel-to-oxidant ratio (Φ) played a crucial role in the morphology, mode of combustion and phase composition of Li_2ZrO_3 powders in SCS. In this study thermodynamic calculations showed that the amount of evolved gas and the calculated adiabatic temperature increased with the increase in Φ. However, a large amount of heat is carried away by flowing gas from the reaction mixture during combustion synthesis, therefore the actual measured temperature of the reaction decreased with the increase in Φ. Also, the mode of combustion switched to SHS-eruption from VCS for $\Phi > 1$. The effect of fuel to oxidizer on enthalpy of reaction, temperature and release of gases is shown in Fig. 22a–c. The average crystal-

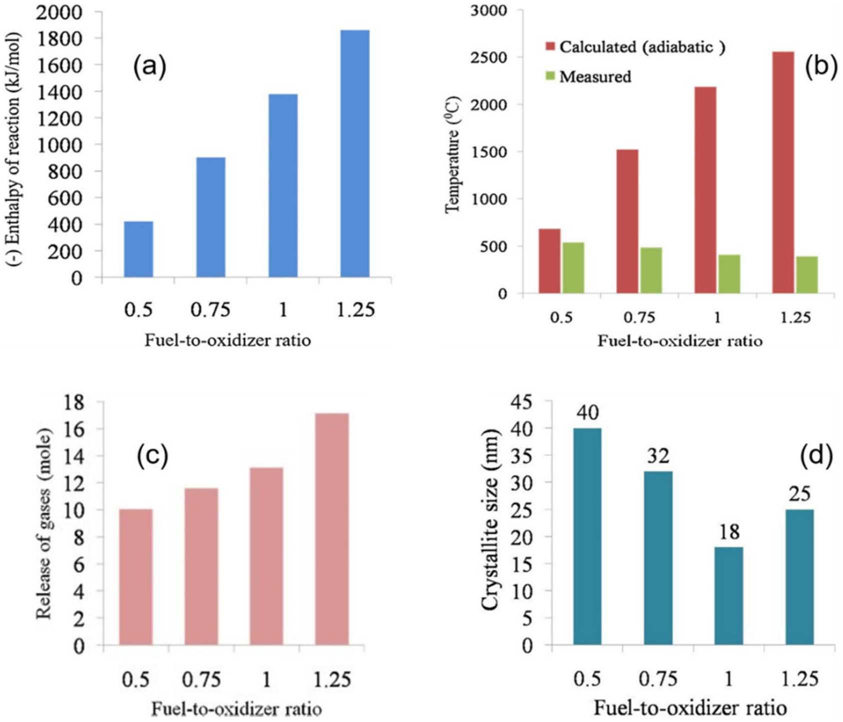

Fig. 22 Bar graphs showing the effect of fuel-to-oxidizer ratio on (a) enthalpy of reaction, (b) calculated and measured temperature, (c) release of gases, (d) crystallite size. This figure has been adapted from ref. 175 with permission from Elsevier, copyright 2020.

lite size of Li_2ZrO_3 is reported to decrease with increase in Φ. However, for $\Phi > 1$ the crystallite size is increased, which could be the consequence of the change in mode from VCS to SHS (Fig. 22d). In a similar way, the fuel-to-oxidizer ratio has a direct effect on the crystallite size of the derived product (Fig. 23).[176]

4.6.1 Phase and morphological aspects. The type and amount of fuel is well known to influence the crystallite and particle size and morphology of the derived product.[177] Gu *et al.*[178] discussed the morphological aspects of SCS-synthesized MoO_2 nanopowders by varying fuel-to-oxidizer ratio. The authors utilized $(NH_4)_6Mo_7O_{24}·4H_2O$ as Mo source and NH_4NO_3 as oxidizer with different glycine/NH_4NO_3 ratios (0.25, 0.5, 0.75, 1, 1.25). Larger and irregular-shaped particles were seen at a ratio of 0.25. Increasing the value of the glycine/NH_4NO_3 ratio to 0.5 yielded a foam-like morphology with nanoparticle size of 20–30 nm diameter. A further ratio increase to 0.75 resulted in the formation of more fine particles embedded in sheets, whilst the formation and aggregation of amorphous phase was observed at fuel-to-oxidizer ratio of 1. The highest value of this ratio (*i.e.*, 1.25) also produced only amorphous phase. Fig. 24 illustrates the effect of Φ on the morphology of SCS-derived MoO_2.

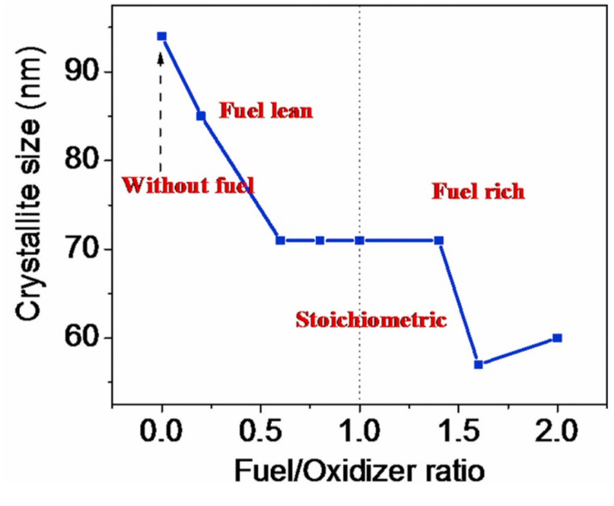

Fig. 23 Effect of urea to $Mg(NO_3)_2$ ratio on the crystallite size of SCS synthesized MgO. This figure has been adapted from ref. 176 with permission from Elsevier, copyright 2020.

In a recent study, Yilmaz *et al.*[163] compared the effect of fuel on the morphology of V_2O_5 powder synthesized by the SCS method. Three different fuels *i.e.*, CA, glycine, and starch, and a mixture of these fuels were employed in the study to synthesize V_2O_5. The SEM (scanning electron microscopy) images confirmed that the lowest particle size was obtained when glycine was used in the synthesis reaction, however, no difference in chemical structure was observed. Yu *et al.*[179] synthesized very fine manganese dioxide nanostructures *via* a novel SCS method. The fuel-to-oxidizer ratio (*i.e.* $C_2H_5NO_2$/$(Mn(NO_3)_2)$) affected the morphology of the SCS-derived manganese oxide. XRD analysis showed poor crystallinity of hexagonal ε-MnO_2 when the fuel-to-oxidizer ratio was 1 : 2. Higher crystal-

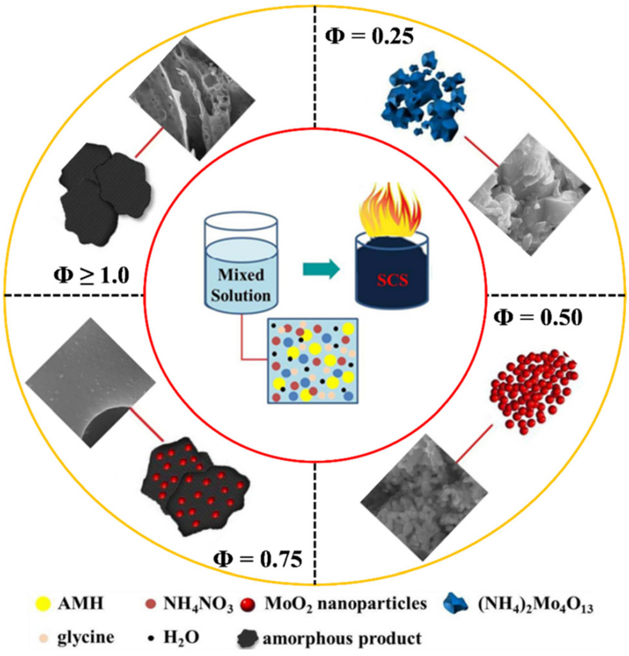

Fig. 24 Schematic illustration of SCS of MoO_2 fueled by glycine and morphological effects at different glycine/NH_4NO_3 ratios. This figure has been adapted from Gu *et al.*[178]

linity was observed when the ratio was increased to 2 : 1. Also, the morphology of SCS-derived ε-MnO_2 was influenced by the fuel-to-oxidizer ratio. The fuel-lean ε-MnO_2 solid showed nanosized particles *i.e.*, 20–25 nm, and thick plate-like morphology, whereas ε-MnO_2 with fuel-to-oxidizer ratio 2 : 1 showed spherical nanoparticles with a greater surface area than the plate-like ε-MnO_2. Similarly, Chen *et al.*[136] discussed the morphological aspects of WO_x nanostructures prepared by SCS by varying both fuel type (*i.e.* glycine and urea), mixed fuel (*i.e.*, urea and CA) and fuel-to-oxidizer ratio. The samples fueled by glycine were prepared by setting fuel-to-oxidizer ratios of 0, 5, 10, and 20, named as G1, G2, G3, and G4, respectively. The samples fueled by urea were prepared by setting fuel-to-oxidizer ratios of 5, 10, 15 and 20, named as U1, U2, U3 and U4, respectively. The samples fueled by urea and CA were prepared by fixing the CA ratio to 20 and varying the urea ratio as 5, 10, 15, and 20, named as UC1, UC2, UC3 and UC4, respectively. The morphology of all the SCS samples is shown in SEM micrographs (Fig. 25). The SEM of sample G1 prepared without glycine showed an urchin-like structure (Fig. 25ia). In preparing sample G2, small amounts of gases were produced, and the mixture did not swell up, producing agglomerated particles of size 100–200 nm (Fig. 25ib). In the G3 sample, enormous gas release was observed, and the mixture swelled up producing nanoneedles of diameter ~80 nm (Fig. 25ic). Adding more glycine to make G4 resulted in vigorous eruption combustion

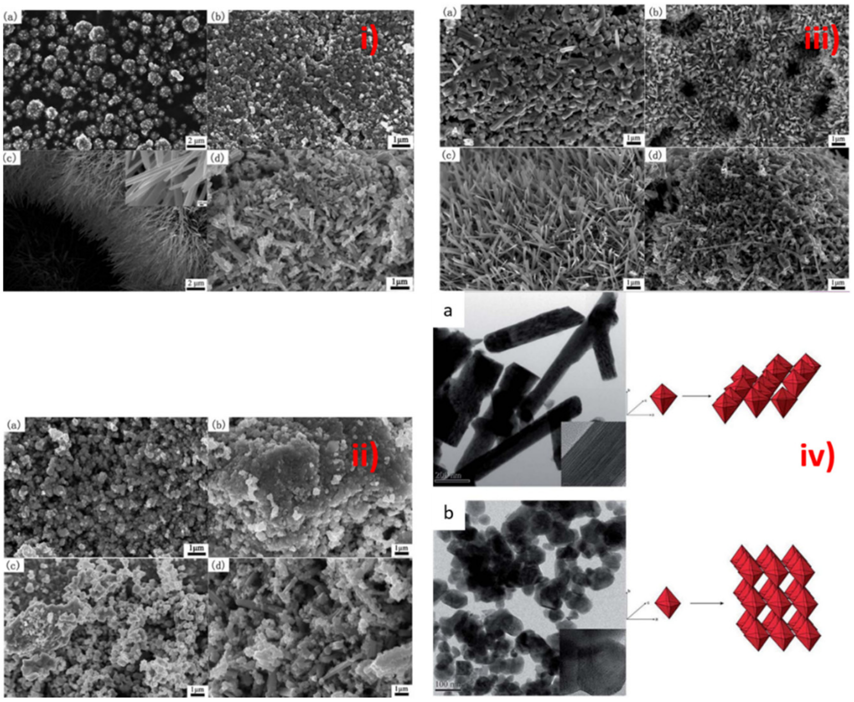

Fig. 25 SEM images of SCS-synthesized tungsten oxide (i) prepared by glycine fuel (a) G1 (*Φ* = 0), (b) G2 (*Φ* = 5), (c), G3 (*Φ* = 10), (d) G4 (*Φ* = 20), (ii) prepared by urea fuel (a) U1 (*Φ* = 5), (b) U2 (*Φ* = 10), (c) U3 (*Φ* = 15), (d) U4 (*Φ* = 20), (iii) prepared by urea and CA mixed fuel (a) UC1 (*Φ* = 5), (b) UC2 (*Φ* = 10), (c) UC3 (*Φ* = 15), (d) UC4 (*Φ* = 20), (iv) TEM image of (a) G3, (b) U3. This figure has been adapted from ref. 136 with permission from RSC, copyright 2016.

synthesis mode, producing comparatively shorter and thicker nanorods of diameter ~80 nm and length of ~5 μm (Fig. 25id). The SEM of urea-synthesized samples is shown in Fig. 25(iia–d). Samples at low fuel-to-oxidizer values (*i.e.* U1, U2 and U3) did not swell to make a foam. However, U4 led to the formation of a slightly foamy product. Noticeably, all the urea-synthesized samples were larger and agglomerated particles. The samples yielded from the mixture of urea and CA displayed regular variation in morphology with fuel-to-oxidizer ratios. The UC1 sample consisted of rod-like particles of ~1 μm along with some nanoparticles sized ~100 nm (Fig. 25iiia). The sample UC2 consisted of nanorods of ~5 μm length and 100 nm diameter (Fig. 25iiib). A further increase of fuel in the UC3 sample attenuated rod-like structures to form nanobelts (Fig. 25iiic), whilst UC4 comprised nanorods (Fig. 25iiid). Fig. 25iva and ivb display the TEM images of G3 and U3 samples, respectively. Importantly, the authors demonstrated that the G3 sample was crystallized into $W_{18}O_{49}$ whilst U3 crystallized into WO_3.

5. Influence of SCS on optical properties and oxygen vacancy generation

The SCS technique is widely used to prepare porous metal oxides.[180–183] The large volume of gases (such as H_2, CO_2, CO, NO_x and H_2O) evolving during the SCS process lead to the production of highly porous and hence high surface area products. Vasei *et al.*[184] reported the SCS of ZnO nanoparticles using cetyltrimethylammonium bromide (CTAB) as a fuel. The effect of the fuel-to-oxidizer ratio Φ influence the surface area and porosity of ZnO powders. The thermogravimetric analysis (TGA), taken at $\Phi = 1$, clearly shows the strength of solution combustion synthesis. The peak at 183 °C is the exothermic peak of SCS that leads to 45% of weight loss. Weight loss here can be divided into three regimes (Fig. 26a). Up to 150 °C, there is only 5% weight loss, *i.e.*, due to vaporization of absorbed water and dehydration of gel. The rapid weight loss at 183 °C is attributed to the vigorous combustion reaction between metal nitrate and fuel that leads to the formation of gaseous products and ZnO powder. The 10% weight loss between 250 °C and 400 °C is due to the continuous and slow oxidation of organic residues. In this research, Φ was varied from 0.5 to 1.5. The specific surface area of the powders is reported to increase from 21 m^2 g^{-1} to 35 m^2 g^{-1} with increasing Φ, as revealed by performing N_2 adsorption–desorption isotherms (Fig. 26b), whilst the pore size distribution was between 2 and 4 nm (Fig. 26c). The crystallite size calculated from XRD data showed a clear decrease from 30 nm to 20 nm with increase in fuel content. Moreover, by increasing the fuel content in SCS the particle size of ZnO powders is decreased while the band gap of ZnO increased (Fig. 26d). The decrease in particle size of ZnO powders is attributed to the rapid cooling of the combustion products, which hinders the particle growth.

The property of fuel has a diverse effect on the SCS of metal oxides. Zhang *et al.*[185] reported interesting findings in

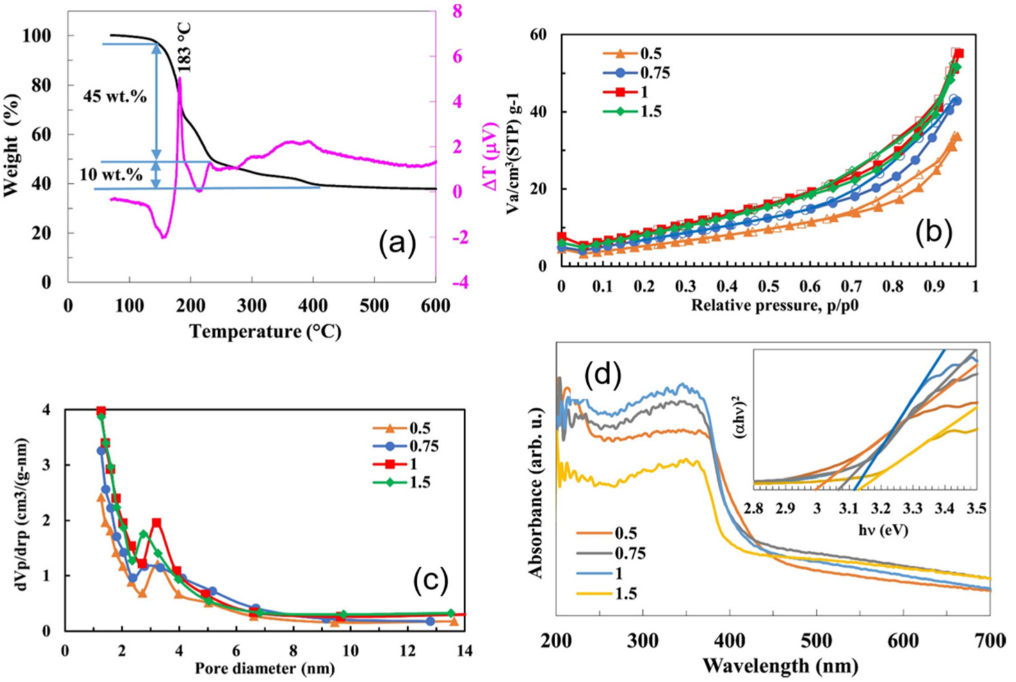

Fig. 26 Effect of fuel-to-oxidizer ratio on SCS of ZnO nanoparticles (a) TGA/DTA curves, (b) adsorption (filled symbols)–desorption (open symbols) isotherms, (c) pore size distribution, (d) bandgap from UV-Vis diffuse reflectance spectra of prepared solids. This figure has been adapted from ref. 184 with permission from Elsevier, copyright 2018.

SCS of BiOBr and Bi/BiOBr. Applying the same experimental conditions in both reactions, BiOBr was obtained using urea as a fuel, whereas Bi/BiOBr was produced using CA fuel. Thereby, two different photocatalysts were obtained, BiOBr and Bi/BiOBr, only by changing the fuel in the SCS method. In the Bi/BiOBr sample, Bi particles were attached on the surface of the BiOBr sheet. Besides the structural and morphological differences of both photocatalysts, the Bi/BiOBr composite also exhibited a greater number of oxygen vacancies. Fig. 27a contains the XPS (X-ray photoelectron spectroscopy) scans of both the BiOBr and Bi/BiOBr samples derived from urea and CA, respectively. The major constituents of the sample are Bi, O and Br with the corresponding binding energy peaks at 159 eV (Bi 4f), 530 eV (O 1s), and 68 eV (Br 3d).

The comparison of the core-level scan of BiOBr and Bi/BiOBr-3 is shown in (Fig. 27b). The two intensive peaks at 164.89 eV and 159.62 eV are due to increased concentration of oxygen vacancies in the vicinity and oxygen deficiency. Moreover, the peak at 532.49 eV for O 1s can be assigned to the presence of oxygen vacancies (Fig. 27c). Additionally, XPS findings show that the ratio of O to Br in Bi/BiOBr-3 is less than 1, indicating enhanced oxygen vacancy generation in the sample. The corresponding electron paramagnetic resonance (EPR) plot is also included in Fig. 27d, to emphasise oxygen vacancy generation only by varying fuel type in combustion synthesis. EPR provides further evidence of oxygen vacancies in the Bi/BiOBr sample. The sharp peak at g = 2.001 that occurred in the case of the Bi/BiOBr sample represents the oxygen vacancies. In contrast, this peak does not appear in the BiOBr sample that was prepared by urea.

Table 1 includes some studies on SCS of some binary and ternary metal oxides for anticorrosion and photocatalytic applications. The table clearly shows that the structural properties and hence the catalytic activity of the derived product can be controlled by choice of appropriate fuel and calcination temperature. In the case of CeO_2 and $BiFeO_3$, urea was the suitable fuel choice for enhanced anticorrosion and photocatalytic activity, respectively. In a similar way the structural control of the mixed phase of BiOBr *via* conventional and MW combustion techniques fueled by glycerol showed enhanced photocatalytic activity, whilst in obtaining $CaMoO_4$, the calcination temperature was observed to have significant control over structural properties. Increasing calcination temperature resulted in increasing crystallite size and a decrease in the surface area.

Briefly, this section demonstrates the various factors of relevance for the SCS method, including type of metal precursor, type of fuel, fuel-to-oxidizer ratio, pH and overall chemistry of the redox solution, formation of energetic gel-like networks, and combustion temperature. The section clearly shows that these parameters are critical in defining the structural properties of the derived products. Both the combustion enthalpy and combustion temperature achieve

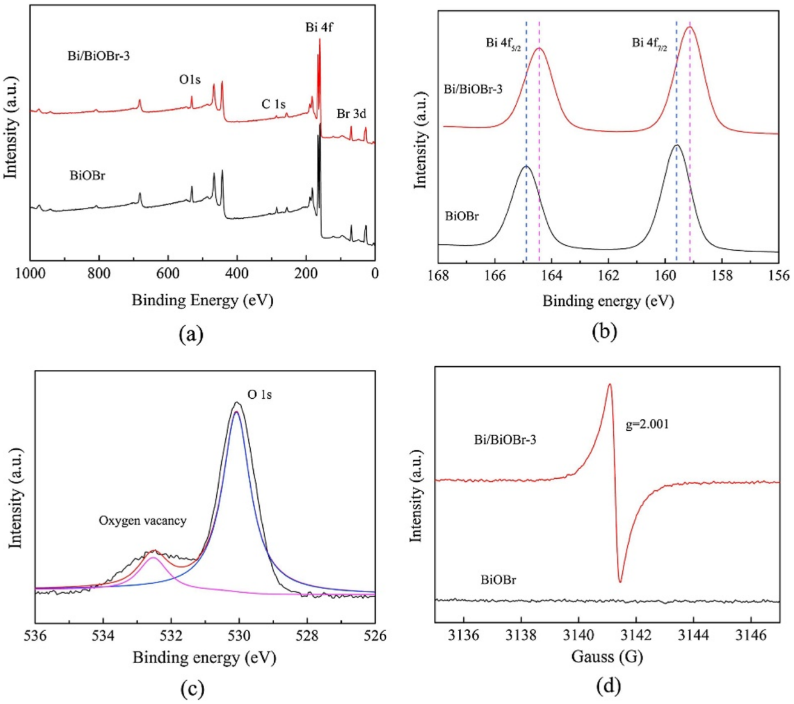

Fig. 27 XPS spectra of BiOBr and Bi/BiOBr-3, high resolution spectra of (b) Bi 4f, and (c) O 1s, (d) EPR spectra of pure BiOBr and Bi/BiOBr-3. This figure has been adapted from ref. 185 with permission from Elsevier, copyright 2019.

Table 1 Effect of fuel on some SCS-produced metal oxides

Material (application)	Synthesis conditions	Remarks	Ref.
CeO_2 (anti-corrosion)	Metal source: $Ce(NO_3)_3·6H_2O$; metal source to fuel molar ratio: (1 : 5/2, urea), (1 : 5/3, glycine), (1 : 5/8, glucose), (1 : 5/6, CA); reaction temperature: 150 °C followed by 300 °C	• All fuels except urea led to cubic fluorite structure • CeO_2 synthesized from urea showed the best corrosion protection • The lowest and highest band gap as 2.68 eV and 3.0 eV were obtained by using urea and CA, respectively • The lowest and highest BET (Brunauer Emmett and Teller) surface area as 8.5 and 47.7 $m^2\ g^{-1}$ were achieved by urea and glucose, respectively	186
Single-phase $BiFeO_3$ (photocatalytic water treatment)	Metal source: $Bi(NO_3)_3·5H_2O$ and $Fe(NO_3)_3·9H_2O$; fuels: urea, glycine, CTAB, glycine + urea, and glycine + CTAB; fuel to oxidant molar ratio (φ) = 1; reaction temperature: 80 °C followed by 250 °C	• 100% $BiFeO_3$ phase was achieved by using urea as fuel • ∼100 methylene blue (MB) removal was obtained by using $BiFeO_3$ prepared by urea under visible-light irradiation • Using urea as fuel yielded the highest purity and crystallinity • The band gap of photocatalysts was changed in the range of 1.88–2.17 eV as a function of fuel type	164
Mixed-phase $Bi_mO_nBr_z$ (photocatalytic water treatment)	Metal source: $Bi(NO_3)_2·5H_2O$ and NH_4Br; fuels: ethylene glycol (EG), propylene glycol (PG) and glycerol (G); reaction temperature: 300 °C as conventional combustion synthesis and also MW heating	• 98.9% tetracycline photocatalytic removal was achieved by using photocatalysts prepared by glycerol and MW heating • The lowest and highest BET as 44.0 and 121.2 $m^2\ g^{-1}$ were achieved by using PG and G(MW), respectively • The ratio between BiOBr and $Bi_{24}O_{31}Br_{10}$ were and band gap changed by changing the fuel and heating method	78
$CaMoO_4$ nanoparticles	Metal source: calcium nitrate tetrahydrate and dissolved molybdenum powder in H_2O_2; fuels : CA; oxidizer : fuel = 1 : 5; reaction temperature: 400 °C followed by calcination at 400 °C, 500 °C and 600 °C for 2 h at ambient atmosphere	• The sample calcined at 400 °C showed the best photocatalytic activity for MB degradation • Specific surface area was significantly reduced at high calcination temperature, while crystallinity and particle size of nanoparticles increased	187
$CuBi_2O_4$; $CuBi_2O_4/CuO$; $CuBi_2O_4/Bi_2O_3$	$Cu(NO_3)_2·2.5H_2O$, $Bi(NO_3)_3·5H_2O$	The molar ratio of Cu/Bi determined the excess of one binary component or the other in the composite. The XRD showed that the product powders formed by 5 : 1 produced ($CuO/CuBi_2O_4$), 10 : 1 ratio produced ($CuO/CuBi_2O_4$), 15 : 1 ratio produced ($CuO/CuBi_2O_4$), 1 : 5 ratio produced (α-$Bi_2O_3/CuBi_2O_4$), 1 : 10 ratio produced (α-$Bi_2O_3/CuBi_2O_4$), 1 : 15 ratio produced (α-$Bi_2O_3/CuBi_2O_4$), 1 : 2 produced $CuBi_2O_4$, 1 : 0 produced CuO, 0 : 1 produced α-Bi_2O_3	188
	The synthesis was carried out employing urea fuel at Φ value of 1 and varying Cu/Bi mole ratios as: (i) 5 : 1, (ii) 10 : 1, (iii) 15 : 1, (iv) 1 : 5, (v) 1 : 10, (vi) 1 : 15, (vii) 1 : 2, (viii) 1 : 0, (ix) 0 : 1	Whilst the sample prepared with 1 : 2 Cu/Bi ratio with HMT fuel crystallized into $CuBi_2O_4$	
	Another experiment was conducted at 1 : 2 Cu/Bi mole ratio using HMT fuel at 1 : 1 Φ ratio	The authors reported a decrease in porosity after annealing. The BET surface area of the samples prepared by urea at different Cu/Bi ratios was reported as: 3.2 $m^2\ g^{-1}$ for the sample prepared by Cu/Bi mole ratio of 5 : 1, 2.5 $m^2\ g^{-1}$ for the sample prepared by Cu/Bi mole ratio of 10 : 1, 2.4 $m^2\ g^{-1}$ for the sample prepared by Cu/Bi mole ratio of 15 : 1, 0.7 $m^2\ g^{-1}$ for the sample prepared by Cu/Bi mole ratio of 1 : 5, 0.8 $m^2\ g^{-1}$ for the sample prepared by Cu/Bi mole ratio of 1 : 10, and 0.6 $m^2\ g^{-1}$ for the sample prepared by Cu/Bi mole ratio of 1 : 15	
	The samples were annealed at 600 °C	The study showed that not only the composite but any of the component either CuO or α-Bi_2O_3 in excess can be synthesized by one-pot SCS process. Importantly the nanocomposite showed improved photoelectrochemical activity compared with pure $CuBi_2O_4$ The sample prepared by Cu/Bi mole ratio of 15 : 1 with urea outperformed all other samples due to improved charge carrier separation	

optimal performances at equivalence ratio or Φ value equal to unity (*i.e.*, $\Phi_e = 1$). We particularly analyzed the phase and morphological characteristics, band gap and generation of oxygen vacancies in SCS-derived powders. The gas evolution during the combustion reaction is significantly influenced by the type of fuel and its concentration. In general, the releasing gases result in the production of smaller and less agglomerated particles. We consider that the selection of fuel is also critical to induce oxygen vacancies in the powders produced by the SCS method.

6. SCS and applications of photocatalysts

The SCS-synthesized metal oxides and supported metal oxide structures are widely explored in photocatalytic applications including photocatalytic water treatment and photocatalytic hydrogen production *via* water splitting. Herein, we have focused on SCS-developed metal oxides for photocatalytic water purification.

6.1 SCS development of binary metal oxide photocatalysts

A lot of work has been done on metal oxides such as TiO_2, Al_2O_3, ZnO, CuO, CeO_2, Fe_2O_3, MnO_x and Bi_2O_3. Low cost, abundance, biocompatibility, and high efficiency have made these candidates favourable for various applications ranging from biological applications such as drug delivery, to gas sensing and energy storage applications. TiO_2 and ZnO have been the pioneering materials in photocatalytic applications. The properties of these metal oxides depend upon the preparation method. As discussed in the above section, SCS is a single-step process and has the basic advantage of *in situ* altering the chemical and physical makeup of the derived product by changing the reaction parameters.[189] Therefore, the method has been widely applied to tailor the properties of binary oxides.[4,48,190–198]

ZnO is an extensively studied semiconductor with a direct bandgap of ~3.37 eV. The optoelectronic properties of ZnO make it a potential candidate for applications in the blue/UV range of the light spectrum. However, owing to its ~3.37 eV bandgap, the photocatalytic activity and efficiency of ZnO is limited in visible light. Additionally, the photocatalytic efficiency is also subject to its shape, morphology, particle size, surface area, surface defects *etc.*[199] The search for economical and eco-friendly production routes is important for its potential industrial use.[200–204] Different fascinating shapes and morphologies of ZnO have been synthesized so far including nanowires, nanoparticles, nanoflowers, nanoplates, nanorods, highly porous honeycomb-like structures *etc.*, *via* the SCS method.[118,189,205–209] In a recent study, Mane *et al.*[210] reported SCS synthesized 3D flower-like ZnO nanostructures employing *m*-cresol as fuel at stoichiometric ratio with zinc nitrate. FE-SEM images of 3D flower-like nanostructures at different magnification show that the nanostructures contain porous petals Fig. 28(a–e). These petal-like sheets with high porosity can provide a high surface area for photocatalytic reactions as well as trapping and utilizing the incident and scattered light. Fig. 28f also shows the presence of only Zn and O without any impurity elements.

Potti *et al.*[211] reported an interesting study for the development of ZnO photocatalysts using different fuels including citric acid (CA), dextrose, glycine, oxalyl dihydrazide, oxalic acid and urea. All the obtained samples showed a standard hexagonal wurtzite structure with the lattice constants a = 3.25 Å and c = 5.21 Å. However, the derived ZnO samples showed peculiar morphologies and surface area. Among all the ZnO samples, the ZnO prepared by oxalic acid showed improved photocatalytic degradation of orange G compared

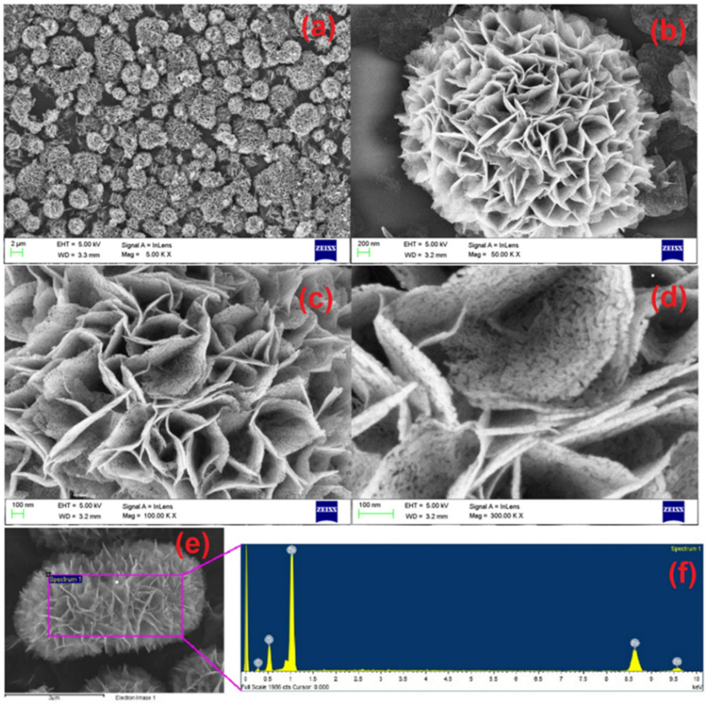

Fig. 28 (a–e) SEM images of SCS synthesized 3D flower-like ZnO at different magnification, (f) EDX (energy dispersive X-ray) spectra of SCS-synthesized 3D flower-like ZnO. This figure has been adapted from ref. 210 with permission from Springer Nature, copyright 2021.

with the other ZnO samples. Azizi *et al.*[212] reported green MW-assisted SCS of ZnO nanopowders for biomedical applications. SCS was carried out using fruit, pulp extracts and seeds of the *Citrullus colocynths* plant as fuel. The morphology of the ZnO powders was changed by changing the type of fuel in the SCS reaction. Flower-like ZnO was obtained using *C. colocynths* fruit-derived fuel, hexagonal ZnO was obtained from seeds, and block-shaped ZnO nanostructures were obtained using pulp as a fuel. The size variation of the as-synthesized ZnO nanostructures investigated by TEM was 85–100 nm, 20–35 nm, and 30–80 nm produced by fruit, seeds, and pulp as fuel, respectively. The bandgap of the ZnO nanostructures also changed with morphology. The flower-like ZnO showed a minimum bandgap of 3.25 eV, while the measured bandgap observed for hexagonal and block-like ZnO was 3.4 eV and 3.28 eV, respectively.

One well-known semiconductor that exists with various stochiometric and crystalline structures is iron oxide. Among its extensively studied phases, α-Fe_2O_3 (hematite), γ-Fe_2O_3 (maghemite), Fe_3O_4 (magnetite) and FeO (wustite),[55] α-Fe_2O_3 is the most stable phase under ambient atmospheric conditions.[213,214] It is an n-type semiconductor with a reported bulk bandgap of ~2.1 eV. The characteristic rust-red colour of α-Fe_2O_3 is due to its strong absorption of yellow to UV light photons and transmission of orange to infrared photons. Owing to its low cost, abundance, high thermal stability, multiple functionalities and striking physical and chemical properties, α-Fe_2O_3 has been widely investigated for a variety of applications. Also, magnetite has been diversely studied for its distinct magnetic properties. The narrow bandgap of α-Fe_2O_3 allows it to absorb light up to 600 nm (*i.e.* ~40% of the solar light), hence making it a promising candidate for photocatalytic applications.[215] In view of such striking advantages, different phases and morphologies of iron oxides have also been produced by the SCS method.[131,173,216–222] Deshpande *et al.*[131] reported the synthesis of well-crystalline α-Fe_2O_3, γ-Fe_2O_3 and Fe_3O_4 through the SCS method. According to the study, changing fuel (glycine, hydrazine and CA) and optimizing the fuel-to-oxidizer ratio "Φ" resulted in the phase changes. The iron oxidation state of SCS-derived iron oxide products decreases by increasing the molar ratio of glycine to ferric nitrate "Φ". In other research, Wang *et al.*[223] synthesized pure Fe_3O_4 nanoparticles at a glycine to ferric nitrate ratio of 0.7 with average grain size of 57 nm and high saturation magnetization of 89.17 emu g^{-1}.

The development of materials that are economical and abundant is of great importance. Titania (TiO_2) is the naturally occurring oxide of titanium and ~95% of titanium ore is processed into TiO_2. It has been extensively used in industry including in paint, inks, paper, textile dying, batteries, as a UV ray absorber in cosmetics, in food additives, sensors, capacitors *etc.*[224] In addition, TiO_2 has also been widely studied for its applications in water and air remediation and for self-cleaning surfaces. The bandgap structure of TiO_2 features a valence band constructed from O 2p orbitals and conduction band constructed from Ti^{4+} 3d orbitals with a bandgap energy of 3.2 eV. Among the various methods employed for the production of TiO_2 nanoparticles, the SCS method is a very successful method.[200,225,226] Chung *et al.*[227] reported three different types of TiO_2 nanopowder fabrication by the SCS technique by varying fuels (glycine, urea, thiourea) for the dye-sensitized solar cell (DSSC) application. The performance of SCS-synthesized TiO_2 was compared with a DSSC prepared from Degussa P25 TiO_2. The results showed that TiO_2 synthesized by SCS method worked better as a photoelectrode for DSSCs. The optical properties of TiO_2 made it an attractive candidate for photocatalysis. Among the three polymorphic structures of TiO_2 (*i.e.* rutile, anatase and brookite), rutile and anatase have been widely studied for photocatalysis, whereas brookite is rarely used. The major difference between anatase and rutile is that anatase consists of (101) as prevailing facets while the prevailing facets for rutile are (110). The reported bandgap of rutile is a little smaller than that of anatase, *i.e.*, 3.03 eV and 3.20 eV, respectively.[228,229]

Challagulla *et al.*[228] reported SCS of nano TiO_2 using glycine, urea and oxalyldihydrazide (ODH) as fuels. The combustion was also carried out by varying the fuel-to-oxidizer ratio. XRD analysis showed that SCS carried out with glycine as a fuel resulted in TiO_2 crystallizing only in the anatase phase, whereas urea and ODH resulted in mixed anatase and rutile polymorphs. The SCS-synthesized mixed phase showed improved photocatalytic degradation of MB compared with the pure phase SCS-synthesized TiO_2. The morphological tuning of SCS-synthesized nanoparticles can also be done for enhancement of photocatalytic activity. Nagaveni *et al.*[230] employed the SCS method to obtain nanocrystalline TiO_2 with lower bandgap employing three different fuels, namely glycine, hexamethylenetetramine (HMT), and oxalydihydrazide (ODH). All the SCS-synthesized TiO_2 exhibited a lower bandgap and higher surface area than commercial Degussa TiO_2. Importantly, the SCS-synthesized TiO_2 showed higher visible light photocatalytic activity towards MB degradation than commercial TiO_2.

Eswar *et al.*[231] demonstrated that the photocatalytic efficiency of TiO_2 can be further improved by conducting modifications in SCS-synthesized TiO_2. For this purpose the authors employed the same synthesis procedure as used by Nagaveni[230] to obtain TiO_2 nanopowder with L-ascorbic acid fuel. The SCS-synthesized TiO_2 was processed to obtain TiO_2 nanobelts, which were further acid etched in a subsequent step (Fig. 29). The acid etching tuning resulted in the formation of a large volume of pores and hydroxyl radicals. The inactivation of harmful bacteria and degradation of MB and methyl orange (MO) were studied in the presence of TiO_2 nanobelts under solar irradiation. The study revealed that the hydroxyl radicals formed by acid etching assisted the rapid degradation of both organic dyes and bacteria. Hence the acid-etched TiO_2 nanobelts resulted an excellent candidate for photocatalytic water purification.

Among various metal oxides, WO_3 is a very active and visible-light-responsive candidate for photocatalysis, with a reported bandgap of 2.8 eV.[232–236] WO_3 is an n-type semi-

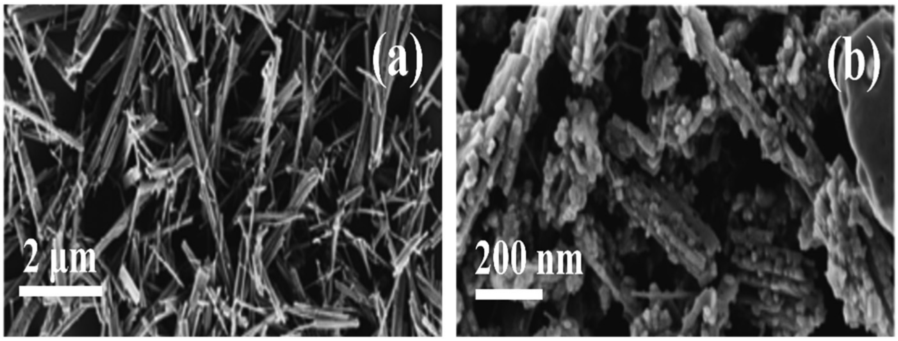

Fig. 29 SEM images of (a) pristine TiO_2 nanobelts, (b) acid-etched nanobelts. This figure is adapted from Eswar *et al.*,[231] with permission from RSC, copyright 2015.

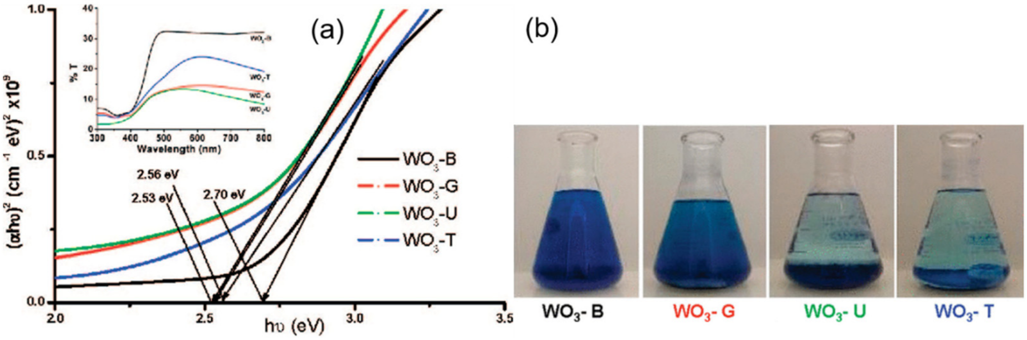

Fig. 30 (a) Tauc plots showing the bandgap of WO_3 obtained from glycine (WO_3-G), urea (WO_3-U), thiourea (WO_3-T) and their comparison with the benchmark comercial (WO_3-B). Inset shows UV-Vis spectra for various SCS-synthesized WO_3 samples, (b) visual images of degradation of MB photocatalyzed by SCS-synthesized WO_3-B, WO_3-G, WO_3-U, and WO_3-T. This figure has been adapted from ref. 121 with permission from ACS, copyright 2008.

conductor with a variety of oxygen-deficient "WO_{3-x}" (sub)stoichiometric materials such as $W_{20}O_{58}$, $WO_{2.9}$, $W_{18}O_{49}$, W_5O_{14}, $WO_{2.72}$, $W_{24}O_{68}$, *etc*. However, WO_3 is reported to be the most stable and highly efficient for visible light photocatalysis compared with other stoichiometries.[237] Various methods have been deployed to synthesize WO_3 nanoparticles. However, the SCS technique for the synthesis of WO_3 nanoparticles was first employed in 2008 by Morales *et al.*[121] using three different fuels: glycine, urea and thiourea, labelled as WO_3-G, WO_3-U, and WO_3-T, respectively. The SCS-synthesized WO_3 samples were relatively darker in color than commercial WO_3 (WO_3-B). Quantitative analysis carried out by UV-visible (UV-vis) spectroscopy showed higher absorption at wavelengths longer than band-edge cut-off for all three SCS-synthesized WO_3 compared with the commercial WO_3-B powder (Fig. 30a and inset). The SCS technique also assisted in enhancement of the light absorption characteristics of WO_3 nanoparticles in the visible light wavelength range. In Fig. 30a a clear redshift can be seen in the bandgap of WO_3-G, WO_3-U, and WO_3-T which comes out between 2.53 eV–2.56 eV compared with the bandgap of benchmarked commercial WO_3 (WO_3-B). Photocatalytic tests showed that all the SCS-synthesized WO_3 samples showed improved photocatalytic activity towards MB degradation compared with the commercial WO_3-B sample (Fig. 30b).

Chen *et al.*[136] detailed the photocatalytic activity of SCS-prepared mesoporous $W_{18}O_{49}$ (G3) nanoneedles synthesized by glycine fuel, a WO_3 (U3) sample produced from urea fuel and rod-like $W_{18}O_{49}$ (UC3) tungsten oxide synthesized from the mixture of urea and CA as fuels. Among the three samples, G3 and UC3 showed good intrinsic absorption in the UV region (Fig. 31) due to the oxygen-deficient stoichiometry of $W_{18}O_{49}$. For the oxygen vacancy-rich semiconductors, the absorption of visible light is explained based on surface plasmon resonance. Moreover, the samples showed excellent photodegradation over MB.

Aluminum oxide Al_2O_3 was first synthesized *via* SCS by Patil *et al.* in 1988 using urea as a fuel.[36] Later on, SCS-synthesized, aluminum-based oxides were prepared for photocatalytic applications.[238] Other metal oxides such as cobalt oxide,[239] tin dioxide,[240,241] cerium oxide,[6,7,181,242] and zirconium oxide[243,244] have also been prepared by the novel SCS method and have shown some potential as photocatalysts.

6.2 Modifications in pristine metal oxide photocatalysts *via* the SCS technique

It has been observed that suitable thermodynamic characteristics (such as appropriate bandgap and position of VB and CB) do not ensure higher photocatalytic performance. The

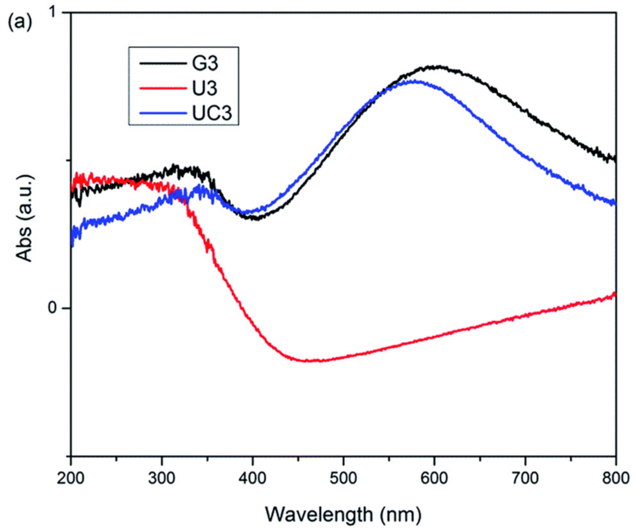

Fig. 31 Optical absorption spectrum of the G3 (glycine), U3 (urea) and UC3 (urea + CA) samples. This figure has been adapted from ref. 136 with prmission from RSC, copyright 2016.

overall photocatalytic efficiency is seen to depend on surface reaction kinetics as well as on the complex charge carrier dynamics. Any discrepancy in these factors may lead to low photocatalytic efficiency. To explain the charge carrier dynamics and reaction kinetics, the three aforementioned typical steps of photocatalysis can be further divided into the following steps: (i) absorption of incident light, (ii) creation of photoinduced electron–hole pairs, (iii) charge carrier transfer to the active sites on the surface, (iv) charge carrier recombination on the surface of the photocatalyst, (v) charge carrier recombination in the bulk, (vi) charge carrier trapping on the surface through surface redox reactions and (vii) charge carrier trapping on the surface by co-catalysts. Provided that η_{abs} is the light absorption efficiency, η_{cs} is charge separation efficiency, η_{cmt} is the charge migration and transport efficiency and η_{cu} is the charge utilization efficiency for surface redox reactions, the overall incident photoenergy conversion efficiency η_{c} can be written as:[245]

$$\eta_{\text{c}} = \eta_{\text{abs}} \cdot \eta_{\text{cs}} \cdot \eta_{\text{cmt}} \cdot \eta_{\text{cu}} \tag{16}$$

This shows that loss in the partial efficiency at any step will lower the overall photocatalytic efficiency. Considering the above-mentioned factors, modulation of the photocatalyst by inducing structural defects is suggested to improve their photocatalytic performance. The incorporation of defects under the optimal condition is known to play in photocatalysis the following major roles:

(1) Tune the bandgap of pristine metal oxide photocatalysis by imparting a defect state.

(2) Trap charge carriers and inhibit charge carrier recombination.

(3) Increase the active sites and enhance the adsorption of reactants such as pollutant molecules, O_2, CO_2, *etc.*

6.2.1 Incorporation of defects.

Recent research focus on defect engineering for the fabrication of highly efficient metal oxide photocatalysts has produced significant progress in this topic. All structural defects and irregularities are classified into four major divisions in accordance with the dimensions: (i) the zero-dimensional or point defects (such as vacancy generation or doping), (ii) one-dimensional defects also known as line defects (such as screw dislocation, edge dislocation), (iii) two-dimensional defects or planar defects (such as grain boundaries or twin boundaries), and (iv) three-dimensional defects (such as voids and lattice disorder). However, in this review we will discuss only those defects that are widely reported in SCS synthesized metal oxides.

6.2.2 Incorporation of oxygen vacancies in metal oxide photocatalysts *via* the SCS technique.

The SCS technique is known to generate defects such as vacancies, dislocations and stacking faults in the crystal structure.[246] Vacancies are the one of the prevalent defects in metal oxide semiconductor photocatalysts. In particular, oxygen vacancies are referred to as the *invisible friend of oxide electronics*[247] and are widely employed for the modification of the metal oxide surface for the rational design of photocatalysts. The introduction of oxygen vacancies is known to employ the so-called "doping effect".[248,249] In addition, oxygen vacancies suppress the electron–hole recombination rate and tune the conductivity of metal oxides. Moreover, these vacancies facilitate visible light absorption by creating an extra energy level just below the conduction band, thereby narrowing the bandgap of the semiconductor photocatalyst.[185] However, oxygen vacancies higher than the optimum value may act as charge carrier recombination centers and reduce the photocatalytic efficiency. Researchers have reported that heat treatment under a hydrogen environment is a facile way to introduce oxygen vacancies in metal oxides. The vacancies are thus introduced by liberating oxygen from the crystal lattice under a low-oxygen environment at elevated temperature. Therefore, chemical reduction is often preferable. In an ideal TiO_2 crystal, the removal of an oxygen atom is often accompanied by neighboring atoms so that the electrostatic balance is maintained in the material. If the removed oxygen atom is represented by O^r, V''_O represents the corresponding empty site (or oxygen vacancy), V'_O shows the empty site formed due to the removal of an oxygen atom with a localized single electron, $[Ti^{4+}]$ shows the exposed neighbouring Ti^{4+} at the oxygen vacancy and $[Ti^{3+}]$ shows the exposed Ti reduced by excess electrons due to oxygen removal, the mechanism is described by the following reactions:

$$2Ti^{4+} + O^{2-} \rightarrow 2[Ti^{4+}] + \frac{2e^-}{V''_O} + O^r \tag{17}$$

$$[Ti^{4+}] + e^- \rightarrow [Ti^{3+}] \tag{18}$$

$$V''_O + e^- \rightarrow V'_O \tag{19}$$

$$[Ti^{4+}] + V'_O \rightarrow [Ti^{3+}] + V''_O \tag{20}$$

The mechanism shows that when oxygen is removed from the TiO_2 crystal it generates V''_O, which further generates V'_O

and reduces the exposed neighbouring metals.[249,250] Ever since the first discovery by Chen *et al.*,[251] great interest has been triggered towards the development of oxygen vacancy-rich black TiO_2 owing to its IR energy absorbability. Ullattil *et al.*[252] demonstrated a one-pot SCS technique as a successful method to obtain black anatase (TiO_{2-x}) using titanium butoxide and diethylene glycol precursors. The defective anatase was observed to constitute various oxygen vacancies and Ti^{3+} sites, which played a decisive role in photocatalytic degradation of MB under solar light illumination.

Chen *et al.*[122] demonstrated the development of amorphous carbon-coated tungsten oxide with high defect concentration *via* solution combustion synthesis. The synthesis was carried out by using ammonium paratungstate as tungsten precursor, ammonium nitrate as reducing agent, and glycine as fuel and glucose was utilized as the source of carbon. The synthesized photocatalyst was tested for MB degradation. The authors reported that the amorphous carbon and defects on the tungsten oxide surface synergistically assisted in achieving total degradation of MB in just 40 min. Karthik *et al.*[253] showed MW-assisted synthesis of ZrO_2 for photocatalytic study of MB and RB dyes as well as antibacterial studies. The authors demonstrated that SCS-synthesized ZrO_2 exhibited dislocation-rich defects as monitored by PL analysis. In addition, the as-synthesized ZrO_2 also exhibited a PL peak at 589 nm due to intrinsic defects such as oxygen vacancies. The literature shows that metal and non-metal atom doping are often also accompanied by generation of oxygen vacancies at the lattice sites of metal oxides and induce various types of visible light responses in the parent metal oxide. The effect of metal and non-metal doping on photocatalytic performance is discussed in the next section.

6.2.3 Vacancy generation in carbon-supported metal oxide photocatalysts. Ever since carbon was found to exhibit good reducibility at high temperatures over 600 °C, researchers have been trying to combine metal oxides with carbon to introduce oxygen vacancies. In addition, owing to the excellent MW absorbability of carbon, MW combustion synthesis provides a fast and controlled processing route to synthesize vacancy-rich metal oxide–carbon composites and hybrids. Similarly, Wan *et al.*[254] successfully developed oxygen defect-rich metal oxides (V_2O_5, WO_3, TiO_2, and Nb_2O_5) through the MW combustion technique. Suresh *et al.*[255] described the synthesis of defect-rich zirconium oxide supported on activated carbon by MW-assisted combustion synthesis. The authors reported that the oxygen vacancy sites, structural defects of ZrO_2, and charge carrier transmission capability of the SCS synthesized catalyst resulted in enhanced photocatalytic activity towards textile dye degradation from wastewater. The PL spectra of all activated carbon-supported ZrO_2 samples showed emergence of subordinate bands due to fast evaporation, partial oxidation, and rapid crystallization during MW heating. However, these bands were absent in the pure ZrO_2 sample.

6.2.4 Incorporation of pores. It is well established that defect-induced surfaces such as hierarchical macro and meso porous structures or core–shell structures assist in efficient electron–hole separation and improved light absorption capability.[256] Such structures enhance the photocatalytic efficiency through light scattering and multiple reflections within the pore channels and the interior of cavities of photocatalysts. Particularly, in photocatalysis often surface defects created during synthesis significantly affect the photocatalytic performance.[257]. The SCS technique has shown an excellent capability in synthesizing foamy porous structures (Fig. 32) due to escaping gases during the synthesis[173,204,258–263] and the possible template role of the organic fuel.[10,264]

In addition, the porosity can be controlled by monitoring the synthesis parameters such as fuel ratio, type of fuel, solution pH and final calcination temperature. Hao *et al.*[265] successfully employed gel combustion synthesis for the synthesis of single-phase $LaFeO_3$ using urea as fuel. The authors reported that a low calcination temperature in combustion synthesis results in a highly porous $LaFeO_3$ structure. Three different samples were prepared by varying the calcination temperature from 200 °C to 400 °C. However, the highest porosity was obtained by the sample calcined at 200 °C. The increase in the calcination temperature resulted in a decrease in porosity. Moreover, the high porosity assisted in light absorption and faster photocatalytic reduction of aqueous chromium(VI) in visible light. Cao *et al.* also demonstrated the combustion synthesis of porous hematite nanoparticles of 20 nm average size that are efficient for degradation of MB. The authors described that the obtained porous structure displayed a continuous absorption band in the visible spectrum. Combustion synthesis is also reported to produce highly porous honeycomb-like oxide structures for improved photo-

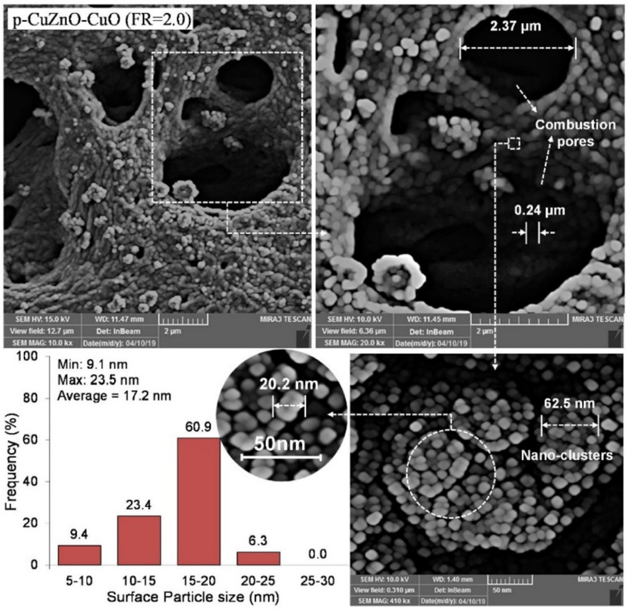

Fig. 32 SEM image showing incorporation of fine combustion pores in p-CuZnO–CuO obtained by SCS along with the histogram SEM particle size distribution. This figure has been adapted from ref. 263 with permission from Elsevier, copyright 2020.

catalytic activity.[209] Similarly, MW-assisted combustion synthesis has also produced porous structures that are highly desired in effective photocatalytic performance.[258] Another way to employ the combustion technique to boost photocatalytic activity is the combustion of colloidal solution, so-called colloidal combustion synthesis.[266] Voskanyan *et al.*[267] employed this combustion technique to obtain uniform mesoporous CeO_2 with tunable porosity using SiO_2 colloids. Colloidal particles assist in confining the combustion reaction in nano dynamics between the colloids, and also moderate the combustion reaction. The content of colloidal particles can be increased or decreased to tailor the porosity of the desired product. Fig. 33 shows schematics of how the colloidal SCS technique can be employed to tailor the porosity in metal oxide semiconductors. Shang *et al.*[268] obtained ordered mesoporous Ag/CeO_2 nanocrystals through the SCS technique and tuned the porosity by silica template. The silica template introduced many macro and mesopores in the resulting powders. SiO_2 has a melting point of 1600–1700 °C, which is generally higher than the typical SCS temperature. Hence silica resides in the SCS-derived product which can later be removed through NaOH solution treatment and leads to pore formation.

Template-assisted SCS is employed to produce ultra-small particles (*i.e.*, size below 5 nm). Manukyan *et al.*[269] synthesized ultra-small α-Fe_2O_3 nanoparticles through the SCS method over a mesoporous silica (SBA-15) template as shown in Fig. 34. The self-sustained combustion reaction propagates along the mesoporous template which was impregnated with iron nitrate, ammonium nitrate and glycine precursor solution. Finally, the template was removed to obtain α-Fe_2O_3 nanoparticles. The authors demonstrated that prolonging calcination from 2 to 6 hours promotes the growth of α-Fe_2O_3 nanoparticles. However, short-term combustion facilitates the synthesis of ultra-small nanoparticles.

6.2.5 Role of defects towards inhibition of charge carrier recombination. After the successful separation of electron–hole pairs, the other factor reported to limit photocatalytic performance is the charge carrier recombination. The charge carriers may recombine in the surface or bulk of the photocatalyst and become unavailable for redox reactions or even lead to the photocorrosion of photocatalysts. So far, reducing the probability of charge carrier recombination is one of the most important challenges in photocatalysis. Low specific area (and agglomeration) of catalyst particles is obviously another limiting factor of photocatalytic performance. It is reported to not only decrease the number of active surface sites but also inhibit the photocatalytic efficiency by retarding the mass transfer of reagents. The present literature on photocatalysis demonstrates that surface-related factors such as surface adsorption, kinetics of surface reactions, diffusion and charge carrier kinetics are very important in the rational design and development of a photocatalyst.[245,270] The photocatalytic performance of a material depends more on surface defects than bulk defects. The surface defects serve as traps for the photo-induced charge carriers and inhibit charge carrier recombination.

A variety of research has been focused on the key issues that limit photocatalytic activity. Suitable metal and non-metal doping, and the formation of composite structures represent major progress towards the solution of issues limiting the photocatalytic activity.

6.2.6 Doping with metal atoms in metal oxide photocatalysts. Incorporation of a small amount of foreign element into

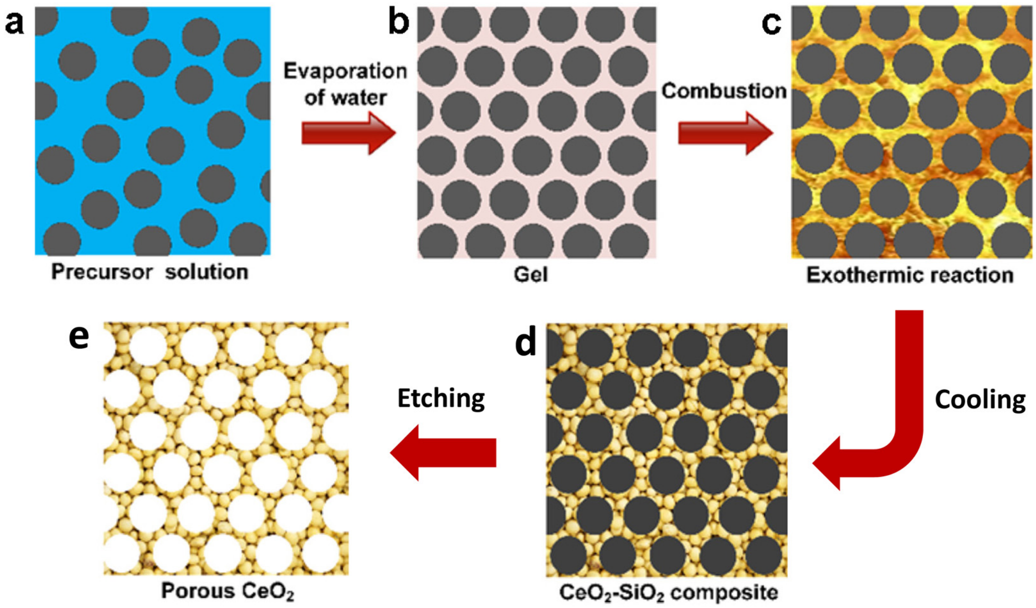

Fig. 33 Step-wise schemetic representation of colloidal SCS of mesoporous CeO_2 with tailored porosity. This figure has been adapted from ref. 267.

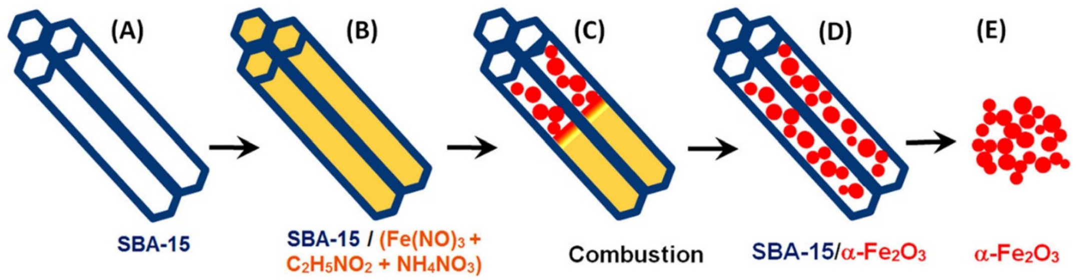

Fig. 34 Template-assisted SCS of α-Fe_2O_3 nanoparticles. This figure has been adapted from ref. 269 with permission from ACS, copyright 2014.

the host structure is known as doping. Doping in metal oxides is a common tool employed to boost the photocatalytic activity. TiO_2, ZnO, CeO_2, SnO_2 and ferrites are the common host metal oxides,[271] and the most widely employed dopants are transition metals, rare-earth, and alkaline earth metals. Doping in metal oxides is known to cause changes in the electronic structure which may lead to modification in the optical bandgap and electronic properties of the pristine metal oxides.[272] Importantly, structural defects such as oxygen vacancies induce oxygen vacancy states and assist in decreasing the bandgap, hence boosting visible light absorption of a photocatalyst.[273] Among several transition metals, the first row of transition metals and d^8 and d^9 metals are typically employed, where 3d orbitals of the dopant transition metal induce extra electronic energy states between the original bandgap of the metal oxide. However, a high level of doping may lead to a decrease in photocatalytic efficiency by introducing recombination centers that decrease the number of active charge carriers and make them unavailable for redox reactions.

As an example we discuss Cu, which is a first-row transition metal known to decrease the bandgap of wide bandgap semiconductors and hence extend the photoabsorption from the UV to the visible region. SnO_2 is known as one of the most dependable, superior and widely studied semiconductors for many applications; its bandgap (3.6 eV) restricts activation in visible light for photocatalytic applications. Babu *et al.*[274] reported that SCS is a successful method for the fabrication of Cu-doped SnO_2 quantum dots series. The bandgap of Cu-doped SnO_2 quantum dots showed a gradual decrease up to 2.2 eV whilst facilitating the visible light photocatalysis with the increase of Cu dopant content.

Mn, another first-row transition metal, is widely reported to reduce the bandgap of the parent metal oxide. The reduction in bandgap implies oxygen vacancy formation and the mechanism of charge transfer between the Mn and metal oxide. Babu *et al.*[275] showed in another study that the photocatalytic efficiency of Mn-doped SnO_2 quantum dots is 17 times higher than the photocatalytic efficiency of undoped SnO_2 quantum dots. The study suggested a decrease in bandgap of SCS-synthesized SnO_2 quantum dots compared with bulk SnO_2 (*i.e.*, 3.07 eV and 3.6 eV, respectively). Since the crystallite size of SnO_2 quantum dots is nearly equal to the Bohr radius of SnO_2 (2.7 nm), the bandgap of SnO_2 quantum dots should be increased due to quantum confinement because of the smaller crystallite size of SnO_2 quantum dots than that of the bulk SnO_2. However, the defects and higher concentration of oxygen vacancies caused a significant decrease in the bandgap energy of SnO_2 quantum dots.[276] The absorption of SnO_2 is gradually red-shifted into the visible region with the addition of Mn^{4+}, as displayed in Fig. 35. The reduction in bandgap energy with increasing Mn^{4+} content could be due to the charge transfer between SnO_2 and Mn^{4+} cations. This indicates the presence of sp–d exchange interactions between the sp electrons and localized d electrons of Mn^{4+} ions due to substitution of Sn^{4+} ions. Thereby, increasing the visible light absorption capability of Mn-doped SnO_2 through SCS facilitates the visible light photocatalysis.

6.2.7 Doping of rare-earth elements. Owing to unique physical and chemical characteristics, rare-earths including yttrium, scandium and fourteen elements of the lanthanide series have attracted huge attention during the last few decades.[277–279] The rare earths are known for their down-conversion (*i.e.*, converting high-energy photons into lower-energy

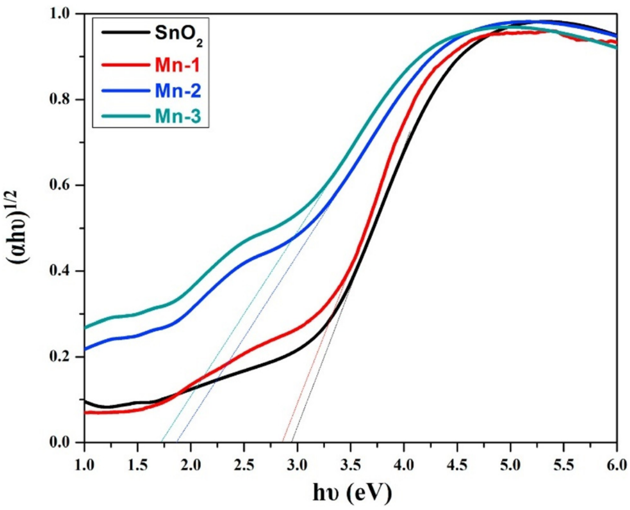

Fig. 35 Optical spectra of undoped and Mn-doped SnO_2 quantum dots. This figure has been adapted from ref. 275 with permission from Elsevier, copyright 2018.

photons) and their up-conversion (*i.e.*, ability to emit higher-energy photons upon excitation by lower-energy photons). The sharp spectral characteristics of rare earths have made them popular phosphors. It is well established that rare-earth metal oxide doping in binary metal oxides results in enhanced photocatalytic activity by modifying the optical features and delaying the deactivation time of the parent metal oxide photocatalyst.[280–283] Additionally, the 4f electrons of lanthanides are reported to configure with the parent metal oxide and prevent electron–hole recombination.[284] The rare earths occupy the Ti sites in the crystal lattice of the parent TiO_2 and lead to the formation of Ti^{3+} and oxygen vacancies.[280] The literature shows that SCS is a promising technique for the synthesis of rare-earth-doped metal oxides for photocatalytic application.[284–286] Xiao *et al.* reported higher photocatalytic performance of Sm^{3+}-doped TiO_2 prepared by the SCS method. It was observed that all the Sm^{3+}-doped TiO_2 showed significant visible light absorption compared with undoped TiO_2. However, 0.5 mol% Sm^{3+} doping was the most suitable loading in titania for efficient photocatalytic performance towards MB due to the maximum content of surface oxygen vacancies. With the further rise in Sm^{3+} doping the oxygen vacancy content was reduced, which led to a decreased photocatalytic performance. A similar observation of enhanced photocatalytic efficiency of Sm-doped ZnO nanoparticles compared with undoped ZnO nanoparticles was reported by Faraz *et al.*[283] The authors demonstrated the SCS technique for obtaining the undoped ZnO nanoparticles and 1%, 3% and 5% Sm-doped ZnO nanoparticles using CA monohydrate fuel. All the Sm-doped ZnO nanoparticles showed higher photoabsorption. Notably, the Sm doping in ZnO nanoparticles resulted in an absorption band in the visible region (Fig. 36a) and lower bandgap (Fig. 36b) than undoped ZnO nanoparticles. The photocatalytic tests towards Malachite green (MG) degradation revealed that the optimum doping content of Sm in ZnO is 3% (Fig. 36c).

Ahmad *et al.*[282] have reported successful SCS of Eu-doped ZnO, Tb-doped ZnO and Eu and Tb co-doped ZnO nanoparticles for photocatalytic applications. The photoluminescence (PL) characteristics of all the samples showed a peak at 580 nm. The yellow emission depicts the exciton transition between the photoaccelerated electrons and charged O vacancy in the ZnO valence band. The PL spectra show that the yellow emission of the Eu and Tb co-doped ZnO is less than that of undoped ZnO nanoparticles (Fig. 37). This shows a decrease in electron–hole recombination which ultimately improves the photocatalytic efficiency.

Rare-earth-doped ternary metal oxides have also been reported in the literature. Liang *et al.*[286] described the development of a broad spectrum for Bi/BiOBr:Yb,Er/C ternary composite in the photocatalytic degradation of Rhodamine B (RhB), phenol and imidacloprid under visible, NIR or solar light exposure. The photocatalysts were produced through one-pot combustion synthesis utilizing CA as fuel and carbon source, whilst pure BiOBr was obtained by using urea fuel. The study demonstrated the successful doping effect of Er^{3+}/Yb^{3+} into the BiOBr lattice and the spontaneous formation of Bi nanoparticles and carbon species during the synthesis. The UV-visible-NIR absorption response of the synthesized samples was observed to increase in the sequence of BiOBr < Bi/BiOBr/C < Bi/BiOBr:Yb,Er/C. The improved broad range of absorbance of Bi/BiOBr:Yb,Er/C was attributed to $^2F_{5/2} \rightarrow {}^2F_{7/2}$ tran-

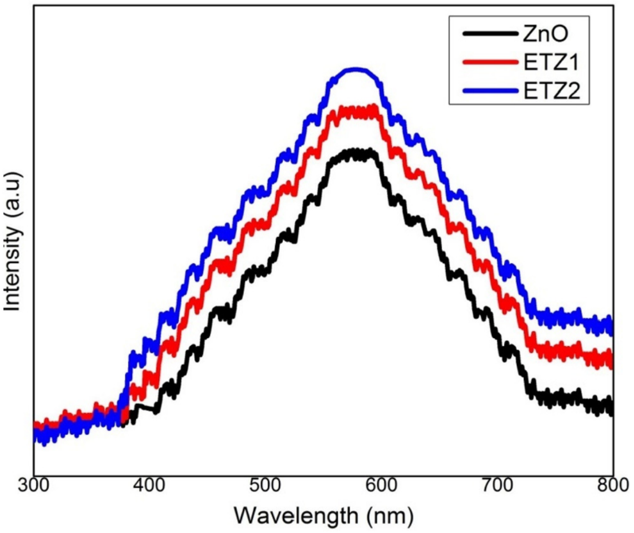

Fig. 37 PL spectra of SCS-synthesized ZnO and ETZ photocatalyst. This figure has been adapted from ref. 282 with permission from Elsevier, copyright 2020.

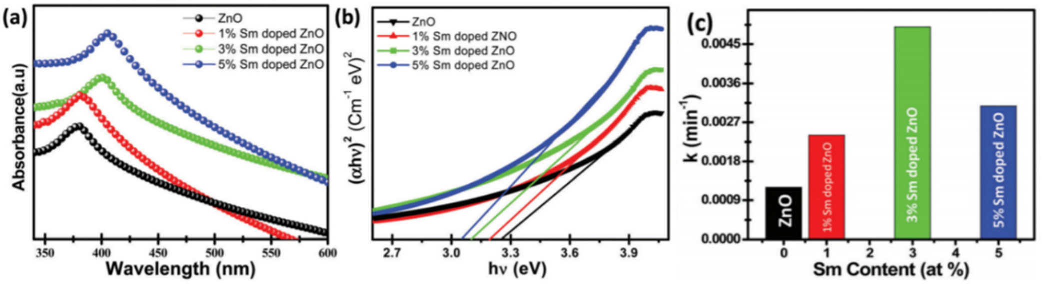

Fig. 36 (a) UV-vis absorbance, (b) bandgap analysis, (c) photocatalytic activity of SCS-synthesized ZnO and Sm-doped ZnO nanostructures. This figure has been adapted from ref. 283 with permission from RSC, copyright 2018.

sition of Yb^{3+} and $^4F_{7/2} \rightarrow ^4I_{15/2}$ transition of Er^{3+}. Additionally, the enhanced photocatalytic activity was also ascribed to the combined effect of surface plasmon resonance effect of metallic Bi, up-conversion transition of Er^{3+} and formation of a heterojunction.

6.2.8 Doping with non-metal atoms. Besides metal doping, doping with non-metal elements such as N, C, F, B and S is reported to reduce the bandgap energy of wide bandgap metal oxides and thereby facilitating the visible light absorption photocatalyst.[287,288] The non-metal atom can exist as an interstitial dopant, or it may replace the oxygen or metal sites in the parent metal oxide. The 2p orbitals of these non-metal dopant atoms contribute to the generation of mixed or localized energy states near the VB edge. The non-metal dopant acting as an impurity also results in defect generation, which contributes to modifying the optical characteristics of the parent metal oxide. Asahi and co-workers[289] were the first to demonstrate that nitrogen-doped TiO_2 exhibits visible light photocatalytic activity towards MB and gaseous acetaldehyde. First principles and XPS studies showed that nitrogen doping into substantial sites narrows the bandgap of TiO_2, which allows visible light absorption in nitrogen-doped TiO_2.

Typically, among non-metal elements, nitrogen is considered one of the most important p-type dopants with additional features of non-toxicity and abundance. Nitrogen doping replaces a portion of oxygen atoms, which imparts a new dopant energy level between VB and CB which triggers new excitations and red-shift in optical absorption. In some studies, carbon doping displayed more effective photocatalytic applications.[290,291] Carbon doping in the crystal lattice of metal oxide is also reported to enhance the visible light activity of the photocatalyst by imparting an extra energy level between VB and CB. Sakthivel *et al.* demonstrated that carbon-doped TiO_2 exhibits superior photocatalytic activity to nitrogen-doped TiO_2 under visible light.[292,293]

The main technique involved in carbon doping in TiO_2 requires sufficient calcination temperature for the carbon to diffuse into lattice sites. However, in solution combustion synthesis, nitrogen and carbon incorporation is straightforward because the adopted fuels constitute these elements and the high combustion temperatures favor the doping of the aforementioned elements at the lattice sites of the metal oxide crystal.[115] Moreover, in SCS the dopant atoms can remain within the lattice. Mani *et al.*[294] developed carbon-doped TiO_2 using ascorbic acid and CA as fuels. The bandgap of carbon-doped TiO_2 obtained by CA (2.8 eV) was less than the bandgap of carbon-doped TiO_2 obtained from ascorbic acid (3 eV). However, both the bandgap values were less than that of commercial TiO_2. Xiao *et al.*[295] investigated the effect of calcination temperature in the SCS development of carbon-doped TiO_2 photocatalysts using a mixture of ethylene glycol and CA fuels. The study showed that the bandgap energy of the developed carbon-doped TiO_2 catalysts became monotonically narrower with increase in calcination temperature, and the smallest bandgap was achieved by the sample heat-treated at 600 °C. The authors deduced that the decrease in bandgap energy of carbon-doped TiO_2 may be due to the presence of Ti^{3+} species. The other reason for visible light photocatalytic activity could be the presence of the Ti–O–C structure in carbon-doped TiO_2 nanocrystals. The presence of Ti^{3+} species may lead to generation of oxygen vacancy states below the conduction band in the developed carbon-doped TiO_2 nanocrystals. Moreover, the carbon-doped TiO_2 developed at 600 °C also resulted in generation of the highest number of $^{\bullet}OH$ radicals per unit surface area, which are highly important in achieving efficient photocatalytic activity. Due to the aforementioned factors the carbon-doped TiO_2 developed at 600 °C exhibited the highest photocatalytic activity towards MB degradation. In another study, Xiao *et al.*[296] obtained carbon-doped TiO_2 by SCS using a mixture of CA and ethylene glycol fuel. The enhanced visible light photodegradation of MB was attributed to the formation of Ti^{3+} species and oxygen vacancy states in the carbon-doped TiO_2.

ZnO is an important direct wide bandgap semiconductor and exhibits a band edge position similar to that of TiO_2, thereby ZnO is also subjected to similar non-metal doping by the SCS method. Researchers reported that such modifications in ZnO also lead to an increase in photocatalytic performance.[297] Zheng *et al.*[298] reported nitrogen doping in ZnO nanocrystals utilizing urea as the main fuel and source of nitrogen whereas CA was used to adjust the combustion process and control the growth of crystallites. The results showed that a small quantity of CA has excellent coordination with urea in accelerating nitrogen doping in TiO_2 and in obtaining perfect nitrogen-doped ZnO nanocrystals of 30–50 nm size with uniform colour. In another study, Zhang *et al.*[299] reported *in situ* carbon doping using urea as carbon source and zinc acetate as zinc precursor with variable zinc acetate to urea ratios. Carbon doping resulted in bandgap reduction from 3.19 eV to 2.72 eV. Moreover, a decrease in the electron–hole recombination rate was observed through weaker PL peak intensity. These collective features of carbon doping and oxygen vacancy generation enhanced the photocatalytic performance of carbon-doped ZnO nanostructures towards MB degradation.

6.2.9 Localized surface plasmon resonance (LSPR) effect induced *via* the SCS technique. Another important method to activate the metal oxide photocatalyst under visible light is surface plasmon resonance (SPR). SPR is the electromagnetic quantum phenomenon that occurs when incident light interacts with free electrons at the metal nanoparticle–dielectric interface. The energy carried by incoming photons is transferred to the free (itinerant or conduction) electrons of the metal nanoparticles causing them to collectively excite at a specific resonance frequency.[300] The plasmonic effect in metal particles arises when their size is reduced to the nano-regime. Heterostructures of noble metal nanoparticles with metal oxide semiconductors (such as Ag–SiO_2, Ag–TiO_2, Au–ZnO[301–305]) have shown strong visible light absorption and boost the photocatalytic activity of the metal oxide semiconductor. However, SPR can also be triggered in metal oxides by carefully tuning free electron concentration such as by doping.

Ansari *et al.*[306] developed pure ZnO and Ag/ZnO nanocomposites *via* a rapid SCS route using $Zn(NO_3)_2{\cdot}6H_2O$ and $Ag(NO_3)_2{\cdot}6H_2O$ as Zn and Ag precursors and CA fuel. The nanocomposites were prepared by 1% and 3% Ag doping. After drying, the precursor gel underwent auto combustion at 100 °C to produce Ag/ZnO nanocomposites. DRS analysis showed that the absorption of Ag/ZnO nanocomposites was higher than that of pure ZnO. Additionally, a peak broadening was observed with increasing concentration of Ag which triggered photocatalytic activity of the developed nanocomposites in visible light. The 3% Ag/ZnO nanocomposite showed the highest photocatalytic activity for MB degradation due to the SPR effect of Ag nanoparticles in the Ag/ZnO nanocomposites. The effect has also been reported in other SCS-synthesized metal oxide photocatalysts. Shang *et al.*[268] demonstrated this effect over the silica-templated SCS of CeO_2 and ordered mesoporous Ag/CeO_2 nanocrystals. The photocatalytic activity of the synthesized nanocrystals was investigated for RhB degradation. The RhB degradation efficiency increased with the rise of Ag doping content. The authors stated that one of the factors responsible for improved photocatalytic efficiency of Ag/CeO_2 was the SPR effect. The photoinduced electrons are accepted by Ag/CeO_2 and the lifetime of charge carriers increases due to the SPR effect.

6.3 Synthesis of ternary and complex metal oxide photocatalysts

Among the above-mentioned popular pristine metal oxides, one major challenge is to improve the photocatalytic efficiency and to harvest visible light for photodegradation due to the wide bandgap. Even if the bandgap is in the visible range, there is room for enhancement of the photocatalytic performance by limiting the electron–hole recombination rate which increases in binary low bandgap metal oxides. The literature shows that the SCS technique is capable of synthesizing single-phase ternary oxides or complex metal oxides through a one-pot synthesis.[165] In addition, SCS can be employed to obtain either nanoparticles (metal nanoparticles or metal oxide nanoparticles) or nanocomposites just by adjusting the synthesis parameters.[103,307–309]

It is quite well established that synthesizing suitable mixed metal oxides may address the grand challenge of harvesting solar energy. In this view, ternary and quaternary metal oxides form a new class of functional materials for enhanced and efficient photocatalytic performance. Some quaternary and complex metal oxides have also been targeted for the development of advanced visible-light-active photocatalysts using solar light. Studies showed that the SCS method is one of the successful methods for producing complex oxides.[20,50,310] Du *et al.*[311] demonstrated the successful combustion synthesis of $Bi_5O_7NO_3$ and Ag-decorated $Bi_5O_7NO_3$ owing to the potential of Bi-containing oxides in photocatalysis.[192] They showed that Ag presence plays a vital role in the photocatalytic decomposition of MO. The Ag content of 5% led to 1.5 times higher photocatalytic activity than undecorated $Bi_5O_7NO_3$. Samu *et al.*[312] discussed the combustion synthesis parameters for obtaining pyrochlore phase $Bi_2Ti_2O_7$. The authors further described the bandgap engineering of the material by carefully adding foreign Fe^{3+} or Mn^{2+} ions in the precursor solution to produce $M_xBi_{2-x}Ti_2O_7$ (where x: 0.01, 0.05, 0.1, 0.25, 0.5 and M denotes: Fe or Mn). The reactions were observed to be incomplete at lower fuel-to-oxidizer ratio, therefore the ratio was adjusted to 2. A decrease in the bandgap and gradual alloying with the inclusion of increasing metal ions were observed. Moreover, the surface area also increased with higher concentration of metal ions. The photocatalytic activity of SCS-synthesized $Bi_2Ti_2O_7$ was observed to outperform P25 TiO_2. However, despite higher photoabsorption, a lower photocatalytic activity was obtained *via* metal-alloyed photocatalysts. The authors attributed the decrease in photocatalytic performance to the electronic properties of the material.

The literature shows that the SCS technique has been a successful synthesis technique for the development of binary and complex ferrites that are extensively explored for photocatalytic applications.[114,313–317] Nguyen *et al.*[114] produced magnesium ferrite nanoparticles *via* the SCS technique. The developed particles showed good photocatalytic activity towards MB degradation. Meena *et al.*[318] demonstrated the successful SCS development of sunlight-responsive, single-phase cubic undoped and Cu-doped manganese ferrite $MnFe_2O_4$ nanoparticles using oxalyl dihydrazide (ODH) fuel. The synthesized ferrite nanoparticles exhibited a spinel structure with spongy, porous and non-uniform morphology. The DRS studies showed the smaller bandgap of Cu-doped $MnFe_2O_4$ than pure $MnFe_2O_4$. Rabbani *et al.*[80] reported a simple MW SCS of pure $BiFeO_3$ crystalline nanopowders using metal nitrates and CA precursor. The derived powders showed a nearly cubic shape and a size distribution of 50–150 nm with a bandgap of 2.08 eV.

Tungsten oxide is known as an attractive candidate for visible light photocatalysis, and efforts have been made to enhance the visible light absorption by modifying pristine tungsten oxide. The literature clearly shows evidence that shifting the band edge position will influence the bandgap, the redox potential of valence and conduction bands of tungsten oxide and hence its photocatalytic activity. This can be done by incorporating metal cations into the WO_3 structure, thereby modulating the interfacial energetics. Such a modification may narrow the bandgap of a material without altering the redox potential of photogenerated charge carriers. Thomas *et al.*[137] showed successful reaction of Zn, Cu, and Ag with WO_3 to form $ZnWO_4$, $CuWO_4$ and Ag_2WO_4, respectively, *via* the SCS technique (Fig. 38).

WO_3 can be crystallized into one of the following structures upon the addition of a heteroatom: (i) wolframite (in the case when the divalent cation is smaller, such as Zn and Cu with ionic radius <0.77 Å), and (ii) scheelite (in the case when the divalent cation is larger). Other possible structures could contain monovalent cations. Cu and Zn both are likely to form a monoclinic wolframite crystal structure. W and Zn form octahedral WO_6 and ZnO_6 joined by edge sharing.[319] $CuWO_4$ forms the triclinic $P\bar{1}$ crystal structure in such a way that both W and Cu are neighbored by six oxygen atoms to form octa-

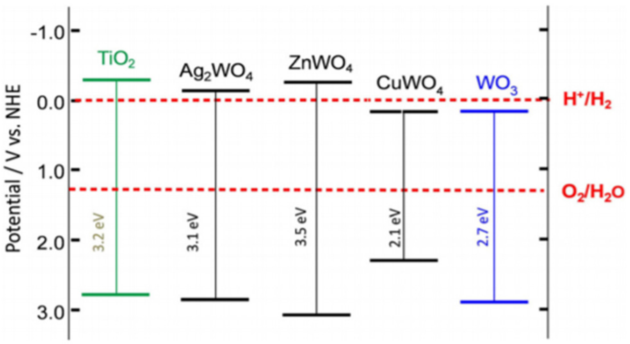

Fig. 38 Approximate VB and CB edge positions of SCS-synthesized tungstates along with interfacial energies of WO_3 and TiO_2 shown for comparison. This figure has been adapted from ref. 137 with pemission from Wiley, copyright 2015.

hedral WO_6 and CuO_6.[320] The two octahedra are joined by edge-bridging oxygen atoms. Even though the associated structure of $CuWO_4$ is monoclinic wolframite with $P2/c$ symmetry,[321,322] the octahedral CuO_6 exhibits Jahn–Teller distortion to remove the degeneracy of Cu^{2+} 3d orbitals. This distortion extends the octahedron which results in the reduction of symmetry from monoclinic to triclinic.[322] Conversely, adding Ag, a monovalent cation in the WO_3 structure facilitates a complex structure Ag_2WO_4. Among the three α, β and γ-Ag_2WO_4, γ-Ag_2WO_4 is thermodynamically the most stable phase (belongs to $Pn2n$ orthorhombic symmetry).[323] All tungsten atoms configure to form octahedral WO_6, W_2O_6, and W_3O_6, and are joined by edge sharing. However, in α-Ag_2WO_4, all W atoms are coordinated only to six O atoms, which form distorted $[WO_6]$ clusters with an octahedral configuration, a symmetry group O_h, and octahedron polyhedra (6 vertices, 8 faces, and 12 edges).[324] Reports show that the fabrication of such materials has been mostly carried out by conventional methods.[325–328] However, the SCS method turned out to be the most efficient and convenient method for *in situ* incorporation of heteroatoms into pristine tungsten oxide. Many other bimetallic oxides[329] and even $Co_{1-x}Ni_xWO_4$ wolframite-type mixed oxides[330] have been also prepared by the SCS method.

These studies clearly demonstrate that SCS-synthesized nanopowders of complex metal oxides can be accomplished and that they are potential candidates for advanced photocatalytic applications.

6.4 Synthesis of nanocomposites for photocatalytic applications

One of the main challenges in the synthesis of nanocomposites is the successful integration of two different materials with distinctive structures to yield unique heterostructures with diverse functionality. In this context, several varieties of hybrid nanostructure have been synthesized. SCS is a very successful and low-cost method for the synthesis of nanocomposites and hybrid nanomaterials. Furthermore, the combustion synthesis technique can produce complex composites in one step without pre and post-treatment steps.[331] On the other hand, besides the advantages of making hybrids through combustion synthesis, one drawback is the appearance of unexpected (or unwanted) intermediate phases, which can be avoided by optimizing the synthesis parameters. Making nanocomposites/heterostructures such as metal oxide–metal oxide nanocomposites,[332–334] metal oxide composites with graphene oxide (or other carbon-based materials) and other complex composites may be very useful in photocatalysis. Several possible reasons can be considered: (i) it may facilitate photocatalysis by favouring the electron–hole migration within a heterostructure by inducing an internal electric field at the interface of photocatalysts,[335] (ii) heterostructure formation by SCS can make electron–hole pair separation more efficient, hence generating a greater number of electron–hole pairs,[336,337] (iii) it can also reduce the electron–hole recombination rate, (iv) it can prolong the lifetime of charge carriers,[336] or (v) it may enhance the light absorption of the composite, hence increasing the efficiency of a photocatalyst.

Facilitating charge transfer within a heterojunction is the one prime advantage of making heterojunctions.[159,338,339] Bajiri *et al.*[335] demonstrated that ZnO can be coupled with a suitable semiconductor to fabricate a direct Z-scheme photocatalyst. For this purpose, a CuO/ZnO/g-C_3N_4 heterojunction was synthesized *via* the SCS route. In general, two schemes are proposed for charge migration in a heterostructure when illuminated with light: (i) heterostructure approach, and (ii) Z-scheme approach. When the light is irradiated on the CuO/ZnO/g-C_3N_4 heterostructure, the electrons from the valence band of CuO, ZnO and g-C_3N_4 are photoexcited to their conduction bands. According to the heterostructure scheme (Fig. 39a), the photogenerated electrons from both CuO and g-C_3N_4 transfer to the conduction band of ZnO, hence their redox potential is decreased. In contrast, the electrons in the conduction band of ZnO have enough potential (−0.2 V) to produce super oxides $^{\bullet}O_2^-$ (−0.046 V). Since the valence band of CuO is at a more negative potential than the valence band of ZnO and g-C_3N_4, the photogenerated holes from ZnO and g-C_3N_4 travel to the valence band of CuO. These holes do not have enough potential (0.4 V) to produce $^{\bullet}OH$ radicals (1.99 V *vs.* NHE at pH 7). On the other hand, according to the Z-scheme, the photogenerated electrons from the ZnO conduction band combine with the holes in the valence band of both CuO and g-C_3N_4. Thus, the electrons accumulated in the conduction band of CuO and g-C_3N_4 have enough redox potential (−0.77 or −1.12 V) to generate species. Also, the holes left in the conduction band of ZnO have adequate potential to generate $^{\bullet}O_2^-$ radicals. Therefore, the enhanced photocatalytic activity of CuO/ZnO/g-C_3N_4 is explained based on the Z-scheme approach (Fig. 39a).

Recently, many studies have focused on coupled metal oxide semiconductors in which two or more different metal oxides are coupled together to form heterojunctions, owing to their higher photocatalytic efficiency than single-metal oxides.[340,341] Upon photoillumination both the metal oxides excite simultaneously and transfer the electron to the low-lying CB of one metal oxide, whilst holes shift to the less anodic VB. This allows efficient electron–hole separation, which plays a

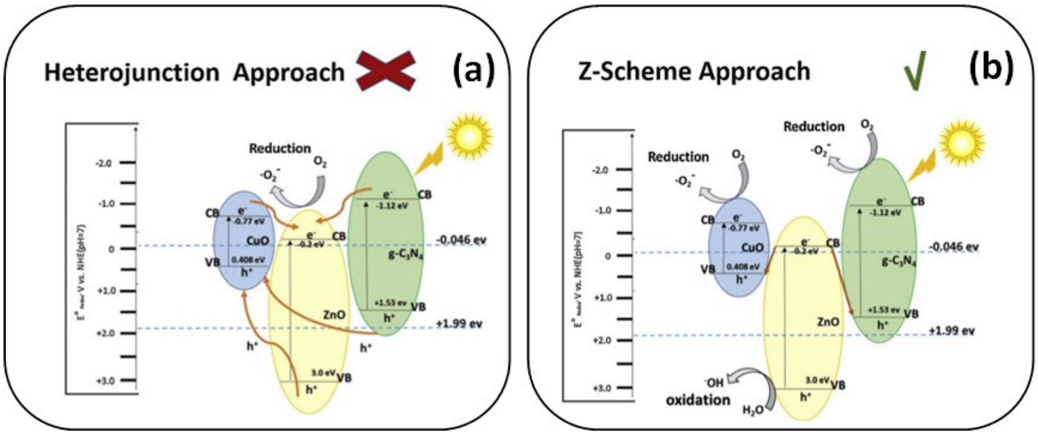

Fig. 39 Schemetic representation of the charge transfer mechanism in CuO/ZnO/g-C_3N_4 (a) Z-scheme, (b) heterojunction approach. This figure has been adapted from ref. 335 with permission from Elsevier, copyright 2019.

leading role in enhancement of photocatalytic efficiency.[244] The literature shows that even if the bandgap is increased upon making the composite, the photocatalytic performance of the composite can still be better than that of the pristine binary metal oxide.[342] This can be explained by band bending at the interface of photocatalysts and formation of an electric field which can facilitate the charge separation. However, in the case of wide-bandgap oxides (*e.g.*, ZnO and TiO_2), beside band bending-induced enhancement, their visible light absorption can also be enhanced when they are coupled with lower bandgap oxides.

Abbasi *et al.*[263] developed ZnO and p-CuZnO–CuO *via* combustion synthesis for photodegradation of textile effluents. However, a more effective and efficient photodegradation by the p-CuZnO–CuO composite than pure ZnO was observed because of the improved photoabsorption of the composite. The incorporation of CuO with ZnO led to the absorption of light in the visible spectrum. Additionally, the incorporation of copper nanoparticles led to the SPR effect (Fig. 40). The developed nanocomposite also showed a lower recombination rate, which demonstrates the efficient electron transfer between the p–n junction and Cu nanoparticles. All the factors collectively favor enhanced visible light photocatalytic activity.

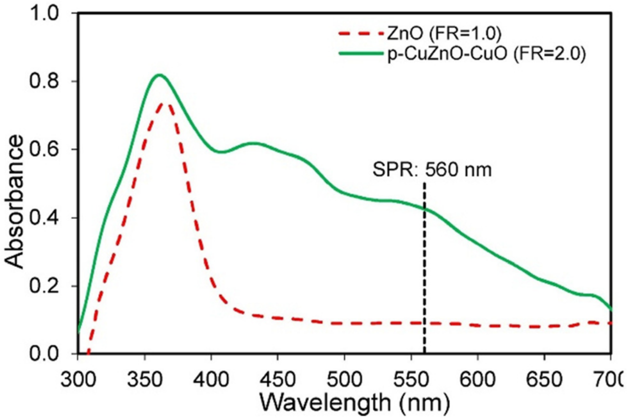

Fig. 40 Optical absorption spectra of p-CuZnO–CuO synthesized at fuel-to-oxidizer ratio (FR) 1 and 2. This figure has been adapted from ref. 263 with permission from Elsevier, copyright 2020.

The increased efficiency of the nanocomposite is also attributed to the efficient separation of the photogenerated electron–hole pairs. Manimozhi *et al.*[343] coupled ZnO with well-known CeO_2 to develop a CeO_2–ZnO nanocomposite *via* the SCS route. The authors proposed that electrons from CeO_2 would excite first when the photocatalyst is exposed to a light source. Since the CB edge positions of CeO_2 and ZnO lie closely, this allows efficient separation of photogenerated electrons from the CB of CeO_2 to CB of ZnO, which results in improved photocatalytic efficiency of the developed nanocomposite. Singh *et al.*[344] suggested an optimum loading of WO_3 on TiO_2 for higher photocatalytic degradation than SCS synthesized WO_3 and commercial TiO_2. The study demonstrated the production of the WO_3–TiO_2 composite by loading SCS-synthesized WO_3 on commercial TiO_2 by physical mixing. According to the experimental findings, the photocatalytic performance varied with the loading of WO_3 on TiO_2 and the highest degradation rate was achieved with the 15 wt% WO_3–TiO_2 composite for anionic and cationic dyes under UV and visible light irradiation. Other complex metal oxide–metal oxide composites like $SrFe_{12}O_{19}$–$SrTiO_3$[345] have also been developed by the SCS technique for photocatalytic applications.

Several reports show that CeO_2–TiO_2 heterojunctions are efficient for photocatalytic applications. However, the visible photocatalytic activity can be further enhanced by modifying this heterojunction with metal or non-metal atoms by increasing the electron–hole separation and by extending the energy range of photoexcitation.[346,347] Basha *et al.*[348] reported the influence of phosphorous doping in CeO_2–TiO_2 during SCS. It was observed that the absorption edge of P–CeO_2–TiO_2 showed a gradual red shift with increase in synthesis temperature from

400 to 600 °C, hence decreasing the bandgap value from 2.98 to 2.93 eV. Another study by Sha *et al.*[346] showed a gradual decrease in the bandgap energy of SCS-synthesized CeO_2–TiO_2 modified with Ni and P. The bandgap energies calculated from Kubelka–Munk plots for CeO_2–TiO_2, Ni–P/TiO_2, Ni–P/CeO_2 and Ni–P/CeO_2–TiO_2 were 3.05, 2.75, 2.70 and 2.40 eV, respectively, as shown in Fig. 41. The improved photocatalytic efficiency of Ni–P/CeO_2–TiO_2 compared with the other samples is also attributed to its lowest charge transfer resistance and highest surface area. The impedance studies showed the smallest semicircle Ni–P/CeO_2–TiO_2, hence depicting the lowest charge transfer resistance of Ni–P/CeO_2–TiO_2 (calculated through the arc at the low-frequency region in Nyquist plots[349]).

Construction of p–n heterojunctions has also been discussed in the literature for efficient photocatalytic activity.[350,351] Bhange *et al.*[351] demonstrated TiO_2 heterojunction formation with p-type metal oxides such as Bi_2O_3 *via* the SCS method to form Bi_2O_3/TiO_2. The authors found that the type of fuel and its concentration influence the synthesis of this heterojunction material. The study revealed that when the SCS process was fueled by urea, only cubic Bi_2O_3 was the crystalline product whilst TiO_2 remained amorphous. However, the phase and composition of the final product was influenced by varying the glycine fuel concentration. When glycine was used in a 1 : 1 metal-to-fuel ratio $Bi_4Ti_3O_{12}$ was obtained. A mixed phase of $Bi_4Ti_3O_{12}$ and β-Bi_2O_3 was obtained when glycine concentration was doubled. A further increase in the concentration of glycine suppressed the formation of the $Bi_4Ti_3O_{12}$ phase whilst α-Bi_2O_3, β-Bi_2O_3 and TiO_2 were the main phases in the final product. An enhanced photocatalytic activity showed the mixed phase $Bi_4Ti_3O_{12}$–β-Bi_2O_3 for MB degradation as well as for H_2 production *via* water splitting. The authors attributed the increase in the photocatalytic activity to the formation of the $Bi_4Ti_3O_{12}$–β-Bi_2O_3 p–n junction which resulted in lowering of the recombination rate of photogenerated electron–hole pairs.

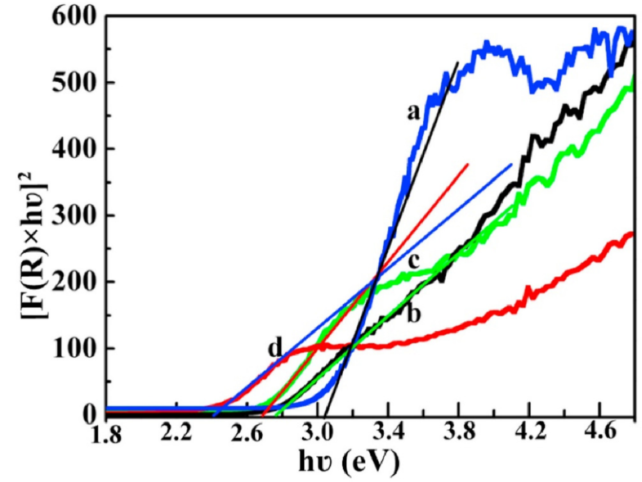

Fig. 41 Bandgap energies of (a) CeO_2–TiO_2, (b) Ni–P-decorated TiO_2, (c) Ni–P-decorated and (d) Ni–P-decorated CeO_2–TiO_2. This figure has been adapted from ref. 346 with permission from Elsevier, copyright 2020.

The band alignment in ternary metal oxide–metal oxide nanocomposite photosystems promotes migration of electrons by facilitating double type-II nature excitations.[352] Bhoi *et al.*[353] demonstrated the single-step synthesis of a ternary Fe_2TiO_5/α-Fe_2O_3/TiO_2 nanocomposite by the SCS process using different fuels including urea, glycine and hexamethylenetetramine at a fuel to oxidizer ratio of 1 and calcination temperature of 700 °C. The authors demonstrated the importance and influence of the type of fuel employed during SCS. They found that the final product was pure pseudo brookite Fe_2TiO_5 for urea fuel. However, under similar operating conditions, an Fe_2TiO_5/α-Fe_2O_3/TiO_2 ternary nanocomposite was obtained when the precursor solution was fueled by glycine or hexamethylenetetramine. The authors suggested a double type-II migration of charge carriers upon photoillumination. Therefore, the Fe_2TiO_5/α-Fe_2O_3/TiO_2 ternary nanocomposite showed improved photocatalytic activity compared with pure Fe_2TiO_5 due to enhanced visible light absorption and effective charge transfer.

6.5. Synthesis of carbon-based metal oxide composites for photocatalytic applications

Several studies have shown that the photocatalytic activity of pristine metal oxides such as TiO_2 and ZnO can be increased significantly when they are supported on activated carbon.[27,255,354,355] This section briefly describes the SCS of graphene-based MO composites and their photocatalytic performances.

Graphene is a single sheet of graphite, and is nearly an ideal 2D material with a remarkably high theoretical surface area of 2630 $m^2\ g^{-1}$ and high electrical conductivity. Its highly conductive robust structure, high porosity, and chemical stability often facilitate charge transfer and redox reactions.[313,356–358] Besides, carbon-based materials generally possess a high specific surface area which can enhance the adsorption of contaminants on the photocatalysts. One way to utilize the extraordinary properties of graphene is to anchor graphene in composite materials. In graphene-based metal oxide photocatalysts, graphene behaves as a functional component or a substrate for immobilizing the other components. Recently graphene-based metal oxide nanocomposites have attracted considerable attention in the field of photocatalysis. When a metal oxide is coupled with graphene, the photogenerated electrons or holes in the metal oxide can efficiently transfer to the surface of grapheme, hence suppressing the probability of electron–hole recombination. These charge carriers can directly degrade the previously adsorbed contaminants on the graphene and/or produce reactive species such as hydroxyl or superoxide radicals.

Wang *et al.*[117] evaluated the photocurrent transient response and charge transfer of an SCS-synthesized graphene/ZnO nanocomposite and ZnO nanoparticles. A higher photocurrent was obtained by the graphene/ZnO nanocomposite, suggesting significantly improved charge separation and efficient migration of charge carriers through the graphene/ZnO nanocomposite compared with pure ZnO nanoparticles. Nyquist plots obtained by electrochemical impedance spectroscopy also showed the smaller semicircle of the graphene/ZnO nanocomposite than ZnO nanoparticles. This indicates a more efficient migration of charge carriers through the graphene/ZnO nanocomposite than pure ZnO nanoparticles. Moreover, the study also suggested the formation of pores and defects on the surface of graphene during SCS. In addition, the UV-vis diffuse reflectance spectra revealed the absorption edge of the graphene/ZnO nanocomposite with significant redshift compared with pure ZnO nanoparticles, hence boosting the photocatalytic performance. SCS is also used to produce metal oxide composites with reduced graphene oxide. Many researchers have reported graphene oxide-based metal oxide composites for enhanced photocatalytic activity. The graphene oxide sheet is also a potential candidate for supporting nanoparticles in liquid phase due to its hydrophilic nature in conjunction with the oxygen-containing functional groups present on its surface.

Gao *et al.*[115] employed the combination of graphene oxide with TiO_2 synthesized by the SCS method in the photocatalytic degradation of MO. The SCS technique was carried out using urea fuel at different furnace temperatures (300, 350, 400 and 450 °C). The reaction led to the successful synthesis of TiO_2 and to the partial reduction and nitridation of GO simultaneously by controlling combustion temperature. The sample prepared at 350 °C showed the highest photodegradation performance compared with the bare TiO_2. The higher photocatalytic activity of the GO–TiO_2 hybrid was attributed to active photogenerated charge transfer from TiO_2 to partially reduced graphene oxide as confirmed by PL quenching of GO-containing TiO_2. The same group later demonstrated a more facile one-pot MW combustion synthesis of graphene oxide–TiO_2 hybrids by following the same procedure for gel preparation, however the heat source was MW irradiation.[33] The MW-assisted combustion synthesis of GO–TiO_2 hybrids was faster than conventional combustion synthesis. The precursor gel was irradiated for 20 min under 700 W power MWs which resulted in partial reduction of GO, and at the same time nitrogen doping of TiO_2 and graphene was achieved. Moreover, the MW-assisted combustion-synthesized GO–TiO_2 hybrid also showed higher photocatalytic activity towards MO degradation in comparison with bare TiO_2. The PL analysis showed significant quenching with increasing GO content, suggesting efficient transfer of photoinduced electrons to GO and effective inhibition of charge carrier recombination, leading to more efficient photocatalytic activity of GO–TiO_2 as compared with bare TiO_2.

Kalantari Bolaghi *et al.*[359] reported that if the zinc nitrate, graphene oxide, glycine and CA mixture is combusted in a closed system, this would result in *in situ* reduction of graphene to produce a ZnO/RGO composite. The bandgap energy of as-synthesized ZnO/RGO was smaller than that of pristine ZnO nanoparticles, resulting in enhancement in photocatalytic performance for MB degradation. SCS-synthesized graphene composites with metal oxides such as TiO_2,[115] $NiFe_2O_4$[360] and other complex composites such as graphene–$CuFe_2O_4$–ZnO[336] are also reported in the literature for photocatalytic applications.

This section has highlighted the fascinating strategies and possibilities for modifying metal oxides through SCS, including the development of porous structures, utilization of dopants, and synthesis of ternary, complex and composite structures to improve their photocatalytic performances. A particular focus was given to the charge carrier separation and enhancement of optical properties of metal oxides produced by the SCS technique to gain further insight into the different approaches employed for efficient harvesting of solar light.

7. Safety considerations for the SCS technique

We have previously discussed that the SCS process involves a sequence of steps that can be combined in two major stages: (i) the solution mixing process (including the gelation process) and (ii) the combustion reaction. The solution mixing and the gel formation processes are relatively safe and do not require a high supply of energy. The second step, on the other hand, needs a small input of energy to achieve the ignition temperature of the redox mixture followed by the combustion reaction that may be highly intense, resulting in self-sustained high flame which rapidly propagates through the reactants. Fig. 42 shows the extent of exothermicity of the combustion reaction,

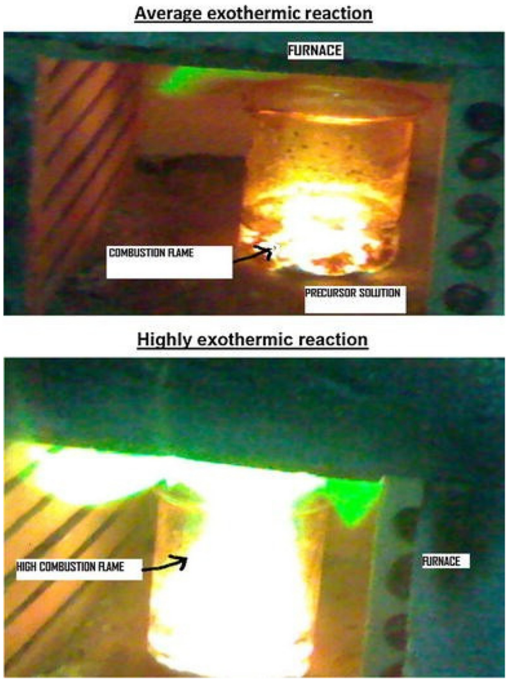

Fig. 42 Flame generation upon SCS inside a furnace. This figure has been adapted from ref. 361 with permission from Springer Nature, copyright 2014.

and the uncontrolled combustion reaction yields serious contamination issues by spreading the powdered and gaseous products from the reaction vessel into the environment. Moreover, besides the energetic reaction and potential environmental consequences, the sudden intensity of the experiment may also be dangerous for the experimenter, especially when material production is in large quantities. In this regard, special care must be taken for the identification of risk factors in the SCS process and essential safety measures that must be taken to prevent unfavorable and unforeseen circumstances.

(i) Type of fuel: It should be kept in mind that fuel plays a prime role in combustion synthesis. The nature of the fuel determines the intensity of the process. A variety of fuels have been investigated in the SCS technique, including glycine, hydrazine, urea/thiourea, CA, furfuryl alcohol, and carbohydrates among many other fuels. These fuels differ in heat of combustion, for example the heat of combustion of glycine is −975 kJ mol^{-1}, and for urea it is −632 kJ mol^{-1};[362] the combustion flame also depends upon the nature of the fuel. However, the nitrogen-containing fuels produce harmful gases during the SCS process. Moreover, nitrogen-containing fuels result in a more vigorous combustion reaction than carbohydrate fuels[165] owing to the higher exothermicity of nitrogen-containing fuel. Among nitrogen-containing fuels hydrazine, for instance, is toxic and results in a relatively violent reaction. Fig. 43(a–l) show the timed images of the violent SCS process carried out over a hot plate and fueled by carbohydrazide. The reaction was recorded for a period of 8 s; the ignition started

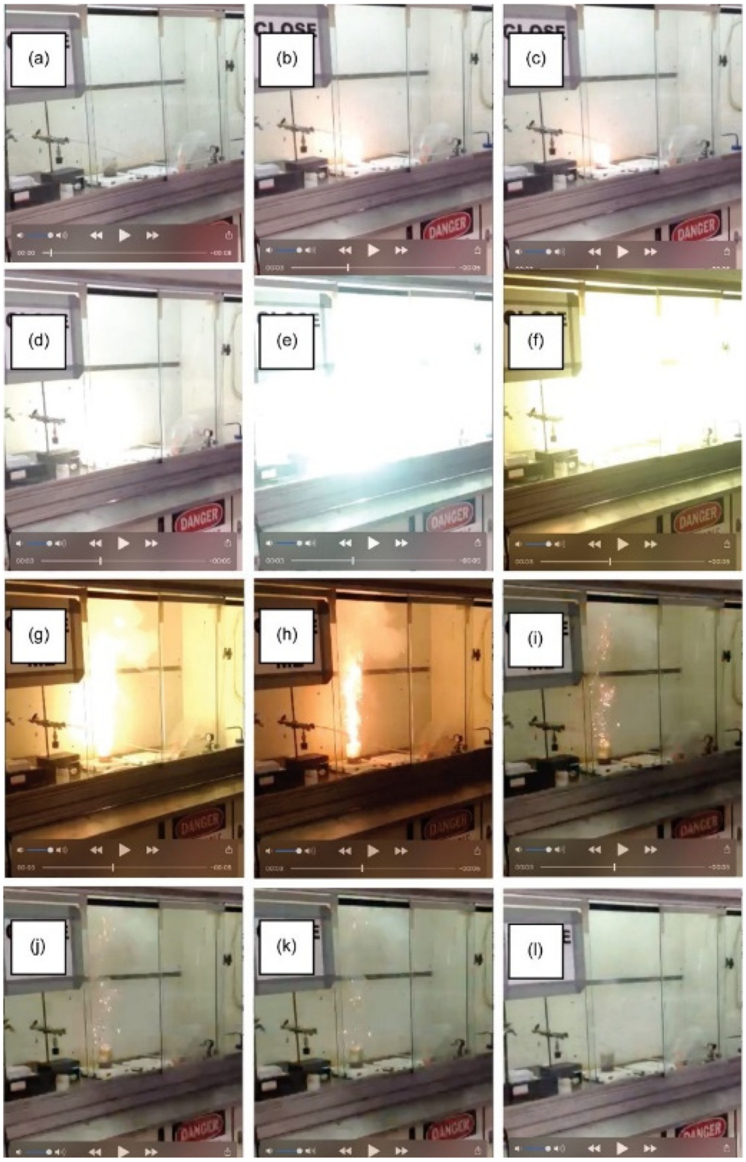

Fig. 43 (a) Timed images of SCS preparation of CaB_6 fueled by carbohydrazide; (a), (b) and (c) show ignition of the SCS mixture, (d), (e), (f) and (g) show the propagation of combustion, and (h), (i), (j), (k) and (l) show the cooling down process after intense combustion. This figure has been adapted from ref. 363 with permission from Taylor & Francis, copyright 2020.

at 5 s and lasted for approximately 2 s. Hence, safety precautions must be taken while employing carbohydrazide and nitrogen-containing fuels in general in SCS.

(ii) Fuel-to-oxidizer ratio: The oxidizer and the fuel are essential components of the redox mixture, which produces a complete combustion reaction, *i.e.* without requiring oxygen, when both the valences and the moles of the fuel and oxidizer are properly balanced.[97,361] Hence, the combination of stoichiometry and valence values to have a fuel-to-oxidizer ratio of the unit (*i.e.*, equivalence) is recommended for a complete combustion reaction. The principles of propulsion chemistry state that the maximum temperature during the combustion reaction can be obtained at Φ ratio of 1. However, for a vigorous combustion reaction at $\Phi = 1$, mixed fuel is sometimes recommended to lower the intensity of combustion and hence the risk of a potential violent combustion reaction. The adiabatic temperature of the flame and duration of flame emitted upon ignition during SCS increase with the rise in fuel concentration.[18,307] In addition, extreme fuel excess synthesis is usually not recommended owing to the excess release of CO and NO_x content.[170,364] The combustion temperature can be decreased by employing fuel-lean conditions due to dilution of fuel content in excess oxidizer.[365] Driving the combustion reaction under fuel-lean conditions also favors lowering of CO and NO_x emission, hence enhancing the greenness of the SCS technique.

(iii) pH of the precursor mixture: Several studies have clearly shown that the combustion intensity depends upon the pH of the precursor mixture.[102,366] The pH values close to 7 and below help to drive a safe and controlled combustion process, whereas higher pH of the precursor solution can influence not only the rate of combustion but also the potential fuel–metal interaction and precipitation of the metal precursors. In fact, the higher pH value results in rapid decomposition of the metal precursor and the formation of desegregated powders.[367] Therefore, the pH is also an important metric that needs to be considered to minimize the risk of energetic redox mixture during the combustion process.

(iv) Material of the combustion reactor: Interestingly, the material of the combustion reactor also significantly influences the combustion intensity. Combustion beakers having higher heat capacity are recommended for safe reaction. Deganello *et al.*[102] compared the SCS in three different combustion reactors made of Pyrex glass, sintered alumina and stainless steel. The results and observations showed that the reaction taking place in the stainless steel reactor displayed the lowest intensity of combustion, whereas the alumina reactor showed the highest intensity of combustion reaction. The authors demonstrated that this trend is due to different heat capacity and heat loss of the three materials. Therefore, the choice of an appropriate combustion reactor/beaker for SCS should be kept in mind for safety purposes.

(v) Design of the equipment: Most of the SCS of nanopowders uses relatively simple equipment and does not require special equipment. However, special equipment can also be used for the SCS technique.[368,369] In general, while employing the SCS technique special attention should be paid to the design of the combustion reactor, such that it contains a sufficiently wide opening for safe ventilation of the gaseous products that evolve during the combustion reaction. SCS should be carried out in a large-volume beaker which can provide enough space to accommodate the large-volume product that usually accompanies. Larger volume of product should be expected in a fuel-rich condition which leads to the formation of a spongy and porous network due to the evolution of a large volume of gases. Studies showed that even with a very calm combustion reaction taking place at low fuel-to-oxidizer ratio, only 80% of the product is obtained and the rest is lost to the environment with evolving gases. Powder loss can be minimized by placing a protective mesh over the reaction vessel, or by using special combustion equipment.[126,370] For a violent combustion reaction, the loss of the product is inevitable; however, in general a violent combustion synthesis is not recommended.

The basic purpose of this section is to make the reader familiar with the safety protocols of the SCS of nanostructured materials. The experimenter must consider the safety guidelines particularly during the combustion stage in which a large amount of heat – sometimes reflected in the generation of a flame – is produced when a large amount of nanopowder is to be synthesized. For this purpose, synthesis parameters and choice of equipment are important. The combustion vessel (beaker) should be large enough to accommodate a large volume of spongy products. The combustion reaction could be robust with a large amount of evolving gases, hence wide opening of the chamber is recommended to ensure proper ventilation. In general, low pH values and fuel-lean conditions

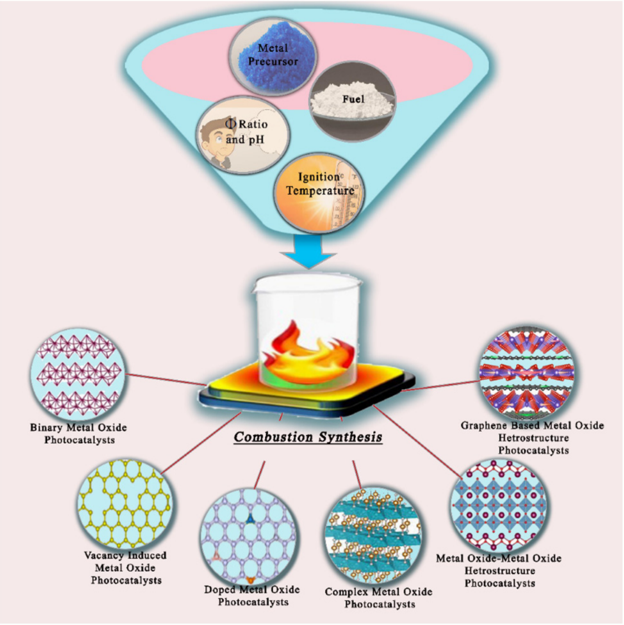

Fig. 44 Influence of SCS parameters on derived photocatalysts.

Table 2 Effect of SCS metrics on structural parameters of metal oxide photocatalysts and their photocatalytic activity

Material	Synthesis conditions	Photocatalytic conditions (light source and pollutant)	Remarks	Ref.
Bi_2O_3	$Bi(NO_3)_3·5H_2O$ + urea (or hydrazine) Urea and hydrazine produced monoclinic α-Bi_2O_3	UV light source. 0.1 g of product was added to 50 mL 5 ppm of RhB	Urea produced Bi_2O_3 with 0.14–10 μm particle size, 13 m^2 g^{-1} surface area and 2.73 eV bandgap whilst hydrazine synthesized Bi_2O_3 with 0.5–37.5 μm, 9 m^2 g^{-1} and 2.74 eV The photocatalytic degradation of RhB on urea synthesized Bi_2O_3 was 12% higher than that from Bi_2O_3 synthesized with hydrazine	192
$CaMoO_4$	$Ca(NO_3)_2·4H_2O$, molybdenum metal powder and CA (fuel) to oxidizer ratio 1 : 5. The samples were prepared at three different temperatures (*i.e.*, 400 °C, 500 °C and 600 °C)	UV light source. An aqueous suspension (100 mL) containing 10 ppm methylene blue and 0.15 g of product.	The SCS product showed crystallite size 16 nm (particle size 15–30 nm) and 45.4 m^2 g^{-1} at 400 °C. Surface area strongly decreased with increasing calcination temperature Crystallinity improved with increase in calcination temperature Highest degradation was achieved by sample calcined at 400 °C, the degradation efficiency decreased with the increase in calcination temperature	187
ZnO	$Zn(NO_3)_2·6H_2O$, the samples were prepared at different CTAB to oxidizer ratios (Φ): 0.5, 0.75, 1, 1.5	UV light source (8 W). 100 ml of 15 mg l^{-1} dye solution was photodegraded in the presence of 0.1 g of ZnO product	All the synthesized samples showed single-phase ZnO with no impurity peaks The samples prepared at $\Phi = 0.5$ showed crystallite size of 31 ± 2 nm, 21 m^2 g^{-1} surface area, 2.99 eV bandgap; $\Phi = 0.75$ leads to 23 ± 1 nm crystallite size, 28 ± 1 m^2 g^{-1} surface area, and 3.06 eV bandgap; $\Phi = 1$ leads to 23 ± 1 nm crystallite size, 35 m^2 g^{-1} surface area, and 3.11 eV bandgap; whilst the sample synthesized at $\Phi = 1.5$ produced 20 ± 1 nm crystallite size, 33 ± 2 m^2 g^{-1} surface area, and 3.13 eV bandgap Highest photocatalytic activity for MB degradation was achieved by sample prepared at $\Phi = 1.5$, the activity decreased with decrease in Φ value	184
ZnO	$Zn(NO_3)_2·6H_2O$ with urea fuel at four different Φ values: 0.6, 1, 1.8, 5.4; the samples were prepared at three different temperatures (*i.e.*, 400 °C, 500 °C and 600 °C)	UV source (850 W). Catalyst dosage: 2 g L^{-1}; orange-G dye solution: (500 mL) of 50 mg L^{-1}	Keeping the calcination temperature at 400 °C, the intensity of XRD peaks decreased with the increase in Φ value. Moreover, no structural peaks observed for the sample with $\Phi = 5.4$ calcined at 400 °C indicating that the provided temperature is not sufficient for combustion With $\Phi = 5.4$ and $\Phi = 0.6$, the increase in calcination temperature improved crystallinity of the ZnO nanopowder The study demonstrate that the sample synthesized at $\Phi = 1.8$ at 400 °C showed highest photocatalytic activity towards orange-G degradation For the samples prepared with excess fuel ($\Phi = 5.4$) and fuel-lean ($\Phi = 0.6$) conditions, 500 °C was suitable calcination temperature in order to get improved photocatalytic activity	204
Bi_2O_3/TiO_2, $Bi_4Ti_3O_{12}$	$Bi(NO_3)_3·5H_2O$, $Ti[OCH(CH_3)_2]_4$ with two different fuels (urea and glycine) at three different Bi : Ti : fuel ratios *i.e.* 1 : 1 : 2, 1 : 1 : 4 and 1 : 1 : 6. All the samples were calcined at 450 °C	Visible light mercury vapor lamp (400 W). For photocatalytic water splitting: 0.1 g catalyst was dispersed in 100 mL aqueous solution containing 25 mL methanol. For photocatalytic degradation test: 50 mg of photocatalyst sample was dispersed in 200 mL of 10 ppm aqueous MB dye solution	The samples prepared by urea showed Bi_2O_3 with cubic structure and TiO_2 remains as an amorphous phase. Whilst employing glycine fuel with the ratio 1 : 1 : 2 indicates the formation of $Bi_4Ti_3O_{12}$ type oxide phase By increasing glycine concentration to 1 : 1 : 4, $Bi_4Ti_3O_{12}$ phase decreased whilst β-Bi_2O_3 appeared. With further increase in glycine concentration to 1 : 1 : 6 $Bi_4Ti_3O_{12}$ phase disappeared and peaks of β-Bi_2O_3, α-Bi_2O_3, and TiO_2 appeared SEM showed well-distributed particles with an average size of 0.2–0.5 μm for all samples The samples prepared with urea at Bi : Ti : fuel ratios 1 : 1 : 2, 1 : 1 : 4, 1 : 1 : 6 showed a bandgap of 2.98 eV, 2.99 eV and 2.96 eV, respectively Whilst the samples fuelled by glycine at Bi : Ti : fuel ratio 1 : 1 : 2, 1 : 1 : 4 and 1 : 1 : 6 revealed bandgap of 2.9 eV, 2.4 eV and 2.75 eV, respectively The sample prepared *via* glycine fuel at a ratio of 1 : 1 : 4 showed higher photocatalytic activity for both photocatalytic H_2 production and for MB degradation	351

Table 2 *(Contd.)*

Material	Synthesis conditions	Photocatalytic conditions (light source and pollutant)	Remarks	Ref.
$BiFeO_3$	$Bi(NO_3)_3 \cdot 5H_2O$; $Fe(NO_3)_3 \cdot 9H_2O$ with the following fuels and their combinations at $\Phi = 1$. (i) Urea; (ii) glycine; (iii) CTAB; (iv) GU (glycine + urea); (v) GCTAB (glycine + CTAB). All the samples were calcined at 600 °C	Photodegradation of MB was evaluated in the presence of the as-calcined BFO powders under visible light radiation (two 100 W xenon lamps with a cutoff ultraviolet filter ($\lambda = 420$ nm)). 100 mL of MB solution (15 mg L^{-1}) was degraded by 0.1 g of BFO catalyst in the presence of 0.1 mL H_2O_2 (30%)	Sample combusted with urea fuel was amorphous because of lower decomposition temperature of urea. However, after calcination 100% $BiFeO_3$ phase was obtained. Mixed phases of $BiFeO_3$ and $Bi_{24}Fe_2O_{39}$ were obtained though combustion of CTAB and GCTAB fuels. The as-combusted powders obtained by glycine and GU fuels contained mixed phases of $BiFeO_3$ and $Bi_2Fe_4O_9$. The post calcination of all the samples resulted in $BiFeO_3$ as a major phase The average crystallite size of the samples prepared by urea, glycine, CTAB, glycine + urea, glycine + CTAB were 62 nm, 54 nm, 46 nm, 39 nm, 41 nm respectively whilst their bandgaps were calculated as 1.93 eV, 1.88 eV, 2.06 eV, 2.12 eV, 2.17 eV, respectively The highest photodegradation rate of MB under visible light irradiation was achieved in the presence of $BiFeO_3$ powders prepared by urea fuel alone in 100 min. This is attributed to their highest purity and crystallinity. The samples obtained by CTAB and GCTAB showed equivalent photocatalytic activity. However, the sample prepared by glycine fuel showed minimum photocatalytic activity	164
ZnO	$Zn(NO_3)_2$ with mixture of CA and DTAB fuels at four different Φ values: 0.5, 0.75, 1, 1.5. All the samples were calcined at 250 °C	UV source (8 W). MB concentration: 15 ppm catalyst dosage: 0.1 g per 100 ml	XRD analysis revealed the formation of high-purity ZnO samples at all fuel-to-oxidizer ratios with no additional peaks The average crystallite size, surface area and bandgap of the sample prepared at $\Phi = 1$ was 15 nm, 205 $m^2 g^{-1}$, 3.16 eV, whilst for the sample synthesized at $\Phi = 1.5$ was 9 nm, 371 $m^2 g^{-1}$, 3.17 eV, respectively. This last sample showed maximum adsorption capacity for MB however, the maximum photodegradation was obtained by $\Phi = 1$. This was attributed to larger bandgap and low light absorption capacity of sample with $\Phi = 1.5$	379
$BiVO_4$	Two vanadium precursors were used in combination with a bismuth precursor: (i) $Bi(NO_3)_3 \cdot 5H_2O + VCl_3$ or (ii) $Bi(NO_3)_3 \cdot 5H_2O + VOSO_4$ and also with three different fuels (urea, glycine, and CA) at $\Phi = 1$. The experiments were performed by setting the furnace temperature at 150 °C for combustion followed by annealing at 600 °C	Tungsten-halogen lamp (450 W). The photocatalytic assessment was made such that the UV portion of the lamp output was filtered out. An aqueous suspension of 250 ml of 50 μM methyl orange solution and the photocatalyst (dose: 2 g L^{-1}) was prepared for photocatalytic test	All the SCS produced samples were well matched with the reference sample. Some traces of V_2O_5 were observed employing VCl_3 precursor All the SCS-synthesized sample size ranges were in nano regime with the average crystallite size of ~34 nm whereas average particle size was ~94 nm. The specific surface area of samples obtained by precursor combination VCl_3 showed lower surface area employed by all the three fuels than precursor combination with $VOSO_4$. The range of surface area was given from 0.3 $m^2 g^{-1}$ to 1.35 $m^2 g^{-1}$ whilst for the commercial $BiVO_4$ was 0.45 $m^2 g^{-1}$ The bandgaps of $BiVO_4$ obtained by VCl_3 precursor with urea, glycine, and CA were reported as 2.17 eV, 2.22 eV and 2.23 eV, respectively, whilst the bandgaps of $BiVO_4$ obtained by employing $VOSO_4$ precursor were calculated as 2.34 eV, 2.39 eV and 2.44 eV, respectively. The authors reported the bandgap of commercial $BiVO_4$ as 2.36 eV, which is higher than the bandgaps of $BiVO_4$ obtained by VCl_3 precursor at all fuel conditions Higher photocatalytic activity for MO degradation was observed by all the samples obtained by precursor combination (i) than the samples obtained by precursor combination (ii). The samples prepared by CA fuel showed highest photocatalytic activity in both precursor combinations All the SCS-synthesized samples showed higher photocatalytic activity than commercial sample	380

Table 2 *(Contd.)*

Material	Synthesis conditions	Photocatalytic conditions (light source and pollutant)	Remarks	Ref.
TiO_2	$[TiO(NO_3)_2]$ with three different fuels glycine, urea, and oxalydihydrazide (ODH). All the experiments were performed at three different fuel concentrations, *i.e.* fuel-lean, 1 : 1 and fuel-rich conditions. The furnace temperature was maintained at 450 °C	Mercury vapor lamp UV source (125 W). 100 mL of 10 ppm of MB solution was prepared with 25 mg of the catalyst. The H_2 production from methanol was carried out with 50 mg of the catalysts	TiO_2 fueled by glycine during SCS crystallized in almost pure anatase phase in all the three conditions *i.e.*, fuel-lean, rich and stoichiometric ratios. The samples synthesized by urea fuel crystallized in mixed phase (anatase and rutile). The ratio of anatase and rutile phase was not affected by urea concentration. The samples synthesized by ODH also crystallized into mixed phase (anatase and rutile). Importantly, varying ODH concentration produced range of anatase to rutile mixture The TiO_2 fuelled by glycine showed smaller particle size at all fuel conditions. The reported bandgap of TiO_2 fuelled by glycine at fuel-lean, 1 : 1 and fuel-rich condition was 3.46 eV, 3.53 eV and 3.47 eV, respectively The type of the fuel was critical in controlling the photocatalytic performance towards MB degradation and H_2 production The TiO_2 prepared by urea and ODH fuel outperformed the TiO_2 prepared by glycine. This was attributed to the formation of mixed phase by urea and ODH fuels. However, for H_2 production, the pure TiO_2 synthesized by glycine fuel outperformed the mixed-phase TiO_2 powders	228
MoO_2	$(NH_4)_6Mo_7O_{24}$ with NH_4NO_3 as oxidizer and glycine fuel at five different fuel to oxidizer ratios 0.25, 0.5, 0.75, 1 and 1.25	300 W Xe lamp light source. The suspension was illuminated with a cut off filter (<420 nm) and an irradiation intensity of 100 mW cm^{-2}. MO, MB, RhB and phenol. Catalyst loading: 0.1 g. Dye concentration: 50 mL of 40 mg L^{-1}. Phenol concentration: 20 mg L^{-1}	The different Φ values lead to different products. Diammonium tetramolybdate $(NH_4)_2Mo_4O_{13}$ was produced at $\Phi = 0.25$, $\Phi = 0.5$ produced monoclinic MoO_2, $\Phi = 0.75$ showed poorly crystalline MoO_2 whilst Φ values of 1 and 1.25 produced amorphous structures $\Phi = 0.25$ lead to larger and irregular-shaped particles of $(NH_4)_2Mo_4O_{13}$, $\Phi = 0.5$ produced MoO_2 with foam-like morphology consisting of 20–30 nm particles, with large surface area of 122.68 m^2 g^{-1} and mesopores of 3.5 to 5.5 nm range. The bandgap of as-synthesized MoO_2 was calculated as 2 eV $\Phi = 0.75$ produced foam-like structure consisting of more fine particles embedded in amorphous sheets Increasing Φ value to 1 lead to the formation of only foam-like amorphous phase with no significant particles Whilst $\Phi = 1.25$ lead to the formation of only foam-like amorphous phase with no significant particles The as-synthesized MoO_2 showed excellent visible light activity towards several typical organic pollutants (MB, MO, RhB) from water	178
Ultra-porous α-MoO_3	The synthesis was carried out using two different molybdenum precursors. (i) Molybdenum metal powder; (ii) AHM. The sucrose was employed as fuel with a Φ value of 1 : 1 for both routes. The synthesis was carried out at 470 °C in air	UV light (120 W high-pressure mercury lamp). 250 mL of a 75 mg L^{-1} MB solution and 100 mg of product dosage was used for photocatalytic tests	The samples synthesized by both routes showed highly crystalline α-MoO_3. The PXRD showed peak broadening in sample prepared by molybdenum metal powder indicates smaller crystallite size The sample prepared by molybdenum metal powder consist of macropores with fine particles of average size 6 nm Whereas the sample AHM was quite agglomerated with average particle size of 50–100 nm The sample prepared by molybdenum metal powder outperformed the sample AHM towards photocatalytic degradation of MB owing to its smaller size distribution	381

Table 2 *(Contd.)*

Material	Synthesis conditions	Photocatalytic conditions (light source and pollutant)	Remarks	Ref.
TiO_2	$TiO(NO_3)_2$; the sample was prepared employing three different fuels (i) glycine (ii) HMT (iii) ODH. The Φ value was adjusted to 1 : 1 in all experiments	UV light and solar light conditions. 100 ppm MB with 1 kg m^{-3} (100 mg per 100 mL) catalyst loading	All the samples crystallized into TiO_2 anatase phase The crystallite size, particle size, surface area and bandgap of TiO_2 prepared by glycine fuel were reported as = 6 nm, 6–8 nm, 246 m^2 g^{-1}, and 2.85 eV, respectively The crystallite size, particle size, surface area and bandgap of TiO_2 prepared by HMT fuel were reported as 9 nm, 7–9, 164 m^2 g^{-1}, and 2.98 eV, respectively The crystallite size, particle size, surface area and bandgap of TiO_2 prepared by HMT fuel were reported as 7 nm. 11–13 nm, 143 m^2 g^{-1} and 2.85 eV, respectively The authors also reported the crystallite size, particle size and surface area of Degussa P25 to be 32 nm, 100–150 nm and 50 m^2 g^{-1}, respectively All the SCS-synthesized TiO_2 photocatalysts showed higher activity towards MB degradation than Degussa P25 The TiO_2 synthesized by glycine fuel showed higher photocatalytic activity than TiO_2 synthesized by HMT and ODH fuels	230

and the utilization of eco-friendly carbohydrate fuels lead to a weak and safe reaction.

8. Relationship between SCS parameters and photocatalytic performance

The kinetics of the SCS process is complex and not completely understood, with the major challenges of agglomeration, the presence of carbonaceous impurities and difficult control over the morphology of the solid product. However, to obtain the optimum materials for a specific application, one can deal with the synthesis parameters of the SCS process. A good guideline to modulate the properties of the SCS-synthesized product is given in this comprehensive review. Our study demonstrates that the SCS technique is an excellent synthesis method to overcome major challenges in the development of advanced binary, ternary and complex solid materials. It is a promising technique for the synthesis of highly crystalline products with suitable phases, nanoparticle range, large surface area and highly modulated bandgap for photocatalytic applications. In addition, the SCS technique is a promising technique for producing porous materials with and without any template. By varying the synthesis conditions, the SCS technique may also be advantageous to produce mesoporous nanostructures for optimum photocatalytic applications. Fig. 44 displays a schematic representation of a one-pot combustion technique for the synthesis of binary, doped and complex metal oxides as well as heterostructures by fine adjustment of the synthesis parameters.

Fuel plays a key role in the SCS process alongside the final calcination temperature and other synthesis parameters. A major critical step of the SCS approach is the selection of the fuel and pH of the redox solution; both factors are strongly related to the metal (nitrate) precursor and particularly the characteristics of the produced nanostructured photocatalyst. The choice of a suitable fuel or combination of fuels can also be effective for synthesizing advanced catalysts.[164,371,372] Both fuel-lean and fuel-rich conditions are suitable for obtaining optimal photocatalytic activity.[204] In most studies fuel-rich conditions have been more suitable for achieving higher photocatalytic activity.[124,373–376] On the other hand, the mode of combustion (*i.e.* voluminous or smoldering) had an influence on desired phase formation,[228] whilst a post-combustion temperature between 300 and 600 °C is recommended for improved crystallinity of the product and burning the residual organics from the product.[187,204,377] However, in some cases the residual carbon may improve the photocatalytic activity.[332] The photocatalytic efficiency strongly depends upon surface area. Higher calcination temperature may result in particle growth, which lowers the surface area of the product, whilst lower calcination temperature may lead to the formation of amorphous products. Additionally, higher heating rates, particularly in fuel-rich conditions, facilitate rapid decomposition of the precursors, hence leading to the formation of small-sized crystals. The higher heating rate leads to growth of an increased number of precursor nuclei and shorter time available for those nuclei to merge with each other.[376,378] The excess fuel may leave some carbonaceous impurity content in the final product. Furthermore, the bandgap of the nanostructured photocatalyst can be modulated by tuning the amount and type of fuel in the energetic redox mixture.

The surface area of the fabricated products is also modulated by the release of the excess of gaseous content during SCS. Moreover, the products obtained from different fuels have different surface areas owing to different content of gas evolution[230] and exothermicity of the combustion reaction. Table 2 summarizes the effect of various SCS parameters on the structural properties of the product and its photocatalytic activity. The table highlights that the simple tuning of SCS process parameters such as fuel type, precursor, precursor composition, fuel concentration, and calcination temperature can boost the photocatalytic performance.

9. Conclusion and outlook

There are many synthesis approaches for fabricating nanostructured materials; however, the SCS technique stands out as an effective synthesis technique for the preparation of advanced binary as well as complex and hybrid oxides which are difficult to produce from other methods. Besides being a fast and energy-efficient synthesis route, SCS also provides additional morphological benefits. The nanostructures obtained from the SCS technique are suitable for a wide range of photocatalytic applications such as dye removal, removal of organic compounds (*i.e.*, wastewater treatment), water splitting, and CO_2 conversion among others. There is a plethora of literature for the synthesis of metal oxide photocatalysts. However, non-oxide compounds can also be produced through the SCS process. Most importantly, the SCS parameters play a crucial role in the phase composition and physical characteristics of the nanostructured materials and their photocatalytic applications. Detailed knowledge of the SCS parameters is required to determine the structural properties of the derived product.

Several advantages and drawbacks of SCS are given below.

Advantages:

1. SCS is a green synthesis approach that is highly energy efficient, and it does not require the utilization of toxic solvents since metal precursors (metal nitrates) are generally soluble in water.

2. Post-combustion temperature (or calcination) at mild conditions (between 300 and 600 °C) can enhance solid crystallinity and decrease the content of residual organic material.

3. Fuel-rich conditions facilitate the rapid decomposition of the metal precursors, hence leading to the formation of small-sized particles.

4. The ignition mode assisted by microwave and ultrasound energy enhances the sustainable character of the SCS approach as a consequence of the reduction of the thermal treatment period and hence the energy consumption.

Drawbacks:

1. It is difficult to control the production of nanoparticles owing to the local high temperature upon the combustion reaction.

2. The high-temperatures generated during synthesis also lead to problems with energy dissipation and suitable reaction vessels.

3. Post-combustion (or calcination) at high temperatures (above 600 °C) may result in particle growth, thereby decreasing the surface area and the performance of the photocatalyst.

4. Emissions of CO_x and NO_x during the combustion reaction of the fuel–oxidizer redox mixture can be minimised through carbon capture and NO_x abatement and even neutralized *via* the utilization of sustainable organic fuels.

A variety of experimental evidence clearly indicates that the employed fuel, fuel concentration (and fuel-to-oxidizer ratio), calcination time and temperature play paramount roles in the structure, morphology, purity and metastability of single and complex solid compounds. The selection of type of fuel and fuel to oxidizer ratio have been the main strategies in the SCS technique to incorporate oxygen vacancies within the crystallite structure of metal oxides. These two factors are the most critical parameters to induce surface modifications in pristine semiconductors; indeed, by varying the type of fuel and its concentration a variety of ternary or quaternary metal oxides, or a heterojunction can be produced in a one-pot synthesis. However, more studies are required for the better understanding of phase evolution and the mechanism of formation of various morphologies of SCS-produced powders.

SCS is a potential technique for the development of advanced materials for energy and environmental remediation applications. Appropriate surface modifications in pristine metal oxides may overcome the drawbacks for efficient utilization of solar energy. The modifications in pristine metal oxide semiconductors employed through the SCS technique are addition of heteroatoms, metal and non-metal doping, defect generation and oxygen vacancy generation, construction of heterojunctions (*i.e.* p–n heterojunctions and metal oxide–metal oxide heterojunction), production of carbon-based metal oxide composites and synthesis of complex metal oxides. Owing to the advanced photocatalytic performance, synthesis of porous materials has been in demand with the assistance of templates. Interestingly, the evolving gases during the combustion reaction in SCS sometime result in porous structures without the assistance of templates, hence decreasing the overall processing cost and time. The most promising aspects of SCS for the development of efficient photocatalysts are the relatively high porosity and the bandgap modulation of the semiconducting material to make it more visible light responsive.

Although the progress achieved in the SCS of advanced photocatalysts, and in general nanomaterials, has been remarkable, as described in this review, there are still some challenges particularly in the development of methodology to control the size and shapes of various geometries for nanomaterials, particularly in the advance of greener approaches. Control of the exothermicity of the combustion reaction and *in situ* advanced analytical techniques to monitor the combustion reaction under real operational time may be useful strategies to control and understand the influence of SCS metrics over the morphology, crystallinity, and nanoparticle size of the SCS-prepared nanomaterials. On the other hand, the development of greener methods of SCS focused on the utilization of

MWs, ultrasound, less hazardous chemicals, and eco-friendly microstructure-controlling agents (*i.e.*, fuels and soft/hard templates) from natural resources alongside the capture (and utilization) of CO_x and NO_x emissions are viable approaches to enhance the sustainability of the SCS technique.

We envisage that the SCS method will pave the way for developing advanced nanomaterials whilst meeting the standards of quality, greenness, circularity and social wellness for a sustainable future. Obviously, the utilization of a sustainable source of energy for initiating the combustion reaction alongside the utilization of eco-friendly raw materials will boost its implementation as a unique and efficient sustainable synthesis method.

Author contributions

F. S. and S. G.-C. conceptualized the idea and wrote the original draft. A. M., M. A. R., T. X. and X. Z. refined the draft. X.Z. did the financial support.

Conflicts of interest

There are no conflicts to declare.

Acknowledgements

The authors thank the University of Oxford for generous funding and continual support of this multidisciplinary research. We would like to acknowledge National Natural Science Foundation of China (Grant No. 12174462) for their financial support.

References

1 F. Siddique, A. Mirzaei, S. Gonzalez-Cortes, D. Slocombe, H. A. Al-Megren, T. Xiao, M. A. Rafiq and P. P. Edwards, Sustainable Chemical Processing of Flowing Wastewater through Microwave Energy, *Chemosphere*, 2022, **287**, 132035, DOI: **10.1016/j.chemosphere.2021.132035**.

2 G. Balakrishnan, R. Velavan, K. Mujasam Batoo and E. H. Raslan, Microstructure, Optical and Photocatalytic Properties of MgO Nanoparticles, *Results Phys.*, 2020, **16**, 103013, DOI: **10.1016/j.rinp.2020.103013**.

3 M. Piumetti, D. Fino and N. Russo, Mesoporous Manganese Oxides Prepared by Solution Combustion Synthesis as Catalysts for the Total Oxidation of VOCs, *Appl. Catal., B*, 2015, **163**, 277–287, DOI: **10.1016/j.apcatb.2014.08.012**.

4 H. Guo, Z. Zhang, Z. Jiang, M. Chen, H. Einaga and W. Shangguan, Catalytic Activity of Porous Manganese Oxides for Benzene Oxidation Improved via Citric Acid Solution Combustion Synthesis, *J. Environ. Sci.*, 2020, **98**, 196–204, DOI: **10.1016/j.jes.2020.06.008**.

5 R. Bakkiyaraj, G. Bharath, K. Hasini Ramsait, A. Abdel-Wahab, E. H. Alsharaeh, S. M. Chen and M. Balakrishnan, Solution Combustion Synthesis and Physico-Chemical Properties of Ultrafine CeO_2 Nanoparticles and Their Photocatalytic Activity, *RSC Adv.*, 2016, **6**(56), 51238–51245, DOI: **10.1039/c6ra00382f**.

6 W. Kang, D. O. Ozgur and A. Varma, Solution Combustion Synthesis of High Surface Area CeO_2 Nanopowders for Catalytic Applications: Reaction Mechanism and Properties, *ACS Appl. Nano Mater.*, 2018, **1**(2), 675–685, DOI: **10.1021/acsanm.7b00154**.

7 S. Patil and H. P. Dasari, Effect of Fuel and Solvent on Soot Oxidation Activity of Ceria Nanoparticles Synthesized by Solution Combustion Method, *Mater. Sci. Energy Technol.*, 2019, **2**(3), 485–489, DOI: **10.1016/j.mset.2019.05.005**.

8 D. Kovacheva, H. Gadjov, K. Petrov, S. Mandal, M. G. Lazarraga, L. Pascual, J. M. Amarilla, R. M. Rojas, P. Herrero and J. M. Rojo, Synthesizing Nanocrystalline LiMn2O4 by a Combustion Route, *J. Mater. Chem.*, 2002, **12**(4), 1184–1188, DOI: **10.1039/b107669h**.

9 F. T. Li, Y. Zhao, Y. Liu, Y. J. Hao, R. H. Liu and D. S. Zhao, Solution Combustion Synthesis and Visible Light-Induced Photocatalytic Activity of Mixed Amorphous and Crystalline MgAl2O4 Nanopowders, *Chem. Eng. J.*, 2011, **173**(3), 750–759, DOI: **10.1016/j.cej.2011.08.043**.

10 B. Xu, T. Xiao, Z. Yan, X. Sun, J. Sloan, S. L. González-Cortés, F. Alshahrani and M. L. H. Green, Synthesis of Mesoporous Alumina with Highly Thermal Stability Using Glucose Template in Aqueous System, *Microporous Mesoporous Mater.*, 2006, **91**(1–3), 293–295, DOI: **10.1016/j.micromeso.2005.12.007**.

11 S. L. González-Cortés, T. C. Xiao, Pedro M. F. J. Costa, B. Fontal and M. L. H. Green, Urea-Organic Matrix Method: An Alternative Approach to Prepare Co-MoS 2/γ-Al2O3 HDS Catalyst, *Appl. Catal., A*, 2004, **270**(1–2), 209–222, DOI: **10.1016/j.apcata.2004.05.006**.

12 A. A. Essawy, I. H. Alsohaimi, M. S. Alhumaimess, H. M. A. Hassan and M. M. Kamel, Green Synthesis of Spongy Nano-ZnO Productive of Hydroxyl Radicals for Unconventional Solar-Driven Photocatalytic Remediation of Antibiotic Enriched Wastewater, *J. Environ. Manage.*, 2020, **271**, 110961, DOI: **10.1016/j.jenvman.2020.110961**.

13 A. S. Mukasyan and P. Dinka, Novel Approaches to Solution-Combustion Synthesis of Nanomaterials, *Int. J. Self-Propag. High-Temp. Synth.*, 2007, **16**(1), 23–35, DOI: **10.3103/s1061386207010049**.

14 P. Erri, P. Pranda and A. Varma, Oxidizer - Fuel Interactions in Aqueous Combustion Synthesis. 1. Iron(III) Nitrate - Model Fuels, *Ind. Eng. Chem. Res.*, 2004, Iii, 3092–3096.

15 A. Varma and A. S. Mukasyan, Combustion Synthesis of Advanced Materials: Fundamentals and Applications, *Korean J. Chem. Eng.*, 2004, **21**(2), 527–536, DOI: **10.1007/BF02705444**.

16 S. T. Aruna and A. S. Mukasyan, Combustion Synthesis and Nanomaterials, *Curr. Opin. Solid State Mater. Sci.*, 2008, 44–50, DOI: **10.1016/j.cossms.2008.12.002**.

17 J. C. Toniolo, A. S. Takimi and C. P. Bergmann, Nanostructured Cobalt Oxides (Co3O4 and CoO) and Metallic Co Powders Synthesized by the Solution Combustion Method, *Mater. Res. Bull.*, 2010, **45**(6), 672–676, DOI: **10.1016/j.materresbull.2010.03.001**.

18 J. C. Toniolo, M. D. Lima, A. S. Takimi and C. P. Bergmann, Synthesis of Alumina Powders by the Glycine-Nitrate Combustion Process, *Mater. Res. Bull.*, 2005, **40**(3), 561–571, DOI: **10.1016/j.materresbull.2004.07.019**.

19 T. Gotoh, M. Jeem, L. Zhang, N. Okinaka and S. Watanabe, Synthesis of Yellow Persistent Phosphor Garnet by Mixed Fuel Solution Combustion Synthesis and Its Characteristic, *J. Phys. Chem. Solids*, 2020, **142**, 109436, DOI: **10.1016/j.jpcs.2020.109436**.

20 G. Liu, X. Kong, Q. Wang, H. Sun, B. Wang and Z. Yi, Low-Temperature Solution Combustion Synthesis of High Performance LiNi 0.5Mn1.5O4, *Ceram. Int.*, 2014, **40**(5), 6447–6452, DOI: **10.1016/j.ceramint.2013.11.095**.

21 F. T. Li, J. Ran, M. Jaroniec and S. Z. Qiao, Solution Combustion Synthesis of Metal Oxide Nanomaterials for Energy Storage and Conversion, *Nanoscale*, 2015, **7**(42), 17590–17610, DOI: **10.1039/c5nr05299h**.

22 E. Carlos, R. Martins, E. Fortunato and R. Branquinho, Solution Combustion Synthesis: Towards a Sustainable Approach for Metal Oxides, *Chem. – Eur. J.*, 2020, 9099–9125, DOI: **10.1002/chem.202000678**.

23 M. S. S. Danish, L. L. Estrella, I. M. A. Alemaida, A. Lisin, N. Moiseev, M. Ahmadi, M. Nazari, M. Wali, H. Zaheb and T. Senjyu, Photocatalytic Applications of Metal Oxides for Sustainable Environmental Remediation, *Metals*, 2021, **11**(1), 80, DOI: **10.3390/met11010080**.

24 F. Siddique, S. Gonzalez-Cortes, T. Xiao, M. A. Rafiq and P. P. Edwards, Effect of Surface Modification and H2reduction of WO3nanoparticles in Methylene Blue Photodegradation, *Surf. Topogr.: Metrol. Prop.*, 2020, **8**(4), 045012, DOI: **10.1088/2051-672X/abSSb7**.

25 A. L. Linsebigler, G. Lu and J. T. Yates, Photocatalysis on TiO2 Surfaces: Principles, Mechanisms, and Selected Results, *Chem. Rev.*, 1995, **95**(3), 735–758, DOI: **10.1021/cr00035a013**.

26 W. Hou and S. B. Cronin, A Review of Surface Plasmon Resonance-Enhanced Photocatalysis, *Adv. Funct. Mater.*, 2013, 1612–1619, DOI: **10.1002/adfm.201202148**.

27 L. Puma, G. Bono, A. Krishnaiah, D. Collin and J. G, Preparation of Titanium Dioxide Photocatalyst Loaded onto Activated Carbon Support Using Chemical Vapor Deposition: A Review Paper, *J. Hazard. Mater.*, 2008, 209–219, DOI: **10.1016/j.jhazmat.2008.01.040**.

28 Y. Nosaka and A. Y. Nosaka, Generation and Detection of Reactive Oxygen Species in Photocatalysis, *Chem. Rev.*, 2017, 11302–11336, DOI: **10.1021/acs.chemrev.7b00161**.

29 A. Fujishima, X. Zhang and D. A. Tryk, TiO2 Photocatalysis and Related Surface Phenomena, *Surf. Sci. Rep.*, 2008, 515–582, DOI: **10.1016/j.surfrep.2008.10.001**.

30 A. B. Djurišić, Y. H. Leung and A. M. Ching Ng, Strategies, for Improving the Efficiency of Semiconductor Metal Oxide Photocatalysis, *Mater. Horiz.*, 2014, 400–410, DOI: **10.1039/c4mh00031e**.

31 S. N. Frank and A. J. Bard, Heterogeneous Photocatalytic Oxidation of Cyanide Ion in Aqueous Solutions at TiO2 Powder, *J. Am. Chem. Soc.*, 1977, **99**(1), 303–304, DOI: **10.1021/ja00443a081**.

32 W. R. K. Thalgaspitiya, T. Kankanam Kapuge, D. Rathnayake, J. He, W. S. Willis and S. L. Suib, Generalized Synthesis of High Surface Area Mesoporous Metal Titanates as Efficient Heterogeneous Catalysts, *Appl. Mater. Today*, 2020, **19**, 100570–100575, DOI: **10.1016/j.apmt.2020.100570**.

33 X. Pu, D. Zhang, Y. Gao, X. Shao, G. Ding, S. Li and S. Zhao, One-Pot Microwave-Assisted Combustion Synthesis of Graphene Oxide-TiO 2 Hybrids for Photodegradation of Methyl Orange, *J. Alloys Compd.*, 2013, **551**, 382–388, DOI: **10.1016/j.jallcom.2012.11.028**.

34 F. Siddique, S. Gonzalez-Cortes, T. Xiao, M. A. Rafiq and P. P. Edwards, Effect of Surface Modification and H 2 Reduction of WO 3 Nanoparticles in Methylene Blue Photodegradation, *Surf. Topogr.: Metrol. Prop.*, 2020, **8**(4), 045012, DOI: **10.1088/2051-672x/abSSb7**.

35 A. E. Sychev and A. G. Merzhanov, Self-Propagating High-Temperature Synthesis of Nanomaterials, *Usp. Khim.*, 2004, **73**(2), 157–171, DOI: **10.1070/rc2004v073n02abeh000837**.

36 J. J. Kingsley and K. C. Patil, A Novel Combustion Process for the Synthesis of Fine Particle α-Alumina and Related Oxide Materials, *Mater. Lett.*, 1988, **6**(11–12), 427–432, DOI: **10.1016/0167-577X(88)90045-6**.

37 A. Varma, A. S. Mukasyan, A. S. Rogachev and K. V. Manukyan, Solution Combustion Synthesis of Nanoscale Materials, *Chem. Rev.*, 2016, 14493–14586, DOI: **10.1021/acs.chemrev.6b00279**.

38 K. Sada, B. Senthilkumar and P. Barpanda, Electrochemical Potassium-Ion Intercalation in Na: XCoO2: A Novel Cathode Material for Potassium-Ion Batteries, *Chem. Commun.*, 2017, **53**(61), 8588–8591, DOI: **10.1039/c7cc02791e**.

39 R. A. E. Acedera, G. Gupta, M. Mamlouk and M. D. L. Balela, Solution Combustion Synthesis of Porous Co3O4 Nanoparticles as Oxygen Evolution Reaction (OER) Electrocatalysts in Alkaline Medium, *J. Alloys Compd.*, 2020, **836**, 154919, DOI: **10.1016/j.jallcom.2020.154919**.

40 R. Li, F. Zhu, Liuxinglian, M. Xiao, Y. Meng and Y. Zhang, Solution Combustion Synthesis of Mesoporous Mesh-Structured Co 3 O 4/C Composites as Anode Materials for Lithium Storage, *Mater. Express*, 2020, **10**(6), 819–826, DOI: **10.1166/mex.2020.1706**.

41 A. A. Lopera, A. M. A. Velásquez, L. C. Clementino, S. Robledo, A. Montoya, L. M. de Freitas, V. D. N. Bezzon, C. R. Fontana, C. Garcia and M. A. S. Graminha, Solution-Combustion Synthesis of Doped TiO2 Compounds and Its Potential Antileishmanial Activity Mediated by Photodynamic Therapy, *J. Photochem. Photobiol., B*, 2018, **183**, 64–74, DOI: **10.1016/j.jphotobiol.2018.04.017**.

42 J. Yu, Y. Ni and M. Zhai, Highly Selective Non-Enzyme Glucose Detection Based on Co-CoO-Co3O4 Nanocomposites Prepared via a Solution-Combustion and Subsequent Heat-Treating Route, *J. Alloys Compd.*, 2017, **723**, 904–911, DOI: **10.1016/j.jallcom.2017.06.322**.

43 S. L. González-Cortés, S. Rugmini, T. Xiao, M. L. H. Green, S. M. Rodulfo-Baechler and F. E. Imbert, Deep Hydrotreating of Different Feedstocks over a Highly Active Al 2O3-Supported NiMoW Sulfide Catalyst, *Appl. Catal., A*, 2014, **475**, 270–281, DOI: **10.1016/j.apcata.2014.01.045**.

44 S. L. González-Cortés, T. C. Xiao, T. W. Lin and M. L. H. Green, Influence of Double Promotion on HDS Catalysts Prepared by Urea-Matrix Combustion Synthesis, *Appl. Catal., A*, 2006, **302**(2), 264–273, DOI: **10.1016/j.apcata.2006.01.019**.

45 M. Mohandoss, S. Sen Gupta, R. Kumar, M. R. Islam, A. Som, A. G. Mohd, T. Pradeep and S. M. Maliyekkal, Self-Propagated Combustion Synthesis of Few-Layered Graphene: An Optical Properties Perspective, *Nanoscale*, 2018, **10**(16), 7581–7588, DOI: **10.1039/c7nr09156g**.

46 R. Rosa, P. Veronesi and C. Leonelli, A Review on Combustion Synthesis Intensification by Means of Microwave Energy, *Chem. Eng. Process.*, 2013, **71**, 2–18, DOI: **10.1016/j.cep.2013.02.007**.

47 J. J. Moore and H. J. Feng, Combustion Synthesis of Advanced Materials: Part I, Reaction Parameters, *Prog. Mater. Sci.*, 1995, 243–273, DOI: **10.1016/0079-6425(94)00011-5**.

48 Z. Zhou, X. Liu, C. Li, Y. Yang, J. Xu and M. Xu, Flaming Combustion and Smoldering of Active Impregnated Cigarette Butts: A Novel Method for Synthesis of Nanostructured MnOx Catalysts for NOx Reduction, *Fuel*, 2020, **277**, 118230, DOI: **10.1016/j.fuel.2020.118230**.

49 M. Melchionna, A. Trovarelli and P. Fornasiero, *Synthesis and Properties of Cerium Oxide-Based Materials*, Elsevier Inc., 2020. DOI: **10.1016/b978-0-12-815661-2.00002-5**.

50 V. Kumari, N. Kumar, S. Yadav, A. Mittal and S. Sharma, Novel Mixed Metal Oxide (ZnO.La2O3.CeO$_2$) Synthesized via Hydrothermal and Solution Combustion Process - A Comparative Study and Their Photocatalytic Properties, *Mater. Today: Proc.*, 2019, **19**(xxxx), 650–657, DOI: **10.1016/j.matpr.2019.07.748**.

51 A. I. Stankiewicz and J. A. Moulijn, Process Intensification: Transforming Chemical Engineering, *Chem. Eng. Prog.*, 2000, **96**(1), 22–33.

52 R. Nagaraja, N. Kottam, C. R. Girija and B. M. Nagabhushana, Photocatalytic Degradation of Rhodamine B Dye under UV/Solar Light Using ZnO Nanopowder Synthesized by Solution Combustion Route, *Powder Technol.*, 2012, **215–216**, 91–97, DOI: **10.1016/j.powtec.2011.09.014**.

53 M. Niederberger and G. Garnweitner, Organic Reaction Pathways in the Nonaqueous Synthesis of Metal Oxide Nanoparticles, *Chem. – Eur. J.*, 2006, **12**(28), 7282–7302, DOI: **10.1002/chem.200600313**.

54 K. Rajeshwar and N. R. De Tacconi, Solution, Combustion Synthesis of Oxide Semiconductors for Solar Energy Conversion and Environmental Remediation, *Chem. Soc. Rev.*, 2009, **38**(7), 1984–1998, DOI: **10.1039/b811238j**.

55 K. C. Patil, M. S. Hegde, T. Rattan and S. T. Aruna, *Chemistry of Nanocrystalline Oxide Materials*, World Scientific, 2008. DOI: **10.1142/6754**.

56 I. Barin, O. Knacke and O. Kubaschewski, *Thermochemical Properties of Inorganic Substances*, Springer Berlin Heidelberg, 1977. DOI: **10.1007/978-3-662-02293-1**.

57 J. B. Holt and Z. A. Munir, Combustion Synthesis of Titanium Carbide: Theory and Experiment, *J. Mater. Sci.*, 1986, **21**(1), 251–259, DOI: **10.1007/BF01144729**.

58 H. C. Yi and J. J. Moore, Self-Propagating High-Temperature (Combustion) Synthesis (SHS) of Powder-Compacted Materials, *J. Mater. Sci.*, 1990, 1159–1168, DOI: **10.1007/BF00585421**.

59 A. S. Mukasyan, P. Epstein and P. Dinka, Solution Combustion Synthesis of Nanomaterials, *Proc. Combust. Inst.*, 2007, **31 II**(2), 1789–1795, DOI: **10.1016/j.proci.2006.07.052**.

60 D. E. Clark, I. Ahmad and R. C. Dalton, Microwave Ignition and Combustion Synthesis of Composites, *Mater. Sci. Eng., A*, 1991, **144**(1–2), 91–97, DOI: **10.1016/0921-5093(91)90213-7**.

61 T. S. Cam, T. A. Vishnevskaya, S. O. Omarov, V. N. Nevedomskiy and V. I. Popkov, Urea–Nitrate Combustion Synthesis of CuO/CeO$_2$ Nanocatalysts toward Low-Temperature Oxidation of CO: The Effect of Red/Ox Ratio, *J. Mater. Sci.*, 2020, **55**(26), 11891–11906, DOI: **10.1007/s10853-020-04857-3**.

62 S. Thiagarajan, A. Sanmugam and D. Vikraman, Facile Methodology of Sol-Gel Synthesis for Metal Oxide Nanostructures, in *Recent Applications in Sol-Gel Synthesis*, InTech, 2017. DOI: **10.5772/intechopen.68708**.

63 X. Yu, J. Smith, N. Zhou, L. Zeng, P. Guo, Y. Xia, A. Alvarez, S. Aghion, H. Lin, J. Yu, *et al.*, Spray-Combustion Synthesis: Efficient Solution Route to High-Performance Oxide Transistors, *Proc. Natl. Acad. Sci. U. S. A.*, 2015, **112**(11), 3217–3222, DOI: **10.1073/pnas.1501548112**.

64 R. Gedye, F. Smith, K. Westaway, H. Ali, L. Baldisera, L. Laberge and J. Rousell, The Use of Microwave Ovens for Rapid Organic Synthesis, *Tetrahedron Lett.*, 1986, **27**(3), 279–282, DOI: **10.1016/S0040-4039(00)83996-9**.

65 R. Rosa, L. Trombi, P. Veronesi and C. Leonelli, Microwave Energy Application to Combustion Synthesis: A Comprehensive Review of Recent Advancements and Most Promising Perspectives, *Int. J. Self-Propag. High-Temp. Synth.*, 2017, 221–233, DOI: **10.3103/S1061386217040057**.

66 R. C. Dalton, I. Ahmad and D. E. Clark, Combustion Synthesis Using Microwave Energy, in *Ceramic Engineering and Science Proceedings*, John Wiley & Sons, Inc., Hoboken, NJ, USA, 1990, vol. 11, pp. 1729–1742. DOI: **10.1002/9780470313053.ch46**.

67 A. Talati and M. Haghighi, Influence of Fuel Type and Heating Approach on One-Step Microwave Combustion Design of Zn-Spinel as Supreme Sunlight-Responsive

Nanophotocatalyst for Degradation of Orange II in Water, *Sol. Energy*, 2022, **234**, 275–293, DOI: 10.1016/j.solener.2022.02.003.

68 B. A. Roberts and C. R. Strauss, Toward Rapid, "Green", Predictable Microwave-Assisted Synthesis, *Acc. Chem. Res.*, 2005, 653–661, DOI: 10.1021/ar040278m.

69 V. Hiranmayee, K. Ananthasivan, D. Maji and K. Joseph, Microwave-Assisted Citrate Gel-Combustion Synthesis of Nanocrystalline Urania, *J. Nucl. Mater.*, 2019, **516**, 73–83, DOI: 10.1016/j.jnucmat.2018.12.031.

70 P. Veronesi, C. Leonelli, G. Poli and A. Casagrande, Enhanced Reactive NiAl Coatings by Microwave-Assisted SHS, *COMPEL - Int. J. Comput. Math. Electr. Electron. Eng.*, 2008, **27**(2), 491–499, DOI: 10.1108/03321640810847779.

71 P. Veronesi, R. Rosa, E. Colombini, C. Leonelli, G. Poli and A. Casagrande, Microwave Assisted Combustion Synthesis of Non-Equilibrium Intermetallic Compounds, *J. Microw. Power Electromagn. Energy*, 2010, **44**(1), 46–56, DOI: 10.1080/08327823.2010.11689769.

72 A. Mirzaei and G. Neri, Microwave-Assisted Synthesis of Metal Oxide Nanostructures for Gas Sensing Application: A Review, *Sens. Actuators, B*, 2016, 749–775, DOI: 10.1016/j.snb.2016.06.114.

73 C. O. Kappe, D. Dallinger and S. S. Murphree, *Practical Microwave Synthesis for Organic Chemists: Strategies, Instruments, and Protocols*, 2009. DOI: 10.1002/9783527623907.

74 D. Zhang, X. Pu, H. Li, Y. M. Yu, J. J. Shim, P. Cai, S. I. Kim and H. J. Seo, Microwave-Assisted Combustion Synthesis of Ag/ZnO Nanocomposites and Their Photocatalytic Activities under Ultraviolet and Visible-Light Irradiation, *Mater. Res. Bull.*, 2015, **61**, 321–325, DOI: 10.1016/j.materresbull.2014.10.048.

75 M. Shahmirzaee, M. Shafiee Afarani, A. Iran Nejhad and A. M. Arabi, Microwave-Assisted Combustion Synthesis of ZnAl2O4 and ZnO Nanostructure Particles for Photocatalytic Wastewater Treatment, *Part. Sci. Technol.*, 2019, **37**(1), 110–117, DOI: 10.1080/02726351.2017.1350772.

76 İ.H Karakaş, Z. Karcıoğlu Karakaş and M. Ertuğrul, Photocatalytic Activity of Cobalt Aluminate Nanoparticles Synthesized by Microwave-Assisted Combustion Method, *J. Phys. Chem. Solids*, 2022, **161**, 110482, DOI: 10.1016/j.jpcs.2021.110482.

77 H. Ajamein and M. Haghighi, On the Microwave Enhanced Combustion Synthesis of CuO-ZnO-Al2O3 Nanocatalyst Used in Methanol Steam Reforming for Fuel Cell Grade Hydrogen Production: Effect of Microwave Irradiation and Fuel Ratio, *Energy Convers. Manage.*, 2016, **118**, 231–242, DOI: 10.1016/j.enconman.2016.04.002.

78 M. Khodaeipour, M. Haghighi, M. Shabani and N. Mohseni, Influence of Fuel Type and Microwave Combustion on *In situ* Fabrication of BimOnBrz Mixed-Phase Nanostructured Photocatalyst: Effective Sun-Light Photo-Response Ability in Tetracycline Degradation, *J. Hazard. Mater.*, 2020, **393**, 122462, DOI: 10.1016/j.jhazmat.2020.122462.

79 M. Hashemzehi, V. Pirouzfar, H. Nayebzadeh and A. Alihosseini, Effect of Synthesizing Conditions on the Activity of Zinc-Copper Aluminate Nanocatalyst Prepared by Microwave Combustion Method Used in the Esterification Reaction, *Fuel*, 2020, **263**, 116422, DOI: 10.1016/j.fuel.2019.116422.

80 M. Rabbani, R. Rahimi and H. Farajnejad Ghadi, Photocatalytic, Application of BiFeO3 Synthesized via a Facile Microwave-Assisted Solution Combustion Method, *J. Sol-Gel Sci. Technol.*, 2018, **87**(2), 340–346, DOI: 10.1007/s10971-018-4743-6.

81 S. V. Sancheti and P. R. Gogate, A Review of Engineering Aspects of Intensification of Chemical Synthesis Using Ultrasound, *Ultrason. Sonochem.*, 2017, 527–543, DOI: 10.1016/j.ultsonch.2016.08.009.

82 J. H. Bang and K. S. Suslick, Applications of Ultrasound to the Synthesis of Nanostructured Materials, *Adv. Mater.*, 2010, 1039–1059, DOI: 10.1002/adma.200904093.

83 Q. Zhou, L. Xue, Y. Wang, H. Li, T. Chikada, Y. Oya and Y. Yan, Preparation of Li2TiO3 Ceramic with Nano-Sized Pores by Ultrasonic-Assisted Solution Combustion, *J. Eur. Ceram. Soc.*, 2017, **37**(11), 3595–3602, DOI: 10.1016/j.jeurceramsoc.2017.04.027.

84 Q. Chen, Q. Liu, X. Chu, Y. Zhang, Y. Yan, L. Xue and W. Zhang, Ultrasonic-Assisted Solution Combustion Synthesis of Porous Na3V2(PO4)3/C: Formation Mechanism and Sodium Storage Performance, *J. Nanopart. Res.*, 2017, **19**(4), DOI: 10.1007/s11051-017-3828-4.

85 S. Abedini Khorrami, G. Mahmoudzadeh, S. S. Madani and F. Gharib, Effect of Calcination Temperature on the Particle Sizes of Zinc Ferrite Prepared by a Combination of Sol-Gel Auto Combustion and Ultrasonic Irradiation Techniques, *J. Ceram. Process. Res.*, 2011, **12**(5), 504–508.

86 S. Hadke, M. T. Kalimila, S. Rathkanthiwar, S. Gour, R. Sonkusare and A. Ballal, Role of Fuel and Fuel-to-Oxidizer Ratio in Combustion Synthesis of Nano-Crystalline Nickel Oxide Powders, *Ceram. Int.*, 2015, **41**(10), 14949–14957, DOI: 10.1016/j.ceramint.2015.08.037.

87 G. C. S, S. Alkanad, K. Alnaggar, G. Al-Zaqri, N. Bajiri, M. A. B, T. Dhileepan, M. D. Neppolian, B. K and L. N, Surface Defect-Engineered CeO 2− x by Ultrasound Treatment for Superior Photocatalytic H 2 Production and Water Treatment, *Catal. Sci. Technol.*, 2022, **12**, 2071–2083, DOI: 10.1039/d1cy01940f.

88 B. Wang, S. Wang, L. Gong and Z. Zhou, Structural, Magnetic and Photocatalytic Properties of Sr 2-Doped BiFeO 3 Nanoparticles Based on an Ultrasonic Irradiation Assisted Self-Combustion Method, *Ceram. Int.*, 2012, **38**(8), 6643–6649, DOI: 10.1016/j.ceramint.2012.05.051.

89 L. Lamiri, B. Kahouadji, M. Berd, A. Abdellatif, L. Benchallal, L. Guerbous, S. Ouhenia, A. Souici, L. Amiour, A. Zoukel, *et al.*, Structural, Morphological and Photoluminescence Characterizations of Sm3 + Doped Y2O3 Nano-Sized Phosphors Synthesized by Ultrasound

Assisted Sol Gel Method, *J. Rare Earths*, 2022, DOI: 10.1016/j.jre.2022.03.006.

90 C. Coromelci, M. Neamtu, M. Ignat, P. Samoila, M. F. Zaltariov and M. Palamaru, Ultrasound Assisted Synthesis of Heterostructured TiO2/ZnFe2O4 and TiO2/ZnFe1.98La0.02O4 Systems as Tunable Photocatalysts for Efficient Organic Pollutants Removal, *Ceram. Int.*, 2022, **48**(4), 4829–4840, DOI: 10.1016/j.ceramint.2021.11.019.

91 J. Burgess, *No Title*, John Wiley & Sons, London, 1978.

92 D. Nicholls, *Complexes and First-Row Transition Elements*, 1974.

93 J. Livage, M. Henry and C. Sanchez, Sol-Gel Chemistry of Transition Metal Oxides, *Prog. Solid State Chem.*, 1988, **18**(4), 259–341, DOI: 10.1016/0079-6786(88)90005-2.

94 B. L. Cushing, V. L. Kolesnichenko and C. J. O'Connor, Recent Advances in the Liquid-Phase Syntheses of Inorganic Nanoparticles, *Chem. Rev.*, 2004, **104**(9), 3893–3946, DOI: 10.1021/cr030027b.

95 M. Henry, J. P. Jolivet and J. Livage, Aqueous Chemistry of Metal Cations: Hydrolysis, Condensation and Complexation, in *Chemistry, Spectroscopy and Applications of Sol-Gel Glasses*, Springer-Verlag, 2006, pp. 153–206. DOI: 10.1007/bfb0036968.

96 A. E. Danks, S. R. Hall and Z. Schnepp, The Evolution of "sol-Gel" Chemistry as a Technique for Materials Synthesis, *Mater. Horiz.*, 2016, **3**(2), 91–112, DOI: 10.1039/c5mh00260e.

97 S. L. González-Cortés and F. E. Imbert, Fundamentals, Properties and Applications of Solid Catalysts Prepared by Solution Combustion Synthesis (SCS), *Appl. Catal., A*, 2013, 117–131, DOI: 10.1016/j.apcata.2012.11.024.

98 J. A. Bergwerff, A. A. Lysova, L. Espinosa-Alonso, I. V. Koptyug and B. M. Weckhuysen, Monitoring Transport Phenomena of Paramagnetic Metal-Ion Complexes inside Catalyst Bodies with Magnetic Resonance Imaging, *Chem. – Eur. J.*, 2008, **14**(8), 2363–2374, DOI: 10.1002/chem.200700990.

99 R. A. Cox, Acids and Bases. Solvent Effects on Acid-Base Strength. By Brian G. Cox, *Angew. Chem., Int. Ed.*, 2013, **52**(30), 7638–7638, DOI: 10.1002/anie.201304650.

100 T. Fujikawa, Highly Active HDS Catalyst for Producing Ultra-Low Sulfur Diesel Fuels, *Top. Catal.*, 2009, **52**(6–7), 872–879, DOI: 10.1007/s11244-009-9228-y.

101 S. L. González-Cortés, Y. Qian, H. A. Almegren, T. Xiao, V. L. Kuznetsov and P. P. Edwards, Citric Acid-Assisted Synthesis of γ-Alumina-Supported High Loading CoMo Sulfide Catalysts for the Hydrodesulfurization (HDS) and Hydrodenitrogenation (HDN) Reactions, *Appl. Petrochem. Res.*, 2015, **5**(3), 181–197, DOI: 10.1007/s13203-015-0097-y.

102 F. Deganello, G. Marcì and G. Deganello, Citrate-Nitrate Auto-Combustion Synthesis of Perovskite-Type Nanopowders: A Systematic Approach, *J. Eur. Ceram. Soc.*, 2009, **29**(3), 439–450, DOI: 10.1016/j.jeurceramsoc.2008.06.012.

103 L. Junliang, Z. Wei, G. Cuijing and Z. Yanwei, Synthesis and Magnetic Properties of Quasi-Single Domain M-Type Barium Hexaferrite Powders via Sol-Gel Auto-Combustion: Effects of PH and the Ratio of Citric Acid to Metal Ions (CA/M), *J. Alloys Compd.*, 2009, **479**(1–2), 863–869, DOI: 10.1016/j.jallcom.2009.01.081.

104 J. L. Ortiz-Quiñonez, U. Pal and M. S. Villanueva, Structural, Magnetic, and Catalytic Evaluation of Spinel Co, Ni, and Co-Ni Ferrite Nanoparticles Fabricated by Low-Temperature Solution Combustion Process, *ACS Omega*, 2018, **3**(11), 14986–15001, DOI: 10.1021/acsomega.8b02229.

105 D. G. Tuck, Critical Survey of Stability Constants of Complexes of Indium, *Pure Appl. Chem.*, 1983, **55**(9), 1477–1528, DOI: 10.1351/pac198355091477.

106 O. V. Komova, S. A. Mukha, O. V. Netskina, G. V. Odegova, A. A. Pochtar, A. V. Ishchenko and V. I. Simagina, A Solid Glycine-Based Precursor for the Preparation of La2CuO4 by Combustion Method, *Ceram. Int.*, 2015, **41**(1), 1869–1878, DOI: 10.1016/j.ceramint.2014.09.139.

107 M. P. Pechini, *Method of preparing idead and alkaline earth titanates and niobates and coating method using the same*, 1963.

108 L. Dimesso, Pechini Processes: An Alternate Approach of the Sol–Gel Method, Preparation, Properties, and Applications, in *Handbook of Sol-Gel Science and Technology*, Springer International Publishing, 2016, pp. 1–22. DOI: 10.1007/978-3-319-19454-7_123-1.

109 H. Flaschka, Complexation in Analytical Chemistry (Ringbom, Anders), *J. Chem. Educ.*, 1964, **41**(6), A474, DOI: 10.1021/ed041pa474.1.

110 M. Kakihana, "Sol-Gel" Preparation of High Temperature Superconducting Oxides, *J. Sol-Gel Sci. Technol.*, 1996, **6**(1), 7–55, DOI: 10.1007/BF00402588.

111 J. Kragten, Atlas of Metal-Ligand Equilibria in Aqueous Solution. Ellis Horwood Ltd., Distributed by J. Wiley & Sons, New York-London-Sydney-Toronto 1978. 781 Seiten. Preis: £ 35.-, *Synth. React. Inorg. Met.-Org. Chem.*, 1978, **82**(10), 1117–1118, DOI: 10.1002/bbpc.19780821025.

112 R. Day, *Quantitative Analysis [by] R.A. Day, Jr. [and] A.L. Underwood*, Prentice Hall, Englewood Cliffs N.J., 2nd edn, 1967.

113 O. Van der Biest, J. Kwarciak, D. Dierickx, M. Dhalle, W. Boon and Y. Bruynseraede, Ceramic Superconductors Synthesized by Sol-Gel Methods, *Phys. C*, 1991, **190**(1–2), 119–121, DOI: 10.1016/S0921-4534(05)80220-5.

114 L. T. T. Nguyen, L. T. H. Nguyen, N. C. Manh, D. N. Quoc, H. N. Quang, H. T. T. Nguyen, D. C. Nguyen and L. G. Bach, A Facile Synthesis, Characterization, and Photocatalytic Activity of Magnesium Ferrite Nanoparticles via the Solution Combustion Method, *J. Chem.*, 2019, **2019**, 342868, DOI: 10.1155/2019/3428681.

115 Y. Gao, X. Pu, D. Zhang, G. Ding, X. Shao and J. Ma, Combustion Synthesis of Graphene Oxide-TiO 2 Hybrid Materials for Photodegradation of Methyl Orange, *Carbon*, 2012, **50**(11), 4093–4101, DOI: 10.1016/j.carbon.2012.04.057.

116 T. P. K. Murthy, B. S. Gowrishankar, M. N. Chandraprabha and R. H. Krishna, Solution Combustion Synthesis of Calcium Aluminate Nanocomposite Using Coffee Husk Extract as Green Fuel and Its Application in Adsorptive Amputation of Anionic Dyes, *Mater. Res. Express*, 2020, 7(3), 35503, DOI: **10.1088/2053-1591/ab6b65**.

117 L. Wang, Z. Li, J. Chen, Y. Huang, H. Zhang and H. Qiu, Enhanced Photocatalytic Degradation of Methyl Orange by Porous Graphene/ZnO Nanocomposite, *Environ. Pollut.*, 2019, **249**, 801–811, DOI: **10.1016/j.envpol.2019.03.071**.

118 A. K. Zak, M. E. Abrishami, W. H. A. Majid, R. Yousefi and S. M. Hosseini, Effects of Annealing Temperature on Some Structural and Optical Properties of ZnO Nanoparticles Prepared by a Modified Sol-Gel Combustion Method, *Ceram. Int.*, 2011, **37**(1), 393–398, DOI: **10.1016/j.ceramint.2010.08.017**.

119 E. Mercadelli, C. Galassi, A. L. Costa, S. Albonetti and A. Sanson, Sol-Gel Combustion Synthesis of BNBT Powders, *J. Sol-Gel Sci. Technol.*, 2008, **46**(1), 39–45, DOI: **10.1007/s10971-008-1693-4**.

120 A. D. Bachvarova-Nedelcheva, R. S. Iordanova, A. M. Stoyanova, R. D. Gegova, Y. B. Dimitriev and A. R. Loukanov, Photocatalytic Properties of ZnO/TiO2 Powders Obtained via Combustion Gel Method, *Cent. Eur. J. Chem.*, 2013, **11**(3), 364–370, DOI: **10.2478/s11532-012-0167-2**.

121 W. Morales, M. Cason, O. Aina, N. R. De Tacconi and K. Rajeshwar, Combustion Synthesis and Characterization of Nanocrystalline WO3, *J. Am. Chem. Soc.*, 2008, **130**(20), 6318–6319, DOI: **10.1021/ja8012402**.

122 P. Chen, M. Qin, Z. Chen, B. Jia, S. Zhao, Q. Wan and X. Qu, A Novel Approach to Synthesize the Amorphous Carbon-Coated WO3 with Defects and Excellent Photocatalytic Properties, *Mater. Des.*, 2016, **106**, 22–29, DOI: **10.1016/j.matdes.2016.05.090**.

123 M. Kusuma and K. V. Jagannath, Solution Combustion Synthesis of SrMoO4 Nanophosphor Using Different Molybdenum Sources and Study of Its Photocatalytic Properties, *Mater. Res. Express*, 2019, **6**(10), 1050a1, DOI: **10.1088/2053-1591/ab39ec**.

124 K. Bolaghi, Z. Hasheminiasari, M. Masoudpanah and S. M, Solution Combustion Synthesis of ZnO Powders Using Mixture of Fuels in Closed System, *Ceram. Int.*, 2018, **44**(11), 12684–12690, DOI: **10.1016/j.ceramint.2018.04.069**.

125 P. Kaur, S. K. Chawla, S. S. Meena, S. M. Yusuf and S. B. Narang, Synthesis of Co-Zr Doped Nanocrystalline Strontium Hexaferrites by Sol-Gel Auto-Combustion Route Using Sucrose as Fuel and Study of Their Structural, Magnetic and Electrical Properties, *Ceram. Int.*, 2016, **42**(13), 14475–14489, DOI: **10.1016/j.ceramint.2016.06.053**.

126 O. Burgos-Montes, R. Moreno, M. T. Colomer and J. C. Fariñas, Influence of Combustion Aids on Suspension Combustion Synthesis of Mullite Powders, *J. Eur. Ceram. Soc.*, 2006, **26**(15), 3365–3372, DOI: **10.1016/j.jeurceramsoc.2005.08.006**.

127 L. E. Muresan, A. I. Cadis, I. Perhaita, O. Ponta and D. T. Silipas, Thermal Behavior of Precursors for Synthesis of Y2SiO5:Ce Phosphor via Gel Combustion, *J. Therm. Anal. Calorim.*, 2015, **119**(3), 1565–1576, DOI: **10.1007/s10973-014-4315-0**.

128 S. R. Nair, R. D. Purohit, P. K. Sinha and A. K. Tyagi, Sr-Doped LaCoO3 through Acetate-Nitrate Combustion: Effect of Extra Oxidant NH4NO3, *J. Alloys Compd.*, 2009, **477**(1–2), 644–647, DOI: **10.1016/j.jallcom.2008.10.087**.

129 B. Pourgolmohammad, S. M. Masoudpanah and M. R. Aboutalebi, Synthesis of CoFe2O4 Powders with High Surface Area by Solution Combustion Method: Effect of Fuel Content and Cobalt Precursor, *Ceram. Int.*, 2017, **43**(4), 3797–3803, DOI: **10.1016/j.ceramint.2016.12.027**.

130 M. Amala Sekar, G. Dhanaraj, H. L. Bhat and K. C. Patil, Synthesis of Fine-Particle Titanates by the Pyrolysis of Oxalate Precursors, *J. Mater. Sci.: Mater. Electron.*, 1992, **3**(4), 237–239, DOI: **10.1007/BF00703033**.

131 K. Deshpande, A. Mukasyan and A. Varma, Direct Synthesis of Iron Oxide Nanopowders by the Combustion Approach: Reaction Mechanism and Properties, *Chem. Mater.*, 2004, **16**(24), 4896–4904, DOI: **10.1021/cm040061m**.

132 G. Manjunath, R. V. Vardhan, A. Salian, R. Jagannatha, M. Kedia and S. Mandal, Effect of Annealing-Temperature-Assisted Phase Evolution on Conductivity of Solution Combustion Processed Calcium Vanadium Oxide Films, *Bull. Mater. Sci.*, 2018, **41**(5), 126, DOI: **10.1007/s12034-018-1644-9**.

133 L. Ortega-San-Martín, K. Vidal, B. Roldán-Pozo, Y. Coello, A. Larrañaga and M. I. Arriortua, Synthesis Method Dependence of the Lattice Effects in Ln0.5M0.5FeO3 Perovskites (Ln=La and (Nd or Gd);M=Ba and (Ca or Sr)), *Mater. Res. Express*, 2016, 3(5), 056302, DOI: **10.1088/2053-1591/3/5/056302**.

134 M. G. Chourashiya and A. Urakawa, Solution Combustion Synthesis of Highly Dispersible and Dispersed Iridium Oxide as an Anode Catalyst in PEM Water Electrolysis, *J. Mater. Chem. A*, 2017, **5**(10), 4774–4778, DOI: **10.1039/c6ta11047a**.

135 S. Colussi, A. Gayen, M. Boaro, J. Llorca and A. Trovarelli, Influence of Different Palladium Precursors on the Properties of Solution-Combustion-Synthesized Palladium/Ceria Catalysts for Methane Combustion, *ChemCatChem*, 2015, **7**(14), 2222–2229, DOI: **10.1002/cctc.201500390**.

136 P. Chen, M. Qin, Z. Chen, B. Jia and X. Qu, Solution Combustion Synthesis of Nanosized WO: X: Characterization, Mechanism and Excellent Photocatalytic Properties, *RSC Adv.*, 2016, **6**(86), 83101–83109, DOI: **10.1039/c6ra12375a**.

137 A. Thomas, C. Janáky, G. F. Samu, M. N. Huda, P. Sarker, J. P. Liu, V. Van Nguyen, E. H. Wang, K. A. Schug and K. Rajeshwar, Time- and Energy-Efficient Solution Combustion Synthesis of Binary Metal Tungstate Nanoparticles with Enhanced Photocatalytic Activity,

ChemSusChem, 2015, **8**(10), 1652–1663, DOI: 10.1002/cssc.201500383.

138 T. B. Tang and V. K. Mohan, Thermal Decomposition of Solids, *Nature*, 1983, **303**(5919), 729, DOI: 10.1038/303729a0.

139 J. G. Jackson, R. W. Fonseca and J. A. Holcombe, Mass Spectral Studies of Thermal Decomposition of Metal Nitrates, *Spectrochim. Acta, Part B*, 1995, **50**(12), 1449–1457, DOI: 10.1016/0584-8547(95)01405-5.

140 C. C. Addison and N. Logan, Anhydrous Metal Nitrates, *Adv. Inorg. Chem. Radiochem.*, 1964, **6**(C), 71–142, DOI: 10.1016/S0065-2792(08)60225-3.

141 A. Małecki, R. Gajerski, S. Łabuś, B. Prochowska-Klisch and K. T. Wojciechowski, Mechanism of Thermal Decomposition of D-Metals Nitrates Hydrates, *J. Therm. Anal. Calorim.*, 2000, **60**(1), 17–23, DOI: 10.1023/A:1010155931266.

142 A. Małecki and B. Małecka, Formation of N2O during Thermal Decomposition of D-Metal Hydrates Nitrates, *Thermochim. Acta*, 2006, **446**(1–2), 113–116, DOI: 10.1016/j.tca.2006.02.006.

143 A. Malecki, B. Malecka, R. Gajerski and S. Labuś, Thermal Decomposition of Chromium(III) Nitrate(V) Nanohydrate. Different Chromium Oxides CrO1.5 + y Formation, *J. Therm. Anal. Calorim.*, 2003, **72**(1), 135–144, DOI: 10.1023/A:1023915618876.

144 E. A. Cochran, K. N. Woods, D. W. Johnson, C. J. Page and S. W. Boettcher, Unique Chemistries of Metal-Nitrate Precursors to Form Metal-Oxide Thin Films from Solution: Materials for Electronic and Energy Applications, *J. Mater. Chem. A*, 2019, **7**(42), 24124–24149, DOI: 10.1039/c9ta07727h.

145 A. E. Gobichon, J. P. Auffrédic and D. Louër, Thermal Decomposition of Neutral and Basic Lanthanum Nitrates Studied with Temperature-Dependent Powder Diffraction and Thermogravimetric Analysis, *Solid State Ionics*, 1996, **93**(1–2), 51–64, DOI: 10.1016/s0167-2738(96)00498-5.

146 J. R. A. Sietsma, J. D. Meeldijk, J. P. Den Breejen, M. Versluijs-Helder, A. J. Van Dillen, P. E. De Jongh and K. P. De Jong, The Preparation of Supported NiO and Co3O4 Nanoparticles by the Nitric Oxide Controlled Thermal Decomposition of Nitrates, *Angew. Chem., Int. Ed.*, 2007, **46**(24), 4547–4549, DOI: 10.1002/anie.200700608.

147 B. Małecka, A. Łącz, E. Drozdz and A. Małecki, Thermal Decomposition of D-Metal Nitrates Supported on Alumina, *J. Therm. Anal. Calorim.*, 2015, **119**(2), 1053–1061, DOI: 10.1007/s10973-014-4262-9.

148 P. L. Llewellyn, V. Chevrot, J. Ragaï, O. Cerclier, J. Estienne and F. Rouquérol, Preparation of Reactive Nickel Oxide by the Controlled Thermolysis of Hexahydrated Nickel Nitrate, *Solid State Ionics*, 1997, **101–103**(PART 1), 1293–1298, DOI: 10.1016/s0167-2738(97)00237-3.

149 J. Estellé, P. Salagre, Y. Cesteros, M. Serra, F. Medina and J. E. Sueiras, Comparative Study of the Morphology and Surface Properties of Nickel Oxide Prepared from Different Precursors, *Solid State Ionics*, 2003, **156**(1–2), 233–243, DOI: 10.1016/S0167-2738(02)00612-4.

150 S. Yuvaraj, F. Y. Lin, T. H. Chang and C. T. Yeh, Thermal Decomposition of Metal Nitrates in Air and Hydrogen Environments, *J. Phys. Chem. B*, 2003, **107**(4), 1044–1047, DOI: 10.1021/jp026961c.

151 J. J. Kingsley and L. R. Pederson, Combustion Synthesis of Perovskite LnCrO3 Powders Using Ammonium Dichromate, *Mater. Lett.*, 1993, **18**(1–2), 89–96, DOI: 10.1016/0167-577X(93)90063-4.

152 S. M. Khaliullin, V. D. Zhuravlev and V. G. Bamburov, Solution-Combustion Synthesis of Oxide Nanoparticles from Nitrate Solutions Containing Glycine and Urea: Thermodynamic Aspects, *Int. J. Self-Propag. High-Temp. Synth.*, 2016, **25**(3), 139–148, DOI: 10.3103/S1061386216030031.

153 K. Frikha, L. Limousy, J. Bouaziz, S. Bennici, K. Chaari and M. Jeguirim, Elaboration of Alumina-Based Materials by Solution Combustion Synthesis: A Review, *C. R. Chim.*, 2019, 206–219, DOI: 10.1016/j.crci.2018.10.004.

154 H. L. Haile, T. Abi and K. Tesfahun, Synthesis, Characterization and Photocatalytic Activity of MnO_2/Al2O3/Fe2O3 Nanocomposite for Degradation of Malachite Green, *Afr. J. Pure Appl. Chem.*, 2015, **9**(11), 211–222, DOI: 10.5897/ajpac2015.0656.

155 C. Zhu, A. Nobuta, I. Nakatsugawa and T. Akiyama, Solution Combustion Synthesis of LaMO3 (M = Fe, Co, Mn) Perovskite Nanoparticles and the Measurement of Their Electrocatalytic Properties for Air Cathode, *Int. J. Hydrogen Energy*, 2013, **38**(30), 13238–13248, DOI: 10.1016/j.ijhydene.2013.07.113.

156 A. Kumar, E. E. Wolf and A. S. Mukasyan, Solution Combustion Synthesis of Metal Nanopowders: Copper and Copper/Nickel Alloys, *AIChE J.*, 2011, **57**(12), 3473–3479, DOI: 10.1002/aic.12537.

157 A. Kumar, E. E. Wolf and A. S. Mukasyan, Solution Combustion Synthesis of Metal Nanopowders: Nickel-Reaction Pathways, *AIChE J.*, 2011, **57**(8), 2207–2214, DOI: 10.1002/aic.12416.

158 B. Yao, T. Xiao, O. A. Makgae, X. Jie, S. Gonzalez-Cortes, S. Guan, A. I. Kirkland, J. R. Dilworth, H. A. Al-Megren, S. M. Alshihri, *et al.*, Transforming Carbon Dioxide into Jet Fuel Using an Organic Combustion-Synthesized Fe-Mn-K Catalyst, *Nat. Commun.*, 2020, **11**(1), 1–12, DOI: 10.1038/s41467-020-20214-z.

159 S. A. Heidari-Asil, S. Zinatloo-Ajabshir, H. A. Alshamsi, A. Al-Nayili, Q. A. Yousif and M. Salavati-Niasari, Magnetically Recyclable ZnCo2O4/Co3O4 Nano-Photocatalyst: Green Combustion Preparation, Characterization and Its Application for Enhanced Degradation of Contaminated Water under Sunlight, *Int. J. Hydrogen Energy*, 2022, **47**(38), 16852–16861, DOI: 10.1016/j.ijhydene.2022.03.157.

160 A. Bianco Prevot, D. Fabbri, E. Bernardini, F. Deganello, M. L. Tummino and G. Magnacca, Insights on the Photocatalytic Performances of LaFeO3 Synthesized by

Solution Combustion Synthesis, in *Materials Science in Photocatalysis*, Elsevier, 2021, pp. 357–370. DOI: **10.1016/B978-0-12-821859-4.00023-4**.

161 B. M. Abu-Zied, Controlled Synthesis of Praseodymium Oxide Nanoparticles Obtained by Combustion Route: Effect of Calcination Temperature and Fuel to Oxidizer Ratio, *Appl. Surf. Sci.*, 2019, **471**(October 2018), 246–255, DOI: **10.1016/j.apsusc.2018.12.007**.

162 R. Hammami and H. Batis, Combustion Synthesized Crystalline La-Mn Perovskite Catalysts: Role of Fuel Molecule on Thermal and Chemical Events, *Arabian J. Chem.*, 2020, **13**(1), 683–693, DOI: **10.1016/j.arabjc.2017.07.009**.

163 E. Yilmaz and M. S. Sonmez, The Influence of Process Parameters on the Chemical and Structural Properties of Solution Combustion Prepared Vanadium Pentoxide, *Mater. Lett.*, 2020, **261**, 127095, DOI: **10.1016/j.matlet.2019.127095**.

164 N. Asefi, S. M. Masoudpanah and M. Hasheminiasari, Photocatalytic Performances of BiFeO 3 Powders Synthesized by Solution Combustion Method: The Role of Mixed Fuels, *Mater. Chem. Phys.*, 2019, **228**(October 2018), 168–174, DOI: **10.1016/j.matchemphys.2019.02.059**.

165 T. Lazarova, M. Georgieva, D. Tzankov, D. Voykova, L. Aleksandrov, Z. Cherkezova-Zheleva and D. Kovacheva, Influence of the Type of Fuel Used for the Solution Combustion Synthesis on the Structure, Morphology and Magnetic Properties of Nanosized NiFe2O4, *J. Alloys Compd.*, 2017, **700**, 272–283, DOI: **10.1016/j.jallcom.2017.01.055**.

166 M. A. Matin, M. A. H. Saleh Saad, A. Kumar, M. J. Al-Marri and S. A. Mansour, Effect of Fuel Content on the Electrocatalytic Methanol Oxidation Performance of Pt/ZnO Nanoparticles Synthesized by Solution Combustion, *Appl. Surf. Sci.*, 2019, **492**, 73–81, DOI: **10.1016/j.apsusc.2019.06.213**.

167 S. R. Jain, K. C. Adiga and V. R. Pai Verneker, Thermochemistry and, Lower Combustion Limit of Ammonium Perchlorate in Presence of Methylammonium Perchlorates, *Combust. Flame*, 1981, **40**(C), 113–120, DOI: **10.1016/0010-2180(81)90117-6**.

168 K. C. Patil, Advanced Ceramics: Combustion Synthesis and Properties, *Bull. Mater. Sci.*, 1993, **16**(6), 533–541, DOI: **10.1007/BF02757654**.

169 K. Suresh and K. C. Patil, A Recipe for an Instant Synthesis of Fine Particle Oxide Materials, *Perspect. Solid State Chem.*, 1995, 376–388.

170 F. Deganello and A. K. Tyagi, Solution Combustion Synthesis, Energy and Environment: Best Parameters for Better Materials, *Prog. Cryst. Growth Charact. Mater.*, 2018, 23–61, DOI: **10.1016/j.pcrysgrow.2018.03.001**.

171 Q. Zhou, Y. Mou, X. Ma, L. Xue and Y. Yan, Effect of Fuel-to-Oxidizer Ratios on Combustion Mode and Microstructure of Li2TiO3 Nanoscale Powders, *J. Eur. Ceram. Soc.*, 2014, **34**(3), 801–807, DOI: **10.1016/j.jeurceramsoc.2013.10.004**.

172 S. R. Jain, K. C. Adiga and V. R. Pai Verneker, A New Approach to Thermochemical Calculations of Condensed Fuel-Oxidizer Mixtures, *Combust. Flame*, 1981, **40**(C), 71–79, DOI: **10.1016/0010-2180(81)90111-5**.

173 Z. Cao, M. Qin, B. Jia, Y. Gu, P. Chen, A. A. Volinsky and X. Qu, One Pot Solution Combustion Synthesis of Highly Mesoporous Hematite for Photocatalysis, *Ceram. Int.*, 2015, **41**(2), 2806–2812, DOI: **10.1016/j.ceramint.2014.10.100**.

174 E. Carlos, R. Martins, E. Fortunato and R. Branquinho, Solution Combustion Synthesis: Towards a Sustainable Approach for Metal Oxides, *Chem. – Eur. J.*, 2020, 9099–9125, DOI: **10.1002/chem.202000678**.

175 B. M. Tripathi, T. Mohanty, D. Prakash, A. K. Tyagi and P. K. Sinha, Glycine-Nitrate Solution Combustion Synthesis of Lithium Zirconate: Effect of Fuel-to Oxidant Ratio on Phase, Microstructure and Sintering, *J. Eur. Ceram. Soc.*, 2020, **40**(1), 136–144, DOI: **10.1016/j.jeurceramsoc.2019.09.008**.

176 B. N. Sherikar, B. Sahoo and A. M. Umarji, Effect of Fuel and Fuel to Oxidizer Ratio in Solution Combustion Synthesis of Nanoceramic Powders: MgO, CaO and ZnO, *Solid State Sci.*, 2020, **109**, 106426, DOI: **10.1016/j.solidstatesciences.2020.106426**.

177 G. K. Nagendra, B. W. Shivaraj, C. Manjunatha, S. A. Ayeesha Siddiqua and V. Suchithra, Study of Structural Features and Antibacterial Property of ZnO/CuO Nanocomposites Derived from Solution Combustion Synthesis, in *IOP Conference Series: Materials Science and Engineering*, 2019, vol. 577. DOI: **10.1088/1757-899X/577/1/012111**.

178 S. Gu, M. Qin, H. Zhang, J. Ma, H. Wu and X. Qu, Facile Solution Combustion Synthesis of MoO2 Nanoparticles as Efficient Photocatalysts, *CrystEngComm*, 2017, **19**(43), 6516–6526, DOI: **10.1039/c7ce01611e**.

179 P. Yu, X. Zhang, Y. Chen and Y. Ma, Solution-Combustion Synthesis of ε-MnO_2 for Supercapacitors, *Mater. Lett.*, 2010, **64**(1), 61–64, DOI: **10.1016/j.matlet.2009.10.007**.

180 Y. Wang, S. Li and Z. Jiang, Combustion Synthesis of Porous Bismuth Oxide, *J. Phys.: Conf. Ser.*, 2021, **1732**(1), 012144, DOI: **10.1088/1742-6596/1732/1/012144**.

181 Z. Shang, Y. Yu, H. Yang, Z. Yang, Y. Xiao and X. Wang, One-Step Solution Combustion Synthesis of Micro/Nano-Scale Porous Cu/CeO_2 with Enhanced Photocatalytic Properties, *J. Rare Earths*, 2022, DOI: **10.1016/j.jre.2022.02.013**.

182 Y. Zhang, M. Wu, Y. Wang, X. Zhao and D. Y. C. Leung, Low-Cost and Efficient Mn/CeO_2 Catalyst for Photocatalytic VOCs Degradation via Scalable Colloidal Solution Combustion Synthesis Method, *J. Mater. Sci. Technol.*, 2022, **116**, 169–179, DOI: **10.1016/j.jmst.2021.11.041**.

183 D. N. V. V. Konda Lutukurthi, S. Dutta and D. K. Behara, Dual Role of Activated Carbon as Fuel and Template for Solution Combustion Synthesis of Porous Zinc Oxide Powders, *J. Am. Ceram. Soc.*, 2021, **104**(9), 4624–4636, DOI: **10.1111/jace.17841**.

184 H. V. Vasei, S. M. Masoudpanah, M. Adeli and M. R. Aboutalebi, Solution Combustion Synthesis of ZnO Powders Using CTAB as Fuel, *Ceram. Int.*, 2018, **44**(7), 7741–7745, DOI: **10.1016/j.ceramint.2018.01.202**.

185 D. Zhang, H. Liu, C. Su, H. Li and Y. Geng, Combustion Synthesis of Highly Efficient Bi/BiOBr Visible Light Photocatalyst with Synergetic Effects of Oxygen Vacancies and Surface Plasma Resonance, *Sep. Purif. Technol.*, 2019, **218**, 1–7, DOI: **10.1016/j.seppur.2019.02.037**.

186 Z. Ghahramani, A. M. Arabi, M. Shafiee Afarani and M. Mahdavian, Solution Combustion Synthesis of Cerium Oxide Nanoparticles as Corrosion Inhibitor, *Int. J. Appl. Ceram. Technol.*, 2020, **17**(3), 1514–1521, DOI: **10.1111/ijac.13365**.

187 M. Kusuma and G. T. Chandrappa, Effect of Calcination Temperature on Characteristic Properties of CaMoO 4 Nanoparticles, *J. Sci.: Adv. Mater. Devices*, 2019, **4**(1), 150–157, DOI: **10.1016/j.jsamd.2019.02.003**.

188 M. K. Hossain, G. F. Samu, K. Gandha, S. Santhanagopalan, J. P. Liu, C. Janáky and K. Rajeshwar, Solution Combustion Synthesis, Characterization, and Photocatalytic Activity of CuBi2O4 and Its Nanocomposites with CuO and α-Bi2O3, *J. Phys. Chem. C*, 2017, **121**(15), 8252–8261, DOI: **10.1021/acs.jpcc.6b13093**.

189 Y. Cao, B. Liu, R. Huang, Z. Xia and S. Ge, Flash Synthesis of Flower-like ZnO Nanostructures by Microwave-Induced Combustion Process, *Mater. Lett.*, 2011, **65**(2), 160–163, DOI: **10.1016/j.matlet.2010.09.072**.

190 V. S. Prabhudesai, A. A. Meshram, R. Vinu and S. M. Sontakke, Superior Photocatalytic Removal of Metamitron and Its Mixture with Rhodamine B Dye Using Combustion Synthesized TiO2 Nanomaterial, *Chem. Eng. J. Adv.*, 2020, **5**, 100084, DOI: **10.1016/j.ceja.2020.100084**.

191 K. N. S. Kumara, H. P. Nagaswarupa, K. R. V. Mahesh, S. C. Prashantha, M. Mylarappa and D. M. K. Siddeshwara, Synthesis and Characterization of Nano ZnO and MgO Powder by Low Temperature Solution Combustion Method: Studies Concerning Electrochemical and Photocatalytic Behavior, *Nanosyst.: Phys., Chem., Math.*, 2016, 662–666, DOI: **10.17586/2220-8054-2016-7-4-662-666**.

192 Y. Astuti, P. P. Elesta, D. S. Widodo, H. Widiyandari and R. Balgis, Hydrazine and Urea Fueled-Solution Combustion Method for Bi2o3 Synthesis: Characterization of Physicochemical Properties and Photocatalytic Activity, *Bull. Chem. React. Eng. Catal.*, 2020, **15**(1), 104–111, DOI: **10.9767/SSrec.15.1.5483.104-111**.

193 K. Belfaa, M. S. Lassoued, S. Ammar and A. Gadri, Synthesis and Characterization of V-Doped TiO2 Nanoparticles through Polyol Method with Enhanced Photocatalytic Activities, *J. Mater. Sci.: Mater. Electron.*, 2018, **29**(12), 10269–10276, DOI: **10.1007/s10854-018-9080-6**.

194 F. Granados-Correa and J. Bonifacio-Martínez, Combustion Synthesis Process for the Rapid Preparation of High-Purity SrO Powders, *Mater. Sci.-Pol.*, 2014, **32**(4), 682–687, DOI: **10.2478/s13536-014-0250-9**.

195 P. Chen, M. Qin, D. Zhang, Z. Chen, B. Jia, Q. Wan, H. Wu and X. Qu, Combustion Synthesis and Excellent Photocatalytic Degradation Properties of W18O49, *CrystEngComm*, 2015, **17**(31), 5889–5894, DOI: **10.1039/c5ce00995b**.

196 L. S. R. Yadav, R. Thippeswamy, P. Shekarappa, R. G. Kempegowda and N. Ganganagappa, Photocatalytic Activities, Kinetics and Adsorption Isotherm Studies of CeO_2 Nanoparticles Synthesized via Low Temperature Combustion Method, *Curr. Nanomater.*, 2019, **4**(3), 223–234, DOI: **10.2174/2405461504666191011171031**.

197 T. N. Ravishankar, T. Ramakrishnappa, G. Nagaraju and H. Rajanaika, Synthesis and Characterization of CeO_2 Nanoparticles via Solution Combustion Method for Photocatalytic and Antibacterial Activity Studies, *ChemistryOpen*, 2015, **4**(2), 146–154, DOI: **10.1002/open.201402046**.

198 J. La, Y. Huang, G. Luo, J. Lai, C. Liu and G. Chu, Synthesis of Bismuth Oxide Nanoparticles by Solution Combustion Method, *Part. Sci. Technol.*, 2013, **31**(3), 287–290, DOI: **10.1080/02726351.2012.727525**.

199 M. Montero-Muñoz, J. E. Ramos-Ibarra, J. E. Rodríguez-Páez, M. D. Teodoro, G. E. Marques, A. R. Sanabria, P. C. Cajas, C. A. Páez, B. Heinrichs and J. A. H. Coaquira, Role of Defects on the Enhancement of the Photocatalytic Response of ZnO Nanostructures, *Appl. Surf. Sci.*, 2018, **448**, 646–654, DOI: **10.1016/j.apsusc.2018.04.105**.

200 Y. Kitamura, N. Okinaka, T. Shibayama, O. O. P. Mahaney, D. Kusano, B. Ohtani and T. Akiyama, Combustion Synthesis of TiO2 Nanoparticles as Photocatalyst, *Powder Technol.*, 2007, **176**(2–3), 93–98, DOI: **10.1016/j.powtec.2007.02.009**.

201 G. V. Khade, M. B. Suwarnkar, N. L. Gavade and K. M. Garadkar, Green Synthesis of TiO2 and Its Photocatalytic Activity, *J. Mater. Sci.: Mater. Electron.*, 2015, **26**(5), 3309–3315, DOI: **10.1007/s10854-015-2832-7**.

202 T. Aarthi and G. Madras, Photocatalytic Reduction of Metals in Presence of Combustion Synthesized Nano-TiO2, *Catal. Commun.*, 2008, **9**(5), 630–634, DOI: **10.1016/j.catcom.2007.07.001**.

203 S. M. Khaliullin, V. D. Zhuravlev, L. V. Ermakova, L. Y. Buldakova, M. Y. Yanchenko and N. M. Porotnikova, Solution Combustion Synthesis of ZnO Using Binary Fuel (Glycine + Citric Acid), *Int. J. Self-Propag. High-Temp. Synth.*, 2019, **28**(4), 226–232, DOI: **10.3103/S1061386219040058**.

204 D. N. V. V. Konda Lutukurthi, S. Dutta and D. K. Behara, Effect of Ignition Temperature and Fuel Amount on Photocatalytic Activity of Solution Combustion Synthesized ZnO, *Ceram. Int.*, 2020, **46**(14), 22419–22428, DOI: **10.1016/j.ceramint.2020.05.324**.

205 Y. Köseoğlu, A Simple Microwave-Assisted Combustion Synthesis and Structural, Optical and Magnetic Characterization of ZnO Nanoplatelets, *Ceram. Int.*, 2014, **40**(3), 4673–4679, DOI: **10.1016/j.ceramint.2013.09.008**.

206 A. J. Reddy, M. K. Kokila, H. Nagabhushana, R. P. S. Chakradhar, C. Shivakumara, J. L. Rao and

B. M. Nagabhushana, Structural, Optical and EPR Studies on ZnO:Cu Nanopowders Prepared via Low Temperature Solution Combustion Synthesis, *J. Alloys Compd.*, 2011, **509**(17), 5349–5355, DOI: **10.1016/j.jallcom.2011.02.043**.

207 J. K. Li and X. Liu, Effects of Fuel on Morphology and Photocatalytic Performance of ZnO Nanorods Synthesized by Solution Combustion Method, *J. Inorg. Mater.*, 2013, **28**(8), 880–884, DOI: **10.3724/SP.J.1077.2013.12634**.

208 T. P. Krishna Murthy, B. S. Gowrishankar, R. H. Krishna, M. N. Chandraprabha and R. Sreenivasa Rao, Influence of Fuel Nature on Dye Adsorption Efficiency of Solution Combustion Derived Zinc Oxide Nanoparticles: A Comparative Study, *Mater. Res. Express*, 2019, **6**(5), 055512, DOI: **10.1088/2053-1591/aafe3f**.

209 K. R. Basavalingiah, S. Harishkumar, Udayabhanu, G. Nagaraju, D. Rangappa and Chikkahanumantharayappa, Highly Porous, Honeycomb like Ag–ZnO Nanomaterials for Enhanced Photocatalytic and Photoluminescence Studies: Green Synthesis Using Azadirachta Indica Gum, *SN Appl. Sci.*, 2019, **1**(8), 935, DOI: **10.1007/s42452-019-0863-z**.

210 S. M. Mane, A. R. Nimbalkar, J. S. Go, N. B. Patil, S. S. Dhasade, J. V. Thombare, A. S. Burungale and J. C. Shin, NO2 Sensing Properties of 3D Flower-like ZnO Nanostructure Decorated with Thin Porous Petals Synthesized Using a Simple Sol–Gel Drop-Casting Method, *Appl. Phys. A: Mater. Sci. Process.*, 2021, **127**(1), 13, DOI: **10.1007/s00339-020-04152-7**.

211 P. R. Potti and V. C. Srivastava, Comparative Studies on Structural, Optical, and Textural Properties of Combustion Derived ZnO Prepared Using Various Fuels and Their Photocatalytic Activity, *Ind. Eng. Chem. Res.*, 2012, **51**(23), 7948–7956, DOI: **10.1021/ie300478y**.

212 S. Azizi, R. Mohamad, M. M. Shahri and D. J. McPhee, Green Microwave-Assisted Combustion Synthesis of Zinc Oxide Nanoparticles with Citrullus Colocynthis (L.) Schrad: Characterization and Biomedical Applications, *Molecules*, 2017, **22**(2), 1–13, DOI: **10.3390/molecules22020301**.

213 A. Lassoued, B. Dkhil, A. Gadri and S. Ammar, Control of the Shape and Size of Iron Oxide (α-Fe2O3) Nanoparticles Synthesized through the Chemical Precipitation Method, *Results Phys.*, 2017, **7**, 3007–3015, DOI: **10.1016/j.rinp.2017.07.066**.

214 P. C. Ricci, C. M. Carbonaro, R. Corpino, D. Chiriu and L. Stagi, *Surface Effects and Phase Stability in Metal Oxides Nanoparticles under Visible Irradiation*, 2014, vol. 1624, pp 104–110. DOI: **10.1063/1.4900464**.

215 M. Mishra and D. M. Chun, α-Fe2O3 as a Photocatalytic Material: A Review, *Appl. Catal., A*, 2015, 126–141, DOI: **10.1016/j.apcata.2015.03.023**.

216 M. Huang, M. Qin, P. Chen, B. Jia, Z. Chen, R. Li, Z. Liu and X. Qu, Facile Preparation of Network-like Porous Hematite (α-Fe2O3) Nanosheets via a Novel Combustion-Based Route, *Ceram. Int.*, 2016, **42**(8), 10380–10388, DOI: **10.1016/j.ceramint.2016.03.175**.

217 S. Punitha and L. C. Nehru, Direct Synthesis of Iron Oxide (α -Fe 2 O 3) Nanoparticles by the Combustion Approach, *Adv. Sci. Lett.*, 2018, **24**(8), 5608–5610, DOI: **10.1166/asl.2018.12159**.

218 H. Aali, S. Mollazadeh and J. V. Khaki, Single-Phase Magnetite with High Saturation Magnetization Synthesized via Modified Solution Combustion Synthesis Procedure, *Ceram. Int.*, 2018, **44**(16), 20267–20274, DOI: **10.1016/j.ceramint.2018.08.012**.

219 A. S. Mukasyan, Solution Combustion as a Promising Method for the Synthesis of Nanomaterials, *Adv. Sci. Technol.*, 2010, **63**, 187–196, DOI: **10.4028/www.scientific.net/ast.63.187**.

220 S. Hadadian, S. M. Masoudpanah and S. Alamolhoda, Solution Combustion Synthesis of Fe 3 O 4 Powders Using Mixture of CTAB and Citric Acid Fuels, *J. Supercond. Novel Magn.*, 2019, **32**(2), 353–360, DOI: **10.1007/s10948-018-4685-9**.

221 A. B. Lesbayev, G. T. Smagulova, S. Kim, N. G. Prikhod'ko, S. M. Manakov, N. Guseinov and Z. A. Mansurov, Solution-Combustion Synthesis and Characterization of Fe3O4 Nanoparticles, *Int. J. Self-Propag. High-Temp. Synth.*, 2018, **27**(3), 195–197, DOI: **10.3103/S1061386218030068**.

222 A. A. Jahagirdar, M. N. Z. Ahmed, N. Donappa, H. Nagabhushana and B. M. Nagabhushana, Solution Combustion Synthesis and Photocatalytic Activity of α-Fe2o3 Nanopowder, *Trans. Indian Ceram. Soc.*, 2011, **70**(3), 159–162, DOI: **10.1080/0371750X.2011.10600164**.

223 X. Wang, M. Qin, F. Fang, B. Jia, H. Wu, X. Qu and A. A. Volinsky, Effect of Glycine on One-Step Solution Combustion Synthesis of Magnetite Nanoparticles, *J. Alloys Compd.*, 2017, **719**, 288–295, DOI: **10.1016/j.jallcom.2017.05.187**.

224 N. Rahimi, R. A. Pax and E. M. A. Gray, Review of Functional Titanium Oxides. I: TiO2 and Its Modifications, *Prog. Solid State Chem.*, 2016, 86–105, DOI: **10.1016/j.progsolidstchem.2016.07.002**.

225 F. A. Deorsola and D. Vallauri, Synthesis of TiO2 Nanoparticles through the Gel Combustion Process, *J. Mater. Sci.*, 2008, **43**(9), 3274–3278, DOI: **10.1007/s10853-008-2530-4**.

226 M. Y. Nassar, E. I. Ali and E. S. Zakaria, Tunable Auto-Combustion Preparation of TiO2 Nanostructures as Efficient Adsorbents for the Removal of an Anionic Textile Dye, *RSC Adv.*, 2017, **7**(13), 8034–8050, DOI: **10.1039/c6ra27924d**.

227 S. L. Chung and C. M. Wang, Solution Combustion Synthesis of TiO 2 and Its Use for Fabrication of Photoelectrode for Dye-Sensitized Solar Cell, *J. Mater. Sci. Technol.*, 2012, **28**(8), 713–722, DOI: **10.1016/S1005-0302(12)60120-0**.

228 S. Challagulla and S. Roy, The Role of Fuel to Oxidizer Ratio in Solution Combustion Synthesis of TiO2and Its Influence on Photocatalysis, *J. Mater. Res.*, 2017, **32**(14), 2764–2772, DOI: **10.1557/jmr.2017.244**.

229 D. O. Scanlon, C. W. Dunnill, J. Buckeridge, S. A. Shevlin, A. J. Logsdail, S. M. Woodley, C. R. A. Catlow, M. J. Powell,

R. G. Palgrave, I. P. Parkin, *et al.*, Band Alignment of Rutile and Anatase TiO2, *Nat. Mater.*, 2013, **12**(9), 798–801, DOI: **10.1038/nmat3697**.

230 K. Nagaveni, M. S. Hegde, N. Ravishankar, G. N. Subbanna and G. Madras, Synthesis and Structure of Nanocrystalline TiO2 with Lower Band Gap Showing High Photocatalytic Activity, *Langmuir*, 2004, **20**(7), 2900–2907, DOI: **10.1021/la035777v**.

231 N. K. Eswar, P. C. Ramamurthy and G. Madras, High Photoconductive Combustion Synthesized TiO2 Derived Nanobelts for Photocatalytic Water Purification under Solar Irradiation, *New J. Chem.*, 2015, **39**(8), 6040–6051, DOI: **10.1039/c5nj01001b**.

232 Y. Wicaksana, S. Liu, J. Scott and R. Amal, Tungsten Trioxide as a Visible Light Photocatalyst for Volatile Organic Carbon Removal, *Molecules*, 2014, **19**(11), 17747–17762, DOI: **10.3390/molecules191117747**.

233 T. T. Nguyen, S. N. Nam, J. Son and J. Oh, Tungsten Trioxide (WO3)-Assisted Photocatalytic Degradation of Amoxicillin by Simulated Solar Irradiation, *Sci. Rep.*, 2019, **9**(1), 1–18, DOI: **10.1038/s41598-019-45644-8**.

234 C. M. Wu, S. Naseem, M. H. Chou, J. H. Wang and Y. Q. Jian, Recent Advances in Tungsten-Oxide-Based Materials and Their Applications, *Front. Mater.*, 2019, 49, DOI: **10.3389/fmats.2019.00049**.

235 Y. Kong, H. Sun, X. Zhao, B. Gao and W. Fan, Fabrication of Hexagonal/Cubic Tungsten Oxide Homojunction with Improved Photocatalytic Activity, *Appl. Catal., A*, 2015, **505**, 447–455, DOI: **10.1016/j.apcata.2015.05.015**.

236 X. Liu, H. Zhai, P. Wang, Q. Zhang, Z. Wang, Y. Liu, Y. Dai, B. Huang, X. Qin and X. Zhang, Synthesis of a WO 3 Photocatalyst with High Photocatalytic Activity and Stability Using Synergetic Internal Fe 3 + Doping and Superficial Pt Loading for Ethylene Degradation under Visible-Light Irradiation, *Catal. Sci. Technol.*, 2019, **9**(3), 652–658, DOI: **10.1039/c8cy02375a**.

237 Z. Shen, Z. Zhao, J. Qian, Z. Peng and X. Fu, Synthesis of WO3-x Nanomaterials with Controlled Morphology and Composition for Highly Efficient Photocatalysis, *J. Mater. Res.*, 2016, **31**(8), 1065–1076, DOI: **10.1557/jmr.2016.106**.

238 H. Nasiri, J. Vahdati Khaki and S. M. Zebarjad, One-Step Fabrication of Cu-Al2O3 Nanocomposite via Solution Combustion Synthesis Route, *J. Alloys Compd.*, 2011, **509**(17), 5305–5308, DOI: **10.1016/j.jallcom.2011.01.185**.

239 M. Verma, M. Mitan, H. Kim and D. Vaya, Efficient Photocatalytic Degradation of Malachite Green Dye Using Facilely Synthesized Cobalt Oxide Nanomaterials Using Citric Acid and Oleic Acid, *J. Phys. Chem. Solids*, 2021, **155**, 110125, DOI: **10.1016/j.jpcs.2021.110125**.

240 B. Babu, A. N. Kadam, R. V. S. S. N. Ravikumar and C. Byon, Enhanced Visible Light Photocatalytic Activity of Cu-Doped SnO2quantum Dots by Solution Combustion Synthesis, *J. Alloys Compd.*, 2017, **703**, 330–336, DOI: **10.1016/j.jallcom.2017.01.311**.

241 M. S. Morassaei, S. Zinatloo-Ajabshir and M. Salavati-Niasari, Simple Salt-Assisted Combustion Synthesis of Nd2Sn2O7–SnO2 Nanocomposites with Different Amino Acids as Fuel: An Efficient Photocatalyst for the Degradation of Methyl Orange Dye, *J. Mater. Sci.: Mater. Electron.*, 2016, **27**(11), 11698–11706, DOI: **10.1007/s10854-016-5306-7**.

242 R. Bakkiyaraj, G. Bharath, K. Hasini Ramsait, A. Abdel-Wahab, E. H. Alsharaeh, S. M. Chen and M. Balakrishnan, Solution Combustion Synthesis and Physico-Chemical Properties of Ultrafine CeO_2 Nanoparticles and Their Photocatalytic Activity, *RSC Adv.*, 2016, **6**(56), 51238–51245, DOI: **10.1039/c6ra00382f**.

243 S. Polisetti, P. A. Deshpande and G. Madras, Photocatalytic Activity of Combustion Synthesized ZrO2 and ZrO2-TiO2 Mixed Oxides, *Ind. Eng. Chem. Res.*, 2011, **50**(23), 12915–12924, DOI: **10.1021/ie200350f**.

244 E. D. Sherly, J. J. Vijaya, N. C. S. Selvam and L. J. Kennedy, Microwave Assisted Combustion Synthesis of Coupled ZnO-ZrO2 Nanoparticles and Their Role in the Photocatalytic Degradation of 2,4-Dichlorophenol, *Ceram. Int.*, 2014, **40**(4), 5681–5691, DOI: **10.1016/j.ceramint.2013.11.006**.

245 X. Li, J. Yu and C. Jiang, Principle and Surface Science of Photocatalysis, in *Interface Science and Technology*, Elsevier B.V., 2020, vol. 31, pp. 1–38. DOI: **10.1016/B978-0-08-102890-2.00001-4**.

246 T. V. Anuradha and S. Ranganathan, Nanocrystalline TiO2 by Three Different Synthetic Approaches: A Comparison, *Bull. Mater. Sci.*, 2007, **30**(3), 263–269, DOI: **10.1007/s12034-007-0046-1**.

247 F. Gunkel, D. V. Christensen, Y. Z. Chen and N. Pryds, Oxygen Vacancies: The (in)Visible Friend of Oxide Electronics, *Appl. Phys. Lett.*, 2020, 120505, DOI: **10.1063/1.5143309**.

248 H. H. Lo, N. O. Gopal and S. C. Ke, Origin of Photoactivity of Oxygen-Deficient TiO2 under Visible Light, *Appl. Phys. Lett.*, 2009, **95**(8), 083126, DOI: **10.1063/1.3216585**.

249 H. Cui, H. Liu, J. Shi and C. Wang, Function of TiO2 Lattice Defects toward Photocatalytic Processes: View of Electronic Driven Force, *Int. J. Photoenergy*, 2013, **2013**, 364802, DOI: **10.1155/2013/364802**.

250 M. S. Hegde, K. Nagaveni and S. Roy, Synthesis, Structure and Photocatalytic Activity of Nano TiO2 and Nano Ti1-XMxO2-δ (M = Cu, Fe, Pt, Pd, V, W, Ce, Zr), *Pramana - J. Phys.*, 2005, **65**(4 SPEC. ISS.), 641–645, DOI: **10.1007/bf03010452**.

251 X. Chen, L. Liu, P. Y. Yu and S. S. Mao, Increasing Solar Absorption for Photocatalysis with Black Hydrogenated Titanium Dioxide Nanocrystals, *Science*, 2011, **331**(6018), 746–750, DOI: **10.1126/science.1200448**.

252 S. G. Ullattil and P. Periyat, A "one Pot" Gel Combustion Strategy towards Ti3 + Self-Doped "Black" Anatase TiO2-x Solar Photocatalyst, *J. Mater. Chem. A*, 2016, **4**(16), 5854–5858, DOI: **10.1039/c6ta01993e**.

253 K. Karthik, M. Madhukara Naik, M. Shashank, M. Vinuth and V. Revathi, Microwave-Assisted ZrO 2 Nanoparticles and Its Photocatalytic and Antibacterial Studies, *J. Cluster*

Sci., 2019, **30**(2), 311–318, DOI: 10.1007/s10876-018-1484-1.

254 J. Wan, X. Yao, X. Gao, X. Xiao, T. Li, J. Wu, W. Sun, Z. Hu, H. Yu, L. Huang, *et al.*, Microwave Combustion for Modification of Transition Metal Oxides, *Adv. Funct. Mater.*, 2016, **26**(40), 7263–7270, DOI: 10.1002/adfm.201603125.

255 P. Suresh, J. J. Vijaya and L. J. Kennedy, Photocatalytic Degradation of Textile-Dyeing Wastewater by Using a Microwave Combustion-Synthesized Zirconium Oxide Supported Activated Carbon, *Mater. Sci. Semicond. Process.*, 2014, **27**(1), 482–493, DOI: 10.1016/j.mssp.2014.06.050.

256 A. Talati and M. Haghighi, Influence of Fuel Type and Heating Approach on One-Step Microwave Combustion Design of Zn-Spinel as Supreme Sunlight-Responsive Nanophotocatalyst for Degradation of Orange II in Water, *Sol. Energy*, 2022, **234**, 275–293, DOI: 10.1016/J.SOLENER.2022.02.003.

257 E. D. Sherly, J. J. Vijaya and L. J. Kennedy, Effect of CeO_2 Coupling on the Structural, Optical and Photocatalytic Properties of ZnO Nanoparticle, *J. Mol. Struct.*, 2015, **1099**, 114–125, DOI: 10.1016/j.molstruc.2015.05.057.

258 L. C. Nehru, V. Swaminathan and C. Sanjeeviraja, Rapid Synthesis of Nanocrystalline ZnO by a Microwave-Assisted Combustion Method, *Powder Technol.*, 2012, **226**, 29–33, DOI: 10.1016/j.powtec.2012.03.042.

259 S. Ekambaram, Y. Iikubo and A. Kudo, Combustion Synthesis and Photocatalytic Properties of Transition Metal-Incorporated ZnO, *J. Alloys Compd.*, 2007, **433**(1–2), 237–240, DOI: 10.1016/j.jallcom.2006.06.045.

260 R. V. Mangalaraja, J. Mouzon, P. Hedström, C. P. Camurri, S. Ananthakumar and M. Odén, Microwave Assisted Combustion Synthesis of Nanocrystalline Yttria and Its Powder Characteristics, *Powder Technol.*, 2009, **191**(3), 309–314, DOI: 10.1016/j.powtec.2008.10.019.

261 N. M. Mahmoodi, O. Masrouri and A. M. Arabi, Synthesis of Porous Adsorbent Using Microwave Assisted Combustion Method and Dye Removal, *J. Alloys Compd.*, 2014, **602**, 210–220, DOI: 10.1016/j.jallcom.2014.02.155.

262 K. M. Navada, G. K. Nagaraja, J. N. D'Souza, S. Kouser, R. Ranjitha and D. J. Manasa, Phyto Assisted Synthesis and Characterization of Scoparia Dulsis L. Leaf Extract Mediated Porous Nano CuO Photocatalysts and Its Anticancer Behavior, *Appl. Nanosci.*, 2020, **1**, 3, DOI: 10.1007/s13204-020-01536-2.

263 E. Abbasi, M. Haghighi, R. Shokrani and M. Shabani, Copper Plasmon-Induced Cu-Doped ZnO-CuO Double-Nanoheterojunction: *In situ* Combustion Synthesis and Photo-Decontamination of Textile Effluents, *Mater. Res. Bull.*, 2020, **129**, 110880, DOI: 10.1016/j.materresbull.2020.110880.

264 S. L. González-Cortés, A. M. Aldawsari and S. Rodulfo-Baechler, *Green Chemistry for Solution Combustion Synthesis of Advanced Catalysts and Materials*, 2020, pp. 1–47. DOI: 10.1142/9781786348708_0001.

265 X. Hao and Y. Zhang, Low Temperature Gel-Combustion Synthesis of Porous Nanostructure LaFeO3 with Enhanced Visible-Light Photocatalytic Activity in Reduction of Cr(VI), *Mater. Lett.*, 2017, **197**, 120–122, DOI: 10.1016/j.matlet.2017.03.133.

266 G. Falk, M. Borlaf, T. Bendo, A. P. Novaes De Oliveira, J. B. Rodrigues Neto, R. Moreno and P. Gouma, Colloidal Sol-Gel Synthesis and Photocatalytic Activity of Nanoparticulate Nb2O5 Sols, *J. Am. Ceram. Soc.*, 2016, **99**(6), 1968–1973, DOI: 10.1111/jace.14217.

267 A. A. Voskanyan, K. Y. Chan and C. Y. V. Li, Colloidal Solution Combustion Synthesis: Toward Mass Production of a Crystalline Uniform Mesoporous CeO_2 Catalyst with Tunable Porosity, *Chem. Mater.*, 2016, **28**(8), 2768–2775, DOI: 10.1021/acs.chemmater.6b00505.

268 Z. Shang, Z. Yang, Y. Xiao and X. Wang, Ordered Mesoporous Ag/CeO_2 Nanocrystalline via Silica-Templated Solution Combustion for Enhanced Photocatalytic Performance, *Colloids Surf., A*, 2020, **604**, 125301, DOI: 10.1016/j.colsurfa.2020.125301.

269 K. V. Manukyan, Y. S. Chen, S. Rouvimov, P. Li, X. Li, S. Dong, X. Liu, J. K. Furdyna, A. Orlov, G. H. Bernstein, *et al.*, Ultrasmall α-Fe2O3 Superparamagnetic Nanoparticles with High Magnetization Prepared by Template-Assisted Combustion Process, *J. Phys. Chem. C*, 2014, **118**(29), 16264–16271, DOI: 10.1021/jp504733r.

270 S. Bai, N. Zhang, C. Gao and Y. Xiong, Defect Engineering in Photocatalytic Materials, *Nano Energy*, 2018, 296–336, DOI: 10.1016/j.nanoen.2018.08.058.

271 R. Y. S. Zampiva, C. P. Bergmann, A. K. Alves and L. Giorgini, Solution Combustion Synthesis of Mo-Fe/MgO: Influence of the Fuel Composition on the Production of Doped Catalyst Nanopowder, in *IOP Conference Series: Materials Science and Engineering*, Institute of Physics Publishing, 2019, vol. 659, p. 012078. DOI: 10.1088/1757-899X/659/1/012078.

272 K. V. A. Kumar, S. R. Amanchi, B. Sreedhar, P. Ghosal and C. Subrahmanyam, Phenol and Cr(VI) Degradation with Mn Ion Doped ZnO under VIsible Light Photocatalysis, *RSC Adv.*, 2017, **7**(68), 43030–43039, DOI: 10.1039/c7ra08172c.

273 S. Vadivel and G. Rajarajan, Influence of Cu Doping on Structural, Optical and Photocatalytic Activity of SnO2 Nanostructure Thin Films, *J. Mater. Sci.: Mater. Electron.*, 2015, **26**(8), 5863–5870, DOI: 10.1007/s10854-015-3154-5.

274 B. Babu, A. N. Kadam, R. V. S. S. N. Ravikumar and C. Byon, Enhanced Visible Light Photocatalytic Activity of Cu-Doped SnO2quantum Dots by Solution Combustion Synthesis, *J. Alloys Compd.*, 2017, **703**, 330–336, DOI: 10.1016/j.jallcom.2017.01.311.

275 B. Babu, A. N. Kadam, G. T. Rao, S. W. Lee, C. Byon and J. Shim, Enhancement of Visible-Light-Driven Photoresponse of Mn-Doped SnO2 Quantum Dots Obtained by Rapid and Energy Efficient Synthesis, *J. Lumin.*, 2018, **195**, 283–289, DOI: 10.1016/j.jlumin.2017.11.040.

276 V. Kumar, V. Kumar, S. Som, J. H. Neethling, E. Olivier, O. M. Ntwaeaborwa and H. C. Swart, The Role of Surface and Deep-Level Defects on the Emission of Tin Oxide Quantum Dots, *Nanotechnology*, 2014, **25**(13), 135701, DOI: **10.1088/0957-4484/25/13/135701**.

277 A. Escudero, A. I. Becerro, C. Carrillo-Carrión, N. O. Núñez, M. V. Zyuzin, M. Laguna, D. González-Mancebo, M. Ocanã and W. J. Parak, Rare Earth Based Nanostructured Materials: Synthesis, Functionalization, Properties and Bioimaging and Biosensing Applications, *Nanophotonics*, 2017, 881–921, DOI: **10.1515/nanoph-2017-0007**.

278 R. Venkatesh, L. S. R. Yadav, N. Dhananjaya and A. Jayasheelan, Green Combustion Synthesis of ZnAl2O4: Eu3 + Nanoparticle for Photocatalytic Activity, in *Materials Today: Proceedings*, Elsevier, 2021, vol. 49, pp. 583–587. DOI: **10.1016/j.matpr.2021.04.508**.

279 S. M. Tikhanova, L. A. Lebedev, K. D. Martinson, M. I. Chebanenko, I. V. Buryanenko, V. G. Semenov, V. N. Nevedomskiy and V. I. Popkov, The Synthesis of Novel Heterojunction H-YbFeO3/o-YbFeO3photocatalyst with Enhanced Fenton-like Activity under Visible-Light, *New J. Chem.*, 2021, **45**(3), 1541–1550, DOI: **10.1039/d0nj04895j**.

280 Z. Rao, X. Xie, X. Wang, A. Mahmood, S. Tong, M. Ge and J. Sun, Defect Chemistry of Er3 + -Doped TiO2 and Its Photocatalytic Activity for the Degradation of Flowing Gas-Phase VOCs, *J. Phys. Chem. C*, 2019, **123**(19), 12321–12334, DOI: **10.1021/acs.jpcc.9b02093**.

281 I. Ahmad, M. E. Mazhar, M. N. Usmani, M. Mehmood, W. Abbas, N. Akhtar and E. Ahmed, Auto-Combustion Synthesis of Pure and Er, Dy Co-Doped ZnO Nanomaterials for Efficient Methyl Orange Degradation Using Solar and Visible Light Photocatalysis, *Mater. Res. Express*, 2019, **6**(7), 075044, DOI: **10.1088/2053-1591/ab1562**.

282 I. Ahmad, M. Shoaib Akhtar, E. Ahmed, M. Ahmad, V. Keller, W. Qamar Khan and N. R. Khalid, Rare Earth Co-Doped ZnO Photocatalysts: Solution Combustion Synthesis and Environmental Applications, *Sep. Purif. Technol.*, 2020, **237**(August), 116328, DOI: **10.1016/j.seppur.2019.116328**.

283 M. Faraz, F. K. Naqvi, M. Shakir and N. Khare, Synthesis of Samarium-Doped Zinc Oxide Nanoparticles with Improved Photocatalytic Performance and Recyclability under Visible Light Irradiation, *New J. Chem.*, 2018, **42**(3), 2295–2305, DOI: **10.1039/c7nj03927a**.

284 Q. Xiao, Z. Si, Z. Yu and G. Qiu, Sol-Gel Auto-Combustion Synthesis of Samarium-Doped TiO2 Nanoparticles and Their Photocatalytic Activity under Visible Light Irradiation, *Mater. Sci. Eng., B*, 2007, **137**(1–3), 189–194, DOI: **10.1016/j.mseb.2006.11.011**.

285 V. Štengl, S. Bakardjieva and N. Murafa, Preparation and Photocatalytic Activity of Rare Earth Doped TiO2 Nanoparticles, *Mater. Chem. Phys.*, 2009, **114**(1), 217–226, DOI: **10.1016/j.matchemphys.2008.09.025**.

286 S. Liang, T. Zhang, D. Zhang, X. Pu, X. Shao, W. Li and J. Dou, One-Pot Combustion Synthesis and Efficient Broad Spectrum Photoactivity of Bi/BiOBr:Yb,Er/C Photocatalyst, *J. Am. Ceram. Soc.*, 2018, **101**(8), 3424–3436, DOI: **10.1111/jace.15520**.

287 J. Payormhorm and R. Idem, Synthesis of C-Doped TiO2 by Sol-Microwave Method for Photocatalytic Conversion of Glycerol to Value-Added Chemicals under Visible Light, *Appl. Catal., A*, 2020, **590**, 117362, DOI: **10.1016/j.apcata.2019.117362**.

288 M. Shen, Z. Wu, H. Huang, Y. Du, Z. Zou and P. Yang, Carbon-Doped Anatase TiO2 Obtained from TiC for Photocatalysis under Visible Light Irradiation, *Mater. Lett.*, 2006, **60**(5), 693–697, DOI: **10.1016/j.matlet.2005.09.068**.

289 R. Asahi, T. Morikawa, T. Ohwaki, K. Aoki and Y. Taga, Visible-Light Photocatalysis in Nitrogen-Doped Titanium Oxides, *Science*, 2001, **293**(5528), 269–271, DOI: **10.1126/science.1061051**.

290 E. M. Neville, M. J. Mattle, D. Loughrey, B. Rajesh, M. Rahman, J. M. D. MacElroy, J. A. Sullivan and K. R. Thampi, Carbon-Doped TiO 2 and Carbon, Tungsten-Codoped TiO 2 through Sol-Gel Processes in the Presence of Melamine Borate: Reflections through Photocatalysis, *J. Phys. Chem. C*, 2012, **116**(31), 16511–16521, DOI: **10.1021/jp303645p**.

291 H. Guo, Z. Zheng, J. Chen, W. Weng and M. Huang, Facile Template-Free One-Pot Fabrication of TiO2at C Microspheres with High Visible-Light Photocatalytic Degradation Activity, *J. Ind. Eng. Chem.*, 2016, **36**, 306–313, DOI: **10.1016/j.jiec.2016.02.018**.

292 S. Sakthivel and H. Kisch, Daylight Photocatalysis by Carbon-Modified Titanium Dioxide, *Angew. Chem., Int. Ed.*, 2003, **42**(40), 4908–4911, DOI: **10.1002/anie.200351577**.

293 S. Sakthivel, M. Janczarek and H. Kisch, Visible Light Activity and Photoelectrochemical Properties of Nitrogen-Doped TiO2, *J. Phys. Chem. B*, 2004, **108**(50), 19384–19387, DOI: **10.1021/jp046857q**.

294 A. D. Mani, P. M. K. Reddy, M. Srinivaas, P. Ghosal, N. Xanthopoulos and C. Subrahmanyam, Facile Synthesis of Efficient Visible Active C-Doped TiO2 Nanomaterials with High Surface Area for the Simultaneous Removal of Phenol and Cr(VI), *Mater. Res. Bull.*, 2015, **61**, 391–399, DOI: **10.1016/j.materresbull.2014.10.051**.

295 Q. Xiao and L. Ouyang, Photocatalytic Activity and Hydroxyl Radical Formation of Carbon-Doped TiO2 Nanocrystalline: Effect of Calcination Temperature, *Chem. Eng. J.*, 2009, **148**(2–3), 248–253, DOI: **10.1016/j.cej.2008.08.024**.

296 Q. Xiao, J. Zhang, C. Xiao, Z. Si and X. Tan, Solar Photocatalytic Degradation of Methylene Blue in Carbon-Doped TiO2 Nanoparticles Suspension, *Sol. Energy*, 2008, **82**(8), 706–713, DOI: **10.1016/j.solener.2008.02.006**.

297 G. Kale, S. Arbuj, U. Kawade, S. Rane, J. Ambekar and B. Kale, Synthesis of Porous Nitrogen Doped Zinc Oxide

Nanostructures Using a Novel Paper Mediated Template Method and Their Photocatalytic Study for Dye Degradation under Natural Sunlight, *Mater. Chem. Front.*, 2018, **2**(1), 163–170, DOI: **10.1039/C7QM00490G**.

298 M. Zheng and J. Wu, One-Step Synthesis of Nitrogen-Doped ZnO Nanocrystallites and Their Properties, *Appl. Surf. Sci.*, 2009, **255**(11), 5656–5661, DOI: **10.1016/j.apsusc.2008.10.091**.

299 X. Zhang, J. Qin, R. Hao, L. Wang, X. Shen, R. Yu, S. Limpanart, M. Ma and R. Liu, Carbon-Doped ZnO Nanostructures: Facile Synthesis and Visible Light Photocatalytic Applications, *J. Phys. Chem. C*, 2015, **119**(35), 20544–20554, DOI: **10.1021/acs.jpcc.5b07116**.

300 H. Raether, *Surface Plasmons on Smooth Surfaces*, Springer, Berlin, Heidelberg, 1988, pp. 4–39. DOI: **10.1007/bfb0048319**.

301 K. H. Chen, Y. C. Pu, K. D. Chang, Y. F. Liang, C. M. Liu, J. W. Yeh, H. C. Shih and Y. J. Hsu, Ag-Nanoparticle-Decorated SiO 2 Nanospheres Exhibiting Remarkable Plasmon-Mediated Photocatalytic Properties, *J. Phys. Chem. C*, 2012, **116**(35), 19039–19045, DOI: **10.1021/jp306555j**.

302 H. Eom, J. Y. Jung, Y. Shin, S. Kim, J. H. Choi, E. Lee, J. H. Jeong and I. Park, Strong Localized Surface Plasmon Resonance Effects of Ag/TiO2 Core-Shell Nanowire Arrays in UV and Visible Light for Photocatalytic Activity, *Nanoscale*, 2014, **6**(1), 226–234, DOI: **10.1039/c3nr04388f**.

303 T. K. Pathak, H. C. Swart and R. E. Kroon, Structural and Plasmonic Properties of Noble Metal Doped ZnO Nanomaterials, *Physica B: Condens. Matter*, 2018, **535**, 114–118, DOI: **10.1016/j.physb.2017.06.074**.

304 T. K. Pathak, R. E. Kroon and H. C. Swart, Photocatalytic and Biological Applications of Ag and Au Doped ZnO Nanomaterial Synthesized by Combustion, *Vacuum*, 2018, **157**, 508–513, DOI: **10.1016/j.vacuum.2018.09.020**.

305 T. I. Chanu, T. Muthukumar and P. T. Manoharan, Fuel Mediated Solution Combustion Synthesis of ZnO Supported Gold Clusters and Nanoparticles and Their Catalytic Activity and in Vitro Cytotoxicity, *Phys. Chem. Chem. Phys.*, 2014, **16**(43), 23686–23698, DOI: **10.1039/c4cp03393k**.

306 S. A. Ansari, M. M. Khan, J. Lee and M. H. Cho, Highly Visible Light Active Ag@ZnO Nanocomposites Synthesized by Gel-Combustion Route, *J. Ind. Eng. Chem.*, 2014, **20**(4), 1602–1607, DOI: **10.1016/j.jiec.2013.08.006**.

307 P. Arunkumar, R. Aadhavan, S. Bhanuchandar and K. Suresh Babu, Effect, of Fuel Ratio on Combustion Synthesis and Properties of Magnetic Nanostructures, *Mater. Res. Express*, 2014, **1**(3), 035011, DOI: **10.1088/2053-1591/1/3/035011**.

308 H. Kazemi, F. Kermani, S. Mollazadeh and J. Vahdati Khakhi, The, Significant Role of the Glycine-Nitrate Ratio on the Physicochemical Properties of CoxZn1−xO Nanoparticles, *Int. J. Appl. Ceram. Technol.*, 2020, **17**(4), 1852–1868, DOI: **10.1111/ijac.13515**.

309 M. K. Hossain, E. Kecsenovity, A. Varga, M. Molnár, C. Janáky and K. Rajeshwar, Solution Combustion Synthesis of Complex Oxide Semiconductors, *Int. J. Self-Propag. High-Temp. Synth.*, 2018, **27**(3), 129–140, DOI: **10.3103/S1061386218030032**.

310 N. Velinov, T. Petrova, R. Ivanova, T. Tsoncheva, D. Kovacheva and I. Mitov, Synthesis and Characterization of Copper-Nickel Ferrite Catalysts for Ethyl Acetate Oxidation, *Hyperfine Interact.*, 2020, **241**(1), 31, DOI: **10.1007/s10751-019-1654-z**.

311 X. Du and X. Wang, Solution Combustion Synthesis of Ag-Decorated Bi5O7NO3 Composites with Enhanced Photocatalytic Properties, *Ceram. Int.*, 2019, **45**(1), 1409–1411, DOI: **10.1016/j.ceramint.2018.09.141**.

312 G. F. Samu, Á. Veres, B. Endrődi, E. Varga, K. Rajeshwar and C. Janáky, Bandgap-Engineered Quaternary MxBi2−xTi2O7 (M: Fe, Mn) Semiconductor Nanoparticles: Solution Combustion Synthesis, Characterization, and Photocatalysis, *Appl. Catal., B*, 2017, **208**, 148–160, DOI: **10.1016/j.apcatb.2017.02.036**.

313 H. Y. Hafeez, S. K. Lakhera, N. Narayanan, S. Harish, Y. Hayakawa, B. K. Lee and B. Neppolian, Environmentally Sustainable Synthesis of a CoFe2O4-TiO2/RGO Ternary Photocatalyst: A Highly Efficient and Stable Photocatalyst for High Production of Hydrogen (Solar Fuel), *ACS Omega*, 2019, **4**(1), 880–891, DOI: **10.1021/acsomega.8b03221**.

314 K. Shetty, L. Renuka, H. P. Nagaswarupa, H. Nagabhushana, K. S. Anantharaju, D. Rangappa, S. C. Prashantha and K. Ashwini, A Comparative Study on CuFe2O4, ZnFe2O4 and NiFe2O4: Morphology, Impedance and Photocatalytic Studies, in *Materials Today: Proceedings*; Elsevier Ltd, 2017, vol. 4, pp. 11806–11815. DOI: **10.1016/j.matpr.2017.09.098**.

315 D. Zhang, X. Pu, K. Du, Y. M. Yu, J. J. Shim, P. Cai, S. I. Kim and H. J. Seo, Combustion Synthesis of Magnetic Ag/NiFe2O4 Composites with Enhanced Visible-Light Photocatalytic Properties, *Sep. Purif. Technol.*, 2014, **137**, 82–85, DOI: **10.1016/j.seppur.2014.09.025**.

316 C. O. Ehi-Eromosele, B. I. Ita and E. E. J. Iweala, Low-Temperature Combustion Synthesis of Cobalt Magnesium Ferrite Magnetic Nanoparticles: Effects of Fuel-to-Oxidizer Ratio and Sintering Temperature, *J. Sol-Gel Sci. Technol.*, 2015, **76**(2), 298–308, DOI: **10.1007/s10971-015-3777-2**.

317 P. Bera, R. V. Lakshmi, B. H. Prakash, K. Tiwari, A. Shukla, A. K. Kundu, K. Biswas and H. C. Barshilia, Solution Combustion Synthesis, Characterization, Magnetic, and Dielectric Properties of CoFe2O4and Co0.5M0.5Fe2O4(M = Mn, Ni, and Zn), *Phys. Chem. Chem. Phys.*, 2020, **22**(35), 20087–20106, DOI: **10.1039/d0cp03161e**.

318 S. Meena, L. Renuka, K. S. Anantharaju, Y. S. Vidya, H. P. Nagaswarupa, S. C. Prashantha and H. Nagabhushana, Optical, Electrochemical and Photocatalytic Properties of Sunlight Driven Cu Doped Manganese Ferrite Synthesized by Solution Combustion Synthesis, in *Materials Today: Proceedings*, Elsevier Ltd,

2017, vol. 4, pp. 11773–11781. DOI: 10.1016/j.matpr.2017.09.094.

319 D. W. Kim, I. S. Cho, S. S. Shin, S. Lee, T. H. Noh, D. H. Kim, H. S. Jung and K. S. Hong, Electronic Band Structures and Photovoltaic Properties of MWO4 (M=Zn, Mg, Ca, Sr) Compounds, *J. Solid State Chem.*, 2011, **184**(8), 2103–2107, DOI: 10.1016/j.jssc.2011.06.005.

320 L. Kihlborg and E. Gebert, CuWO4, a Distorted Wolframite-Type Structure, *Acta Crystallogr., Sect. B: Struct. Crystallogr. Cryst. Chem.*, 1970, **26**(7), 1020–1026, DOI: 10.1107/s0567740870003515.

321 H. Search, C. Journals, A. Contact, M. Iopscience and I. P. Address, Structural and Electronic Properties of Epitaxial V2O3, *J. Phys.: Condens. Matter*, 2007, **77**(41), 413101, DOI: 10.1088/0953-8984.

322 J. E. Yourey and B. M. Bartlett, Electrochemical Deposition and Photoelectrochemistry of CuWO4, a Promising Photoanode for Water Oxidation, *J. Mater. Chem.*, 2011, **21**(21), 7651–7660, DOI: 10.1039/c1jm11259g.

323 A. J. van den Berg and C. A. H. Juffermans, The Polymorphism of Silver Tungstate Ag 2 WO 4, *J. Appl. Crystallogr.*, 1982, **15**(1), 114–116, DOI: 10.1107/s0021889882011510.

324 L. S. Cavalcante, M. A. P. Almeida, W. Avansi, R. L. Tranquilin, E. Longo, N. C. Batista, V. R. Mastelaro and M. S. Li, Cluster Coordination and Photoluminescence Properties of α-Ag 2WO 4 Microcrystals, *Inorg. Chem.*, 2012, **51**(20), 10675–10687, DOI: 10.1021/ic300948n.

325 H. Fu, J. Lin, L. Zhang and Y. Zhu, Photocatalytic Activities of a Novel ZnWO4 Catalyst Prepared by a Hydrothermal Process, *Appl. Catal., A*, 2006, **306**, 58–67, DOI: 10.1016/j.apcata.2006.03.040.

326 J. Ungelenk and C. Feldmann, Synthesis of Faceted β-SnWO4 Microcrystals with Enhanced Visible-Light Photocatalytic Properties, *Chem. Commun.*, 2012, **48**(63), 7838–7840, DOI: 10.1039/c2cc33224h.

327 R. Shi, Y. Wang, D. Li, J. Xu and Y. Zhu, Synthesis of ZnWO4 Nanorods with [100] Orientation and Enhanced Photocatalytic Properties, *Appl. Catal., B*, 2010, **100**(1–2), 173–178, DOI: 10.1016/j.apcatb.2010.07.027.

328 C. Zhang, H. Zhang, K. Zhang, X. Li, Q. Leng and C. Hu, Photocatalytic Activity of ZnWO4: Band Structure, Morphology and Surface Modification, *ACS Appl. Mater. Interfaces*, 2014, **6**(16), 14423–14432, DOI: 10.1021/am503696b.

329 M. H. Habibi and V. Mosavi, Urea Combustion Synthesis of Nano-Structure Bimetallic Perovskite FeMnO3 and Mixed Monometallic Iron Manganese Oxides: Effects of Preparation Parameters on Structural, Opto-Electronic and Photocatalytic Activity for Photo-Degradation of Basic Blue 12, *J. Mater. Sci.: Mater. Electron.*, 2017, **28**(12), 8473–8479, DOI: 10.1007/s10854-017-6568-4.

330 S. L. González-Cortés, T. C. Xiao, Perdo M. F. J. Costa, S. M. A. Rodulfo-Baechler and M. L. H. Green, Relevance of the Co1-XNixWO4 Wolframite-Type Mixed Oxide Compositions on the Synthesis and Catalytic Properties of W-Based Carbides, *J. Mol. Catal. A: Chem.*, 2005, **238**(1–2), 127–134, DOI: 10.1016/j.molcata.2005.05.012.

331 A. R. Abbasian and M. Rahmani, Salt-Assisted Solution Combustion Synthesis of Nanostructured ZnFe2O4-ZnS Powders, *Inorg. Chem. Commun.*, 2020, **111**, 107629, DOI: 10.1016/j.inoche.2019.107629.

332 N. J. Baygi, A. V. Saghir, S. M. Beidokhti and J. V. Khaki, Modified Auto-Combustion Synthesis of Mixed-Oxides TiO2/NiO Nanoparticles: Physical Properties and Photocatalytic Performance, *Ceram. Int.*, 2020, **46**(10), 15417–15437, DOI: 10.1016/j.ceramint.2020.03.087.

333 S. Zinatloo-Ajabshir and M. Salavati-Niasari, Preparation of Magnetically Retrievable CoFe2O4@SiO2@Dy2Ce2O7 Nanocomposites as Novel Photocatalyst for Highly Efficient Degradation of Organic Contaminants, *Composites, Part B*, 2019, **174**, 106930, DOI: 10.1016/j.compositesb.2019.106930.

334 K. Ghorai, A. Panda, M. Bhattacharjee, D. Mandal, A. Hossain, P. Bera, M. M. Seikh and A. Gayen, Facile Synthesis of CuCr2O4/CeO_2 Nanocomposite: A New Fenton like Catalyst with Domestic LED Light Assisted Improved Photocatalytic Activity for the Degradation of RhB, MB and MO Dyes, *Appl. Surf. Sci.*, 2021, **536**, 147604, DOI: 10.1016/j.apsusc.2020.147604.

335 M. A. Bajiri, A. Hezam, K. Namratha, R. Viswanath, Q. A. Drmosh, H. S. Bhojya Naik and K. Byrappa, CuO/ZnO/g-C3N4 Heterostructures as Efficient Visible Light-Driven Photocatalysts, *J. Environ. Chem. Eng.*, 2019, **7**(5), 103412, DOI: 10.1016/j.jece.2019.103412.

336 A. Kumar, L. Rout, L. S. K. Achary, S. K. Mohanty and P. Dash, A Combustion Synthesis Route for Magnetically Separable Graphene Oxide-CuFe2O4-ZnO Nanocomposites with Enhanced Solar Light-Mediated Photocatalytic Activity, *New J. Chem.*, 2017, **41**(19), 10568–10583, DOI: 10.1039/c7nj02070h.

337 M. Y. Nassar, A. A. Ali and A. S. Amin, A Facile Pechini Sol-Gel Synthesis of TiO2/Zn2TiO2/ZnO/C Nanocomposite: An Efficient Catalyst for the Photocatalytic Degradation of Orange G Textile Dye, *RSC Adv.*, 2017, **7**(48), 30411–30421, DOI: 10.1039/c7ra04899h.

338 G. Luciani, C. Imparato and G. Vitiello, Photosensitive Hybrid Nanostructured Materials: The Big Challenges for Sunlight Capture, *Catalysts*, 2020, **10**(1), 103, DOI: 10.3390/catal10010103.

339 S. Sharma, N. Kumar, B. Mari, N. S. Chauhan, A. Mittal, S. Maken and K. Kumari, Solution Combustion Synthesized TiO2/Bi2O3/CuO Nano-Composites and Their Photocatalytic Activity Using Visible LEDs Assisted Photoreactor, *Inorg. Chem. Commun.*, 2021, **125**, 108418, DOI: 10.1016/j.inoche.2020.108418.

340 Z. Lv, Q. Zhong and M. Ou, Utilizing Peroxide as Precursor for the Synthesis of CeO 2 /ZnO Composite Oxide with Enhanced Photocatalytic Activity, *Appl. Surf. Sci.*, 2016, **376**, 91–96, DOI: 10.1016/j.apsusc.2016.01.280.

341 M. R. D. Khaki and M. S. Shafeeyan, Sol–Gel Synthesized ZnO/Mn–TiO2 Core–Shell Nanocomposite and Its Elevated Activity for Methyl Orange Degradation, *J. Nanophotonics*, 2020, **14**(03), 036015, DOI: **10.1117/1.jnp.14.036015**.

342 M. Sangeeta, K. V. Karthik, R. Ravishankar, K. S. Anantharaju, H. Nagabhushana, K. Jeetendra, Y. S. Vidya and L. Renuka, Synthesis of ZnO, MgO and ZnO/MgO by Solution Combustion Method: Characterization and Photocatalytic Studies, in *Materials Today: Proceedings*, Elsevier Ltd, 2017, vol. 4, pp. 11791–11798. DOI: **10.1016/j.matpr.2017.09.096**.

343 R. Manimozhi, D. Ranjith Kumar and A. P. Gnana Prakash, Enhanced Solar Light Driven Photocatalytic Degradation of Organic Dye Using Solution Combustion Synthesized CeO_2-ZnO Nanocomposites, *J. Electron. Mater.*, 2018, **47**(11), 6716–6721, DOI: **10.1007/s11664-018-6649-z**.

344 S. A. Singh and G. Madras, Photocatalytic Degradation with Combustion Synthesized WO3 and WO3TiO2 Mixed Oxides under UV and Visible Light, *Sep. Purif. Technol.*, 2013, **105**, 79–89, DOI: **10.1016/j.seppur.2012.12.010**.

345 Z. H. Karahroudi, K. Hedayati and M. Goodarzi, Green Synthesis and Characterization of Hexaferrite Strontium-Perovskite Strontium Photocatalyst Nanocomposites, *Main Group Met. Chem.*, 2020, **43**(1), 26–42, DOI: **10.1515/mgmc-2020-0004**.

346 A. Sha, M. Chandrasekharan Meenu, P. Sasidharan Sumi, V. Chithrajakumary Bhagya, T. Revamma Sreelekshmy, B. Shibli and S. M. A, Tuning of Electron Transfer by Ni–P Decoration on CeO_2–TiO2 Heterojunction for Enhancement in Photocatalytic Hydrogen Generation, *Mater. Sci. Semicond. Process.*, 2020, **105**, 104742, DOI: **10.1016/j.mssp.2019.104742**.

347 X. Lu, X. Li, F. Chen, Z. Chen, J. Qian and Q. Zhang, Biotemplating Synthesis of N-Doped Two-Dimensional CeO_2–TiO2 Nanosheets with Enhanced Visible Light Photocatalytic Desulfurization Performance, *J. Alloys Compd.*, 2020, **815**, 152326, DOI: **10.1016/j.jallcom.2019.152326**.

348 M. H. Basha and N. O. Gopal, Solution Combustion Synthesis and Characterization of Phosphorus Doped TiO2–CeO_2 Nanocomposite for Photocatalytic Applications, *Mater. Sci. Eng., B*, 2018, **236–237**, 43–47, DOI: **10.1016/j.mseb.2018.12.001**.

349 T. C. Bhagya, A. Krishnan, S. Arunima Rajan, M. Ameen Sha, B. R. Sreelekshmy, P. Jineesh and S. M. A. Shibli, Exploration and Evaluation of Proton Source-Assisted Photocatalyst for Hydrogen Generation, *Photochem. Photobiol. Sci.*, 2019, **18**(7), 1716–1726, DOI: **10.1039/c9pp00119k**.

350 K. Das, D. Majhi, Y. P. Bhoi and B. G. Mishra, Combustion Synthesis, Characterization and Photocatalytic Application of CuS/Bi4Ti3O12 p-n Heterojunction Materials towards Efficient Degradation of 2-Methyl-4-Chlorophenoxyacetic Acid Herbicide under Visible Light, *Chem. Eng. J.*, 2019, **362**, 588–599, DOI: **10.1016/j.cej.2019.01.060**.

351 P. D. Bhange, D. S. Shinde, D. S. Bhange and G. S. Gokavi, Solution Combustion Synthesis of Heterostructure Bismuth Titanate Nanocomposites: Structural Phases and Its Correlation with Photocatalytic Activity, *Int. J. Hydrogen Energy*, 2018, **43**(2), 708–720, DOI: **10.1016/j.ijhydene.2017.10.150**.

352 J. P. Dhal, B. G. Mishra and G. Hota, Hydrothermal Synthesis and Enhanced Photocatalytic Activity of Ternary Fe2O3/ZnFe2O4/ZnO Nanocomposite through Cascade Electron Transfer, *RSC Adv.*, 2015, **5**(71), 58072–58083, DOI: **10.1039/c5ra05894e**.

353 Y. P. Bhoi, F. Fang, X. Zhou, Y. Li, X. Sun, J. Wang and W. Huang, Single Step Combustion Synthesis of Novel Fe2TiO5/α-Fe2O3/TiO2 Ternary Photocatalyst with Combined Double Type-II Cascade Charge Migration Processes and Efficient Photocatalytic Activity, *Appl. Surf. Sci.*, 2020, **525**, 146571, DOI: **10.1016/j.apsusc.2020.146571**.

354 W. Kang and A. Varma, Hydrogen Generation from Hydrous Hydrazine over Ni/CeO_2 Catalysts Prepared by Solution Combustion Synthesis, *Appl. Catal., B*, 2018, **220**, 409–416, DOI: **10.1016/j.apcatb.2017.08.053**.

355 M. Y. Nassar, I. S. Ahmed and I. Samir, A Novel Synthetic Route for Magnesium Aluminate (MgAl2O 4) Nanoparticles Using Sol-Gel Auto Combustion Method and Their Photocatalytic Properties, *Spectrochim. Acta, Part A*, 2014, **131**, 329–334, DOI: **10.1016/j.saa.2014.04.040**.

356 S. Indrawirawan, H. Sun, X. Duan and S. Wang, Low Temperature Combustion Synthesis of Nitrogen-Doped Graphene for Metal-Free Catalytic Oxidation, *J. Mater. Chem. A*, 2015, **3**(7), 3432–3440, DOI: **10.1039/c4ta05940a**.

357 W. Peng, S. Liu, H. Sun, Y. Yao, L. Zhi and S. Wang, Synthesis of Porous Reduced Graphene Oxide as Metal-Free Carbon for Adsorption and Catalytic Oxidation of Organics in Water, *J. Mater. Chem. A*, 2013, **1**(19), 5854–5859, DOI: **10.1039/c3ta10592j**.

358 Y. Yao, S. Miao, S. Liu, L. P. Ma, H. Sun and S. Wang, Synthesis, Characterization, and Adsorption Properties of Magnetic Fe 3O 4@graphene Nanocomposite, *Chem. Eng. J.*, 2012, **184**, 326–332, DOI: **10.1016/j.cej.2011.12.017**.

359 Z. Kalantari Bolaghi, S. M. Masoudpanah and M. Hasheminiasari, Photocatalytic Activity of ZnO/RGO Composite Synthesized by One-Pot Solution Combustion Method, *Mater. Res. Bull.*, 2019, **115**, 191–195, DOI: **10.1016/j.materresbull.2019.03.024**.

360 D. Zhang, Q. Ding, X. Pu, C. Su, X. Shao, G. Ding, Z. G. Zhang and Q. Fang, One-Step Combustion Synthesis of NiFe2O4-Reduced Graphene Oxide Hybrid Materials for Photodegradation of Methylene Blue, *Funct. Mater. Lett.*, 2014, **7**(1), 1350065, DOI: **10.1142/S1793604713500653**.

361 A. Sharma, A. Rani, A. Singh, O. P. Modi and G. K. Gupta, Synthesis of Alumina Powder by the Urea–Glycine–Nitrate Combustion Process: A Mixed Fuel Approach to Nanoscale

Metal Oxides, *Appl. Nanosci.*, 2014, **4**(3), 315–323, DOI: 10.1007/s13204-013-0199-8.

362 A. A. Voskanyan and K. Y. Chan, Solution Combustion Synthesis Using Furfuryl Alcohol as Fuel and a Combustible Solvent, *J. Exp. Nanosci.*, 2015, **10**(6), 466–475, DOI: 10.1080/17458080.2013.843028.

363 E. Novitskaya, J. P. Kelly, S. Bhaduri and O. A. Graeve, A Review of Solution Combustion Synthesis: An Analysis of Parameters Controlling Powder Characteristics, *Int. Mater. Rev.*, 2020, **66**(3), 188–214, DOI: 10.1080/09506608.2020.1765603.

364 T. Pine, X. Lu, D. R. Mumm, G. S. Samuelsen and J. Brouwer, Emission of Pollutants from Glycine-Nitrate Combustion Synthesis Processes, *J. Am. Ceram. Soc.*, 2007, **90**(12), 3735–3740, DOI: 10.1111/j.1551-2916.2007.01919.x.

365 E. J. Bosze, J. McKittrick and G. A. Hirata, Investigation of the Physical Properties of a Blue-Emitting Phosphor Produced Using a Rapid Exothermic Reaction, *Mater. Sci. Eng., B*, 2003, **97**(3), 265–274, DOI: 10.1016/S0921-5107(02)00598-6.

366 Z. Yue, W. Guo, J. Zhou, Z. Gui and L. Li, Synthesis of Nanocrystilline Ferrites by Sol-Gel Combustion Process: The Influence of PH Value of Solution, *J. Magn. Magn. Mater.*, 2004, **270**(1–2), 216–223, DOI: 10.1016/j.jmmm.2003.08.025.

367 L. C. Pathak, T. B. Singh, S. Das, A. K. Verma and P. Ramachandrarao, Effect of PH on the Combustion Synthesis of Nano-Crystalline Alumina Powder, *Mater. Lett.*, 2002, **57**(2), 380–385, DOI: 10.1016/S0167-577X(02)00796-6.

368 A. Mukasyan and P. Dinka, Novel Approaches to Solution-Combustion Synthesis of Nanomaterials, *Int. J. Self-Propag. High-Temp. Synth.*, 2007, **16**, 23–35.

369 H. H. Nersisyan, J. H. Lee, J. R. Ding, K. S. Kim, K. V. Manukyan and A. S. Mukasyan, Combustion Synthesis of Zero-, One-, Two- and Three-Dimensional Nanostructures: Current Trends and Future Perspectives, *Prog. Energy Combust. Sci.*, 2017, 79–118, DOI: 10.1016/j.pecs.2017.07.002.

370 R. Ghose, H. T. Hwang and A. Varma, Oxidative Coupling of Methane Using Catalysts Synthesized by Solution Combustion Method, *Appl. Catal., A*, 2013, **452**, 147–154, DOI: 10.1016/j.apcata.2012.11.029.

371 A. Naveenkumar, P. Kuruva, C. Shivakumara and C. Srilakshmi, Mixture of Fuels Approach for the Synthesis of SrFeO3-δ Nanocatalyst and Its Impact on the Catalytic Reduction of Nitrobenzene, *Inorg. Chem.*, 2014, **53**(22), 12178–12185, DOI: 10.1021/ic502121k.

372 R. Ianoş, R. Istratie, C. Pəcurariu and R. Lazəu, Solution Combustion Synthesis of Strontium Aluminate, SrAl2O4, Powders: Single-Fuel versus Fuel-Mixture Approach, *Phys. Chem. Chem. Phys.*, 2015, **18**(2), 1150–1157, DOI: 10.1039/c5cp06240c.

373 M. Mapa and C. S. Gopinath, Combustion Synthesis of Triangular and Multifunctional ZnO 1-XNx (x = 0.15) Materials, *Chem. Mater.*, 2009, **21**(2), 351–359, DOI: 10.1021/cm803048h.

374 M. Ahmad, Z. Hong, E. Ahmed, N. R. Khalid, A. Elhissi and W. Ahmad, Effect of Fuel to Oxidant Molar Ratio on the Photocatalytic Activity of ZnO Nanopowders, *Ceram. Int.*, 2013, **39**(3), 3007–3015, DOI: 10.1016/j.ceramint.2012.09.079.

375 H. Vahdat Vasei, S. M. Masoudpanah and M. Habibollahzadeh, Different Morphologies of ZnO via Solution Combustion Synthesis: The Role of Fuel, *Mater. Res. Bull.*, 2020, **125**, 110784, DOI: 10.1016/j.materresbull.2020.110784.

376 D. N. V. V. Konda Lutukurthi, S. Dutta and D. K. Behara, Effect of Ignition Temperature and Fuel Amount on Photocatalytic Activity of Solution Combustion Synthesized ZnO, *Ceram. Int.*, 2020, **46**(14), 22419–22428, DOI: 10.1016/J.CERAMINT.2020.05.324.

377 M. Minakshi, D. R. G. Mitchell, C. Baur, J. Chable, A. J. Barlow, M. Fichtner, A. Banerjee, S. Chakraborty and R. Ahuja, Phase Evolution in Calcium Molybdate Nanoparticles as a Function of Synthesis Temperature and Its Electrochemical Effect on Energy Storage, *Nanoscale Adv.*, 2019, **1**(2), 565–580, DOI: 10.1039/c8na00156a.

378 J. L. Hernández-Pinero, M. Terrón-Rebolledo, R. Foroughbakhch, S. Moreno-Limón, M. F. Melendrez, F. Solís-Pomar and E. Pérez-Tijerina, Effect of Heating Rate and Plant Species on the Size and Uniformity of Silver Nanoparticles Synthesized Using Aromatic Plant Extracts, *Appl. Nanosci.*, 2016, **6**(8), 1183–1190, DOI: 10.1007/s13204-016-0532-0.

379 H. Vahdat Vasei, S. M. Masoudpanah and V. Kamrani Pouya, Photocatalytic Activity of Solution Combustion Synthesized ZnO Powders by Using a Mixture of DTAB and Citric Acid Fuels, *J. Phys. Chem. Solids*, 2021, **151**, 109895, DOI: 10.1016/j.jpcs.2020.109895.

380 H. K. Timmaji, W. Chanmanee, N. R. De Tacconi and K. Rajeshwar, Solution Combustion Synthesis of BiVO4 Nanoparticles: Effect of Combustion Precursors on the Photocatalytic Activity, *J. Adv. Oxid. Technol.*, 2011, **14**(1), 93–105, DOI: 10.1515/jaots-2011-0112.

381 G. P. Nagabhushana, D. Samrat and G. T. Chandrappa, α-MoO3 Nanoparticles: Solution Combustion Synthesis, Photocatalytic and Electrochemical Properties, *RSC Adv.*, 2014, **4**(100), 56784–56790, DOI: 10.1039/c4ra05135a.